Magnetic field effects on the local tunneling conductivity of $La_{0.75}Ca_{0.25}MnO_3$/MgO thin films

Dissertation
zur Erlangung des Doktorgrades
der Mathematisch-Naturwissenschaftlichen Fakultäten
der Georg-August-Universität zu Göttingen

vorgelegt von

Sigrun Antje Köster

aus

Braunschweig

Göttingen 2007

D7

Referent:	Prof. Dr. Konrad Samwer
Korreferent:	PD Dr. Christian Jooß
Tag der Disputation:	10. Oktober 2007

Abstract

Manganites are known for their exceptional properties, such as the metal-insulator transition (MIT) and the colossal magnetoresistance (CMR) effect. These materials show a very rich phase diagram in which the properties of the different phases do not only depend on the doping and temperature but also on electric and magnetic fields. Manganites are interesting candidates for studying the physics of correlated electrons and are also possible candidates for technological applications. It is known that a strong interplay between lattice, charge, spin and orbital degrees of freedom plays a very important role, which has been described in different theoretical models. Until now the basic mechanisms responsible for the special electronic and magnetic properties and the CMR effect are far from being understood completely. Hence more experimental work is crucial for understanding manganites.

Scanning tunneling microscopy (STM) and spectroscopy (STS) are very local and surface sensitive techniques for probing the topography and the local electronic properties. They were used in this work to examine manganites with a metallic and ferromagnetic low temperature ground state. Overall strain-free thin films of $La_{3/4}Ca_{1/4}MnO_3$ were deposited on MgO(100) substrates and showed different microscopic growth modes and crystal symmetries depending on the deposition parameters. The films were examined by STM/STS with respect to their temperature behavior and especially their behavior in external magnetic fields in the vicinity of the MIT. Furthermore, the films were compared with respect to their growth modes.

The experiments reveal that the local tunneling conductivity changes continuously with temperature and magnetic field. The tunneling conductivity also varies locally, but neither distinct phases nor a domain-like growth of some regions with a magnetic field were found. This is inconsistent with the most popular theory of a percolation scenario. In a nutshell, a percolation of insulating and metallic phases does not seem to be a necessary prerequisite for the CMR effect.

Zusammenfassung

Die Manganate sind für ihre besonderen Eigenschaften, wie den Metal-Isolator Übergang (MIT) und den kolossalem Magnetowiderstandseffekt (CMR), bekannt. Diese Materialien zeigen ein sehr reichhaltiges Phasendiagramm, wobei die Eigenschaften der verschiedenen Phasen nicht nur von der Dotierung und der Temperatur abhängig sind, sondern auch von elektrischen und magnetischen Feldern. Die Manganate sind interessante Kandidaten für das Studium der Physik korrelierter Elektronen als auch für eventuelle technische Anwendungen. Es ist bereits bekannt, dass die Wechselwirkung der verschiedenen Freiheitsgrade (Gitter, Ladung, Spin und Orbital) eine sehr wichtige Rolle spielen. Dies wird in verschiedenen theoretischen Modellen beschrieben. Dennoch sind die Mechanismen, die für die elektronischen und magnetischen Eigenschaften verantwortlich sind noch lange nicht vollständig verstanden. Weitere experimentelle Untersuchungen sind daher unentbehrlich für das Verständnis der Manganate.

Rastertunnelmikroskopie (STM) und -spektroskopie (STS) sind sehr lokale und oberflächensensitive Verfahren, um die Topografie und die lokalen elektronischen Eigenschaften einer Probe zu erfassen. In dieser Arbeit wurden Manganate mit einem metallischen und ferromagnetischen Grundzustand bei tiefen Temperaturen untersucht. Spannungsfreie dünne $La_{3/4}Ca_{1/4}MnO_3$-Filme wurden auf MgO(100) Substraten deponiert und zeigten je nach Herstellungsparametern unterschiedliche Wachstumsmoden und Kristallsymmetrien. Die Proben wurde mittels STM und STS in Abhängigkeit der Temperatur und insbesondere von äußeren magnetischen Feldern im Bereich des MIT untersucht und bezüglich ihrer Wachstumsmoden miteinander verglichen.

Die Experimente zeigen, dass sich die lokale Tunnelleitfähigkeit kontinuierlich mit der Temperatur und dem Magnetfeld ändert. Die Tunnelleitfähigkeit variiert auch lokal, allerdings sind keine einzelnen klar unterscheidbaren Phasen zu sehen und es ist kein Domänenwachstum von einzelnen Bereichen in Abhängigkeit vom Magnetfeld zu beobachten. Dies entspricht nicht der verbreiteten Theorie eines Perkolationsübergangs. Kurz gesagt, scheint also ein Perkolationsübergang mit einer isolierender und metallischer Phase nicht notwendigerweise der Ursprung des CMR zu sein.

Contents

Glossary

Abbreviations

3D Three dimensional (grain-like) growth.

ac Alternating current.

ACEC Acetylacetonate, negatively charged, used a ligand for metal-chelate complex compounds.

ADC Analog digital converter.

AF Antiferromagnetic phase.

AFM Atomic force microscope.

AMR Anisotropic magneto resistance.

CMR Colossal magneto resistance.

CO Charge ordered phase.

DAC Digital analog converter.

dc Direct current.

DE Double exchange.

DMFA Dimethylformamide.

DMFT Dynamical mean field theory.

DOS Density of States.

ED Electron diffraction.

FFT Fast Fourier Transform.

FM Ferromagnetic phase.

FT Fourier Transform.

FWHM Full width of half maximum.

GMR Giant magneto resistance.

HOPG Highly oriented pyrolytic graphite.

HRTEM High resolution transmission electron microscopy.

I Insulating phase.

IDL Interactive data language, Research Systems, Inc.

IVC Current voltage converter.

LCMO $La_{0.75}Ca_{0.25}MnO_3$ (results and discussion); $La_xCa_{1-x}MnO_3$ (in general terms).

LDOS Local Density of States.

LL Layer-by-layer growth.

LL-O Layer-by-layer growth with an A-site ordering.

M Metallic phase.

M^{n+} Metal ion as chemical symbol with charge n+.

MAD Metal organic aerosol deposition.

MFM Magnetic force microscope.

MIT Metal insulator transition.

MOCVD Metal organic chemical vapor deposition.

NV Needle valve.

OVC Outer vacuum shell (Omicron cryostat).

PM Paramagnetic phase.

PPMS Physical Property Measurement System, Quantum Design, here used for resistance measurements.

rf Radio frequency.

rms Root mean square.

RT Room temperature (300K).

SAXS Small angle X-ray scattering.

SE Superexchange.

SFM Scanning force microscope.

SPM Scanning probe microscope.

SQUID Superconducting Quantum Interference Device, in this work a SQUID-magnetometer from Quantum Design was used for magnetization measurements.

STM Scanning tunneling microscope.

STS Scanning tunneling spectroscopy.

TEM Transmission electron microscopy.

TMR Tunnel magneto resistance.

TSP Titanium sublimation pump.

UHV Ultra high vacuum.

VIC Voltage current converter.

VTI Variable temperature insert.

WAXS Wide angle X-ray scattering.

XRD X-ray diffraction.

XRR X-ray reflectometry.

Symbols

a, b Lattice parameters (unit cell or pseudo cubic cell), in general to describe the in-plane parameters.

A Amplitude, parameter in exponential decay.

c Lattice parameter (unit cell or pseudo-cubic cell), in general to describe out-of-plane parameter.

C_{fg} Convolution between functions f and g.

C Correlation function, capacitance (experimental part), sometimes a constant.

$C(r)$ Radial correlation function.

d_{hkl} Spacing of lattice planes corresponding to the Miller indices hkl.

d Film thickness.

e Electron charge.

E Energy, generally as fixed value.

E_F Fermi energy.

$\mathbf{F}^{\pm}$ Operator for Fourier Transform $(+)$ and its inverse $(-)$.

f, g Functions.

$f^*(x)$ Complex conjugate of f.

$\hat{f}$	Fourier transform of f.
F	Force.
$f(\epsilon)$	Fermi-Dirac distribution.
hkl	Miller indices.
I_0	Current (predetermined).
I	Current/Tunneling current.
j, l	Indices (integers) for discrete FT.
$\vec{k}_{i/r}$	Incident (i) and reflected (r) wave vectors for X-ray geometry.
L	Self inductance.
m	(Electron) Mass, interference maxima.
m_i	Number of interference maximum (integer).
$M_{\mu\nu}$	Matrix elements, connecting the states within the tunneling equation.
m_0	Electron mass.
n	Refractive index.
N_A	Avogadro number ($6.02217 \cdot 10^{23}$).
N_e	Electron density.
N	Integer number.
$\vec{q}$	Scattering vector of X-rays.
r_e	Classical electron radius.
$r_{1/2}$	Radii for distance of sample contacts.
r	Radius (used in correlation functions).
r_l	Correlation length (here: exponential decay length of radial correlation).
$\vec{r}$	Spacial position vector.
t	Time.
T	Temperature.
U, V	Voltage.
u	Variable, like x.
x, y	Coordinates (in plane).
z	Coordinate (perpendicular to plane), height.
Z	Transfer function.

Greek Symbols

β	Imaginary part of refractive index, describing absorption.
χ	Error.
δ	Real part of refractive index, describing dispersion.
ϵ	Energy, in general as variable.
κ	Exponential decaying constant for wavefunctions in classically forbidden region.
λ	Wavelength of X-rays (for CuK_α=1.54184·10^{-8} cm).
μ, ν	Indices, corresponding to the energy states of the different electrodes in a tunneling junction.
μ	Attenuation coefficient.
Φ	Magnetic flux.
Φ_{ext}	Magnetic flux from an external source.
Φ_0	Flux quantum.
$\Phi_{\mu,\nu}; \Phi_{s,t}$	Work functions for tunneling electrodes (tip,sample).
$\Psi_{\mu,\nu}$	Wave functions for tunneling electrodes.
ρ	Mass density, resistivity.
$\rho(\epsilon)$	Density of states as function of energy.
σ	Roughness (rms), tunneling conductivity dI/dU.
σ_p	Peak (mean) conductivity of histograms from tunneling conductivities.
Θ	Angle of incidence (with respect to the surface) for XRD.
Θ_t	Angle of total reflection for XRR.

1. Introduction

In solid state physics as well as in industrial technology the dimensions of the research on structure, electronics and magnetism get smaller and smaller and the word "nano" has become a representative classifying these fields. The so-called magneto resistance (MR) effects belong into this regime, since they deal about magnetism on the nanometer scale and are involved in devices utilized in nanotechnology. The MR effect appears as changes in the resistivity ρ of a sample induced by an applied magnetic field H. These effects can be very large and underly very different mechanisms, not all of them being finally understood. In manganites the MR effect is caused by an interplay of microscopic interactions, and take effect on the properties on a nanometer scale, therefore the topic of this work can be included in the widespread areas of nano-scale magnetism and nano-scale electronic features.

Manganites are manganese oxide compounds mixed with rear earth and/or transition metal elements like $La_{0.75}Ca_{0.25}MnO_3$. They show peculiar magnetic and electronic properties. Since the discovery of the colossal magneto resistance (CMR) effect in manganites [7], they can be regarded as materials of widespread interest in solid state physics and materials sciences. The manganites belong to the correlated electron systems, which are interesting for basic research with respect to the understanding of the specific microscopic interactions and are still far away from being understood. In correlated electron systems the individual charge carriers are not independent from each other, like it is the case in a simple metal as copper with a nearly free electron gas, but their behavior is coupled. This is due to the fact that correlated electron materials consist of d- or f–electron systems, which have quite localized orbitals. Therefore the Coulomb repulsion becomes very important and the behavior of one electron depends on all the others.

A basic model describing correlated electron systems is the Hubbard model [4], but the real cases are usually much more complex. An intricate system of lattice, charge, orbital and spin degrees of freedom makes the manganites to fascinating candidates in the context of electronic transport and magnetism in correlated electron materials. Complex phase diagrams with regions of very different properties, that is insulating, metallic, ferromagnetic, antiferromagnetic or charge and orbital ordered phases can be observed.

Ferromagnetic manganites show a metal to insulator transition together with a ferromagnetic to paramagnetic transition, for which the transition temperatures can be tuned by the composition. The largest values for the CMR effect are observed in the temperature region of these transitions, which are coupled to each other. The driving mechanism of this metal-insulator transition has not been fully understood

and remarkably the CMR effect becomes larger for those compounds showing higher residual resistivities.

It is known already that the charge transport is somehow coupled to the magnetic properties via the superexchange and double exchange mechanisms, which evoke either an antiferromagnetic or ferromagnetic coupling of the core spins of the manganese atoms via the oxygen atoms in between. A movement of the charge carrier is then dependent on the orientations of the spins or more precisely local moments. This can explain the reduction of the resistivity within magnetic fields, but taking only these exchange mechanisms into account proves to be insufficient. Charge and lattice effects, as Jahn-Teller distortions or polarons, play a crucial role. Additionally, for the CMR effect a phase separation scenario is discussed. The competition of a ferromagnetic metallic and an antiferromagnetic insulating phase has been proposed and partially observed in some experiments. It is still under debate if phase separation and percolation is essential for the occurrence of the CMR effect.

Manganites exist as single crystals, polycrystalline bulk samples or as thin films on very different oxidic substrates. Of course the real intrinsic properties can only be observed for single crystalline samples or unstrained thin films, in contrast to extrinsic effects, which are observed for polycrystalline samples due to the grain sizes and interface effects [9]. Since the production of single crystals is not straightforward, very often thin films are used for the experiments. In addition, they are also more useful candidates for various applications. The properties of thin films cannot only be varied by their composition, but also by the substrate on which they are deposited.

A lot of models for the metal-insulator transition in manganites exist, but they are in general too simple to explain the entire system. Therefore it is still necessary to perform experimental research on this system. The bulk properties have already been widely examined, however for the origin of these properties microscopic techniques are of relevance. Such a technique is the scanning tunneling microscopy (STM) together with scanning tunneling spectroscopy (STS). With STM the surface of the sample can be examined on a nanometer scale and STS yields information about the local electronic properties of the sample. If these observations are done together with the application of magnetic fields, which is a quite challenging task, it is possible to investigate directly the field induced changes of the local properties.

To shed somewhat more light onto this issue was the task of this thesis. The local electronic properties of thin ferromagnetic manganite films were examined. This was done with respect to the occurrence of a phase separation and concerning the behavior within applied magnetic fields.

Due to their peculiar properties manganite thin films are interesting for technological applications, since they show a variety of magnetoresistance effects and possess a large spin-polarization. The latter is important for magnetic layer systems. The magneto resistance effects in materials can be used for magnetic field sensors, magnetic memories, switches or other devices. For example the giant magneto resistance effect (GMR) found in specific layer systems [3], is used in read

heads of hard disks [1]. In manganite thin film structures an anisotropic magneto resistance effect (AMR) was found, that is the resistivity of the film depends on the direction of the magnetic field with respect to the crystallographic orientations. Since the spin-polarization is very high in manganites, they might be utilized in tunneling magneto resistive (TMR) systems [5, 6] as well. For example the TMR effect is used in magnetic random access memory devices (MRAM). A very new field is the current induced switching in magnetic spin valve systems. One of the magnetic layers is switched by a current, which is applied perpendicular to the plane. Some groups work on manganite based field-effect transistors [8] and additionally the ferroelectric properties are in the focus of technological research. A summary of some of the important new materials useful for technological applications is given in [2].

In this work STM and STS measurements were performed mainly in the vicinity of the metal-insulator transition on $La_{0.75}Ca_{0.25}MnO_3$ thin films, which were deposited on MgO substrates by the metal organic aerosol deposition (MAD) technique. To achieve some STS data with a magnetic field applied, a microscope situated in a cryostat under ultra high vacuum conditions was used. The thesis is structured as in the following:

The fundamental properties and theories for the basic understanding of manganites are introduced in **Chapter 2** together with a review of the most important literature. It is followed by a brief summary of the theoretical fundamentals about the STM and STS techniques in **Chapter 3**. The standard experimental techniques used for the thin film deposition and characterization are reviewed in short in **Chapter 4**. Then a detailed presentation of the microscope used for this work and its environment is given in **Chapter 5**. The experimental results are split into two parts: Whereas **Chapter 6** deals with the basic sample characteristics, **Chapter 7** presents the STM and STS results. In **Chapter 8** the results are discussed and the work is finished by a summary and outlook in **Chapter 9**. The references appear in alphabetical order for each chapter.

Bibliography

[1] Recording heads/head materials. http://www.hitachigst.com/hdd/research/recording_head/headmaterials/index.html, 2007. Hitachi Global Storage Technologies, San Jose, California, USA.

[2] Forschungszentrum Jülich GmbH, Institut für Festkörperforschung. *Neue Materialien für die Informationstechnik*, volume 32 of *IFF-Ferienkurs*. Forschungszentrum Jülich GmbH, 2001.

[3] B. Heinrich and J. A. C. Bland, editors. *Ultrathin Magnetic structures II*, volume 2. Spinger Verlag (Berlin, Heidelberg), 1994.

[4] J. Hubbard. Electron correlations in narrow energy bands. *Proc. Roy. Soc. A*, 276:238, 1963.

[5] J. S. Moodera, L. R. Kinder, T. M. Wong, and T. Meservey. *Phys. Rev. Lett.*, 74:7, 1995.

[6] J. S. Moodera and G. Mathon. *J. Magn. Magn. Mat.*, 200:248, 1999.

[7] R. von Helmolt, J. Wecker, B. Holzapfel, L. Schultz, and K. Samwer. *Phys. Rev. Lett.*, 71:2331, 1993.

[8] T. Zhao, S. B. Ogale, S. R. Shinde, R. Ramesh, R. Droopad, J. Yu, K. Eisenbeiser, and J. Misewich. *Appl. Phys. Lett.*, 84:750, 2004.

[9] M. Ziese. *Rep. Prog. Phys.*, 56:143, 2002.

2. Manganites

The so called manganites are manganese oxide compounds mixed with rare earth and alkaline earth elements. They show a large variety of structural, resistive and magnetic properties. These can be attributed to complicated interactions of charge, orbital and spin degrees of freedom. Like some other correlated oxides (e.g. the group of vanadium oxides) they show a metal-insulator transition, which can reach room temperature or even higher temperatures depending of the particular composition. Additionally large magneto-resistive effects can be observed coupled to the magnetic transitions, which made the manganites very popular in solid state research. The manganites show in general a rich phase diagram, which gives the possibility to learn a lot about these transitions and their coupled electronic and magnetic properties. Besides a technical usage of these compounds, their study provides a widespread possibility to gain more insight in correlated electron systems.

The first interest in manganese oxide compounds came up in 1950, when van Santen and Jonker reported about an "anomaly" in the resistive behavior of manganites [67], the *metal-insulator transition* (MIT). They also firstly studied the crystallographic and magnetic properties of these compounds. Some more studies followed [31, 70] including theoretical work by Zener [74], Hasegawa et al. [5] and de Gennes [19]. But the large interest in manganites arose much later, when – due to higher quality samples – the so called *colossal magneto-resistance effect* (CMR) with changes in the resistance of up to 100.000% was discovered [69, 8, 46, 60, 41, 9] in thin films and in bulk materials.

In the following the physics of manganites will be briefly reviewed, including the main properties, the most important structures and the basic exchange mechanisms, which are important to understand the complexity evolving in the phase diagrams. One section is addressed to the phase separation, which is very important for the present discussions regarding the phase transition. The chapter is oriented at the ferromagnetic compounds and at the end the features of $La_{1-x}Ca_xMnO_3$ will be summarized. In conjunction with the results obtained in this work a detailed discussion of particular models and a comparison with other results in the literature is following in the discussion, Chap. 8.

2.1. Fundamental properties

Talking about the manganites the following group of compounds is meant: The parent compound is the perovskite ABO_3 with Mn on the B-site, for instance $LaMnO_3$ or $CaMnO_3$. The A-site can be split into two groups of elements, for the doping of the respective parent compound. The resulting compound is $RE_{1-x}AE_xMnO_3$ with

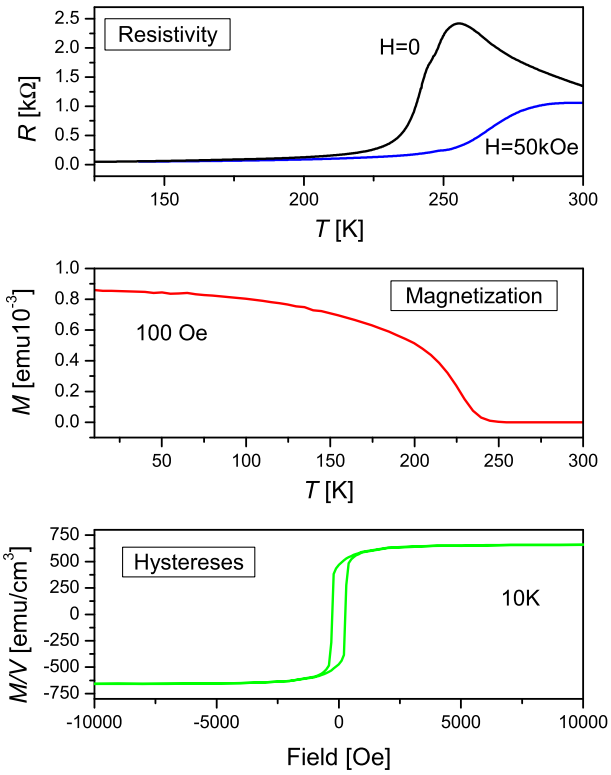

Figure 2.1.: The main features of ferromagnetic manganites. Top: Resistance R versus temperature T for a zero and non-zero field ($H = 50\,\mathrm{kOe}$) measurement. Middle: Magnetization M versus temperature. Bottom: Hysteresis loop $M(H)$ at $T = 10\,\mathrm{K}$. The measurements stem from a $La_{1-x}Ca_xMnO_3$ thin film for $x = 0.3$ on a MgO substrate.

RE as the trivalent rare earth elements (La, Pr, Nd, Sm, etc.) and AE as divalent alkaline earth ions (Sr, Ca, Ba). In a ionic model it would be $RE^{3+}_{1-x}AE^{2+}_x(Mn^{3+}_{1-x}Mn^{4+}_x)O_3$, underlining already the important role of the mixed valence on the manganite site, which is – to a large extent – responsible for the widespread properties found. The latter will be reviewed in course of the detailed structural and electronic properties.

The properties observed within the manganite family vary from antiferromagnetic insulators ($LaMnO_3$, $CaMnO_3$), over insulating ferromagnets ($Pr_{0.8}Ca_{0.2}MnO_3$) to ferromagnetic metals ($La_{0.75}Sr_{0.25}MnO_3$, $La_{0.75}Ca_{0.25}MnO_3$) and charge ordering ($La_{7/8}Ca_{1/8}MnO_3$) in their low temperature phase. Most of them undergo a phase transition at a certain temperature with respect to their electronic and magnetic behavior, which are strongly coupled to each other. Also structural transitions are observed supplementary. About the basic properties of the different compounds a lot of review articles can be found, for instance in Refs. [64, 12, 58, 22, 65]. Commonly the CMR effect is introduced together with the MIT from a ferromagnetic metal to a paramagnetic insulator, like in the case of $La_{0.75}Ca_{0.25}MnO_3$.

The MIT in the manganites can be described as a transition between a metallic

transport characteristic with a positive slope $d\rho/dT \geq 0$ of the resistivity ρ as a function of temperature T. Above the *metal-insulator transition temperature* (T_{MI}) this behavior is reversed and an insulating behavior with $d\rho/dT \leq 0$, that is an activated transport, is observed. This is a typical behavior which can be observed also in some other materials (e.g. NiS, FeSi) and various oxides [28]. In the transition region the resistivity ρ becomes maximal, shown in the upper panel of Fig. 2.1 in the resistance curve $R(T)$ at zero field. Compared to normal metals (Cu: $\rho \approx 1.7\,\mu\Omega$cm) in manganites the residual resistivities at $T \sim 4.2\,$K are with $\rho \approx 100\,\mu\Omega$cm still much larger.

In the manganites the metal-insulator transition is coupled to a magnetic transition from a ferromagnetic state into a paramagnetic state above the critical temperature T_C, which is normally not far apart from the T_{MI} . A magnetization curve $M(T)$ is shown in the middle panel of Fig. 2.1. At low temperatures a large magnetization M can be observed, which is vanishing at the transition into the paramagnetic phase above T_C. An example for a hysteresis loop $M(H)$ with the external magnetic field H is shown in the lower panel in the figure and indicates a ferromagnetic behavior with a remanent magnetization and the coercive field below T_C.

The huge CMR effect is manifested in the lowering of the resistivity in large magnetic fields. Additionally to the typical resistivity curve in Fig. 2.1 a resistivity curve taken within a magnetic field of 50 kOe is plotted. Here it can be seen, that the resistance is lowered in general in the presence of a magnetic field, but the effect is largest in the vicinity of the MIT. Another detail is the shifting of the temperature of the resistivity maximum due to the magnetic field. The MIT is displaced to larger temperatures.

Consequently, for a constant temperature the CMR is defined as the resistance ratio [1]

$$MR = \frac{R(H) - R(0)}{R(0)}. \qquad (2.1)$$

This effect becomes large for several Tesla and close to the metal-insulator transition region already small fields cause a reasonable change in the resistivity. An example is given in Fig. 2.2, with MR curves for different temperatures. The last curve for 270 K lies above T_{MI} in the paramagnetic region and has a somewhat different shape at small fields, that is, the curvature is different.

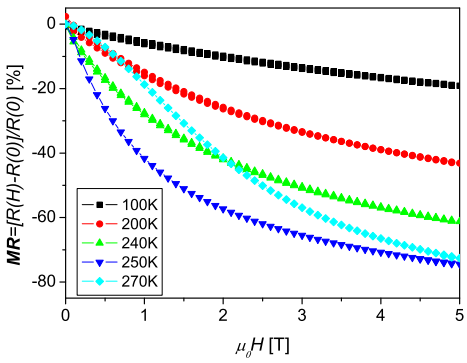

Figure 2.2.: Magnetoresistance MR versus magnetic field for different temperatures (thin film $La_{1-x}Ca_xMnO_3$, $x = 0.3$ on MgO). The last curve was taken at 270 K $> T_{MI}$.

[1] Here the definition is used, in which the MR cannot exceed 100%.

2.1.1. Crystal structure

The basic perovskite structure[2] is shown in Fig. 2.3 in the pseudo-cubic representation for $LaMnO_3$. The A-site (La) atoms are situated in the center of the cube, while the B-site (Mn) occupies the corners of the cube. The oxygen atoms are found on the center of the edges and form an octahedron surrounding the B-site atoms, as marked by the dotted line. The lattice parameter a_p for the pseudo-cubic representation is the length of the edge of the cube.

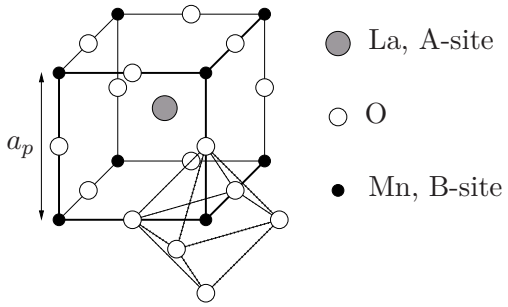

Figure 2.3.: Pseudocubic perovskite structure (this is not the primitive cell of the perovskite). The oxygen octahedron is marked by the dotted lines.

The oxygen octahedrons are crucial to consider within this structure for various reasons: Depending on the different chemical compositions they might be tilted or distorted. Additionally the transport properties rely on the manganese-oxygen bonds, described later. In an ideal cubic perovskite the ratio of the bond lengths (of the oxygen and the A-site atom, d_{A-O}, and the oxygen and the B-site atom, d_{B-O}) is equal to $\sqrt{2}$. To distinguish different chemical compositions, with atoms of different size and different doping levels, and to account for their effects on the structure the tolerance factor

$$f = \frac{1}{\sqrt{2}} \frac{d_{A-O}}{d_{B-O}} \approx \frac{1}{\sqrt{2}} \frac{(< r_A > + r_O)}{(< r_B > + r_O)} \tag{2.2}$$

was introduced [12]. Since the bond lengths are generally not known, the mean ionic radii ($< r_A >, < r_B >$) of the A- and B- sites are used for a prediction of the structure. For an ideal perovskite structure $f \equiv 1$, small deviations from this value lead to considerable stress. To compensate for the latter, the octahedrons become tilted. In the next chapter also a distortion of the octahedrons and its electronic origin will be described in more detail. These facts lead to different structures for the manganites. Two of the most frequent ones are the orthorhombic and rhombohedral structures; they are shown with respect to the cubic cell in Fig. 2.4. In comparison to the *cubic* structure the *tetragonal* shows $a = b \neq c$, which is a special case of the *orthorhombic* structure $a \neq b \neq c$ with $a \neq b \approx \sqrt{2}, c = 2a_p$. The *rhombohedral* structure can always be represented as a pseudo-cubic structure with $a = b = c$. The single octahedrons are not shown here for simplicity, the structures can be found in the literature, e.g. [48].

In the *rhombohedral* (space group $R\bar{3}c$) structure with $0.96 < f < 1$ (Fig. 2.4, left) all Mn-O bond lengths are equal, but the oxygen octahedrons are all tilted slightly in the same direction, which leads to the diagonal distortion compared to the cubic structure. The *orthorhombic* (space group P_{nma}) structure with $f < 0.96$ [24] (Fig. 2.4, right) consists of octahedrons, which are each tilted in opposite directions, also called alternating buckling. Additionally they are distorted and have different Mn-O bond lengths.

[2] The Name *Perovskite* originates from the trivial name of the mineral $CaTiO_3$.

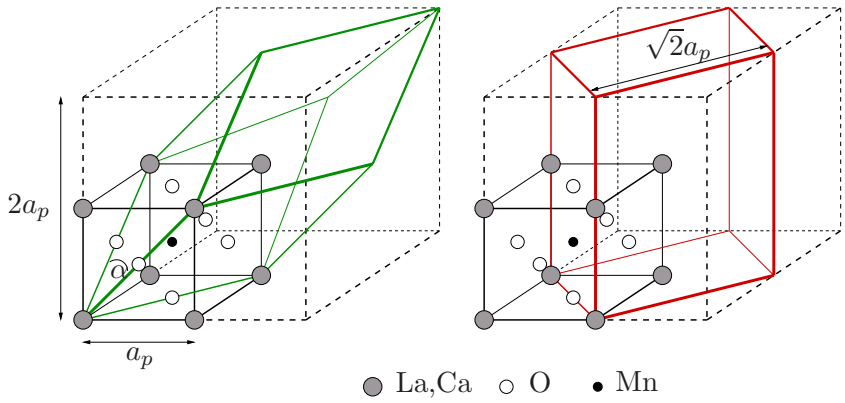

Figure 2.4.: Pseudocubic perovskite structure with lattice constant a_p and the related rhombohedral (green) and tetragonal (red) structure, which is as a special case of the orthorhombic structure very similar to it.

2.1.2. Basic electronic properties

The presentation of the properties of the manganites is quite complex and simplifications have to be made to gain insight into their properties. First of all, the considerations follow those for magnetic oxides (mainly transition metal oxides) [35]. In the latter, typically, the electrons responsible for the electronic behavior also account for their magnetic nature. Hence these materials can be characterized by a close connection between transport and magnetism. In the following the basic principles, which are important for the understanding of the transport and magnetic properties, will be presented split into two parts.

There are two models to be considered, the ionic description and the band model. Although due to the orbital overlap the band model would be physically more appropriate, a lot of characteristics can be already explained sufficiently well within a ionic-like picture. In the manganese atoms the highest occupied levels are the 3d levels with a configuration of $[Ar]3d^5 4s^2$ (and correspondingly the Mn^{3+}, Mn^{4+}-ions $[Ar]3d^4$ and $[Ar]3d^3$). Since the Fermi level is lying in the very narrow d-band a ionic-like approach is justifiable. The five d-orbitals have different geometries, the group of the t_{2g} orbitals called xy, yz, zx have each their "barbell" pointing in between the axis and the two $d_{x^2-y^2}, d_{3z^2-r^2}$ orbitals belonging to the e_g-orbitals are pointing towards the axis. Examples for the orbitals are shown in Fig. 2.5 (a). Since the Mn-ions are surrounded by O-ions, the figure shows how the orbitals of the oxygen and manganese are situated with respect to each other. It can be seen that an overlap of the d_{e_g}-orbitals with the p-orbitals of the oxygen is possible, while the others point into different directions and the overlap can only be very small.

The transport takes place between the manganese ions via the oxygen ions, depending on the overlap of the orbitals (the possible mechanisms are explained below). Since there is not always a perfect pseudo-cubic structure with $f = 1$, the overlap depends on the distance of the ions and the bond angle. The d-orbitals are not five-fold degenerate, like in a separated ion, but due to the *crystal field*, for

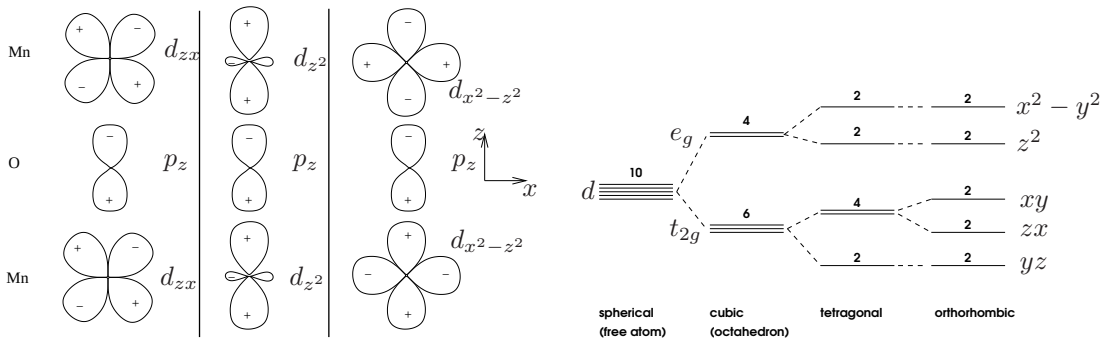

(a) Geometry of 3d-orbitals **(b)** Energy of 3d-orbitals

Figure 2.5.: Geometry of the 3d-orbitals and their orientation with respect to the oxygen p-orbitals (a). Energy level diagram and degeneracy (given in numbers including the spin) of the 3d-orbitals for different crystal fields[a] (b), adapted from [28]. (Drawn levels are no true to scale.)

[a] The Jahn-Teller splitting is not included here.

instance, of the octahedral oxygen coordination, the orbitals are energetically split (see Fig. 2.5 (b)), originating in the different geometries mentioned before and the *Coulomb repulsion* between the electrons. In Fig. 2.5 (b) these energy splittings are shown for different crystal fields in different crystal structures. The other cations have closed shells (La^{3+} with [Xe] and Ca^{2+} with [Ar]) and do only play a minor role in transport and magnetism. They can be neglected concerning the basic mechanisms.

It has already been pointed out, that the symmetry of the orbitals within the crystal has an important influence onto the resulting energy splitting. Here another mechanism, the *Jahn-Teller-distortion* [29] driven by symmetry will be introduced. In Fig. 2.5 (b) the energy splitting of the e_g and t_{2g} orbitals has been shown. According to Hund's rule the electrons are filled such that a high spin state is achieved, since the Hund's coupling is quite large in manganites. This means, that for a Mn^{3+}-ion the t_{2g} orbitals are all filled with one electron and in the doubly degenerate e_g orbitals one electron has to be placed. This is demonstrated in Fig. 2.6. Normally the e_g orbitals are degenerated, but in a certain crystal environment the preference of one orbital can lead to a lowering of the energy.

Consider the situation in which the $d_{3z^2-r^2}$ orbital points into z-direction, like in Fig. 2.6 (a) and the $d_{x^2-y^2}$ is lying in the plane of the octahedron. An elongation of the Mn-O-bond in the z-direction would favor the $d_{3z^2-r^2}$ orbital, due to the decreased Coulomb repulsion between the oxygen ions. At the same time the octahedron becomes compressed within the xy-plane, which would enhance the Coulomb repulsion. The interplay between the energy lowering and the elastic strain leads to an energy minimum for a certain distortion. This distortion does not account for the Mn^{4+}-ion, since there is no such asymmetric occupation possible.

There are several possibilities of a Jahn-Teller distortion. The first is the dynamical one, which appears, if there are several energy minima between the system

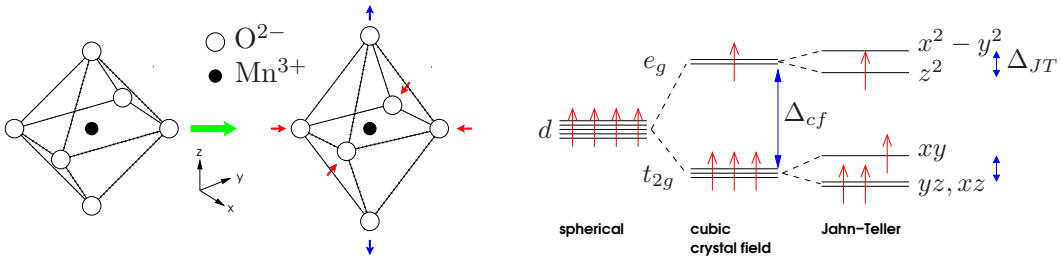

(a) Distortion of octahedron **(b)** Energy splitting

Figure 2.6.: The distortion of the oxygen octahedron by the Jahn-Teller effect (a). Energy diagram of the 3d-orbitals for the Jahn-Teller split Mn^{3+} ions (b). The crystal field splitting Δ_{cf} for an octahedral coordination in a cubic crystal field is marked, as well as the Jahn-Teller splitting Δ_{JT}.

can chose due to thermal or quantum transitions. The second is the cooperative Jahn-Teller distortion, which occurs in the case of a lot of Mn^{3+}-ions in the lattice. Then the distortions are not any more independent from each other and global structural changes are involved.

2.1.3. Magnetic properties, exchange mechanisms and orbital ordering

The interaction mechanisms in the manganites are very complicated and not known in all details, although there are a lot of theoretical studies [36, 35, 40, 43]. Here, only some basic exchange mechanisms (super exchange, double exchange) will be briefly summarized for an intuitive understanding of the possible interactions in the manganites and their connection to lattice effects. There are some more detailed mathematical considerations, e.g. [55], which consider these exchange interactions, but they are not shown here.

The exchange mechanism couples electronic with magnetic effects via the spin of the electron. The d-electrons can be most easily described by the Hubbard model [27, 54] without orbital degeneracy. Then the hamiltonian is

$$H = -\sum t_{ij} c^{+}_{i\sigma} c_{j\sigma} + U \sum n_{i\uparrow} n_{i\downarrow} \tag{2.3}$$

The first term stands for the possible electron hopping with the creation and annihilation operators $c_{i,j\sigma}$ for electrons at the sites i, j and spin σ and the hopping matrix element t_{ij}. The second term accounts for the Coulomb repulsion U between the electrons at the same site with the occupation number operators $n_{i\uparrow,\downarrow}$. For the non-interacting limit of $t \gg U$, only the hopping term is important and a metallic state is achieved. In the case of $t \ll U$ the situation is reversed and a strong interaction has to be taken into account. In the case of one electron per site ($n = 1$), the ground state is an insulator (with an energy gap of $E_g \sim U - t$). There is only a small probability of hopping, but the interaction of the localized moments, $s = \frac{1}{2}$, is important, since the virtual hopping can stabilize a certain configuration, although the electron is still localized. There are two possibilities shown in Fig. 2.7 (a), while the energy gain due to hopping only occurs for the right situation in (a).

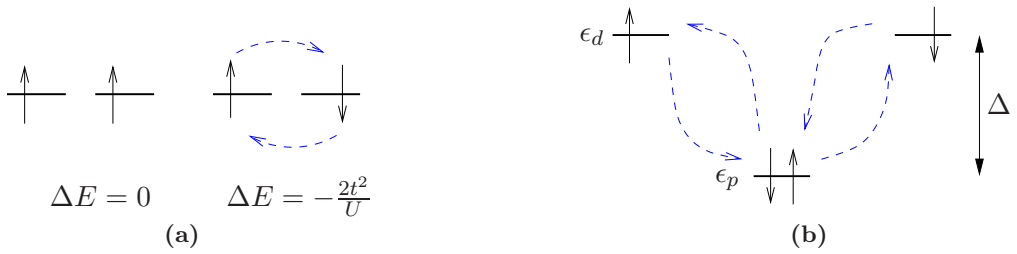

Figure 2.7.: Simple antiferromagnetic interaction between single occupied sites for an insulator with $U \gg t$ (a). Hopping between single occupied d-orbitals via oxygen p-orbitals (b).

Due to the virtual hopping, the degeneracy is lifted, since it can only take place for antiparallel alignment, since the hopping with parallel alignment is forbidden caused by the Pauli principle. The energy gain for antiparallel alignment is $\Delta E = -2t^2/U$ and therefore leads to the antiferromagnetic Heisenberg exchange interaction, called *superexchange* (SE). It can be described by the effective exchange Hamiltonian

$$H_{\text{eff}}^{\text{SE}} = J \sum \mathbf{S_i S_j}, \qquad \text{with} \qquad J = \frac{2t^2}{U}. \tag{2.4}$$

Of course this is only a very simple description, since in the hopping between the manganese atoms, also a hopping t_{pd} via the p-orbitals of the oxygen takes place (Fig. 2.7 (b)). The so called *charge-transfer* excitation energy $\Delta = \epsilon_d - \epsilon_p$ has to be considered. The case of $\Delta \gg U$ describes a Mott-Hubbard insulator and the oxygen states can be neglected, while the hopping is described by

$$J = \frac{2t_{pd}^4}{U\Delta} \qquad \text{with} \qquad t_{dd} = t = t_{pd}^2/\Delta. \tag{2.5}$$

The others for $\Delta \ll U$ (for $n = 1, \Delta \gg t$) are called charge-transfer insulators and the exchange becomes

$$J = \frac{2t_{pd}^4}{\Delta^2(2\Delta + U_{pp})}. \tag{2.6}$$

In the case of simple considerations there is no significant difference with respect to the magnetic properties. For more details about these insulators see [73, 36, 42]. Another issue which needs to be considered is usually the strong p-d-hybridization, which occurs due to the strong overlap between the e_g– and p–orbitals and forms some σ–orbitals. It leads also to a splitting of the d–orbitals and lifts the e_g–orbitals about t_{pd}^2/Δ. The t_{2g}–orbitals have only a weak overlap and therefore a weak hybridization with the p–orbitals. The hopping $t_{pd\sigma}$ depends on the angle of the O–Mn–O bond by roughly $t_{pd\sigma} = t_{pd}^0 \cos\theta$, while t_{pd}^0 stands for a 180° hopping.

So far, only the simplest case has been discussed. For an overlap of the orbitals via a 90° –path instead of 180° or other angles, also a weak ferromagnetic interaction might occur. Goodenough, Kanamori and Anderson formulated the GKA rules [21] to predict roughly the expected interactions. These rules are important for the

different magnetic ordering in the manganite lattice [12, 64]. There can be either the typical AF ordering, where each neighboring site has an opposite moment (G-type), the AF ordering can occur between the lattice planes (A-type) or there can be zig-zag chains with parallel moment, while the next chain has opposite moments (CE-type) etc., see Fig. 2.8.

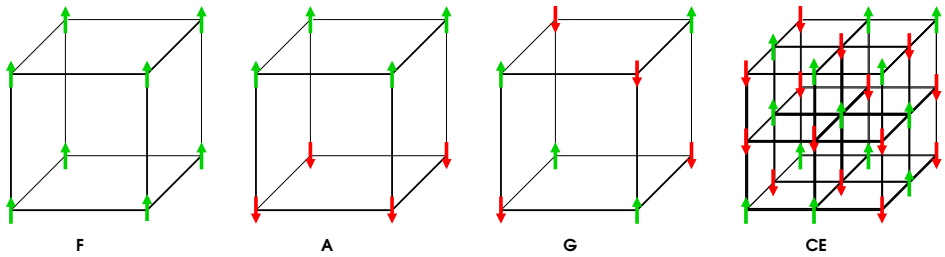

Figure 2.8.: Possible magnetic ordering modes for the Mn-site (B-site). Each arrow represents the local moment of a Mn-atom (for a better visualization the last structure is drawn for a larger group of cells). The letters below the structures denote the names of the mode.

The strong ferromagnetic ordering in the doped manganites is supposed to be caused by another exchange mechanism, the *double exchange* (DE). The doping creates Mn^{3+}– $[t_{2g}^3 e_g^1]$ and Mn^{4+}–ions $[t_{2g}^3]$, which add some "holes" to the electronic lattice. The electrons occupy each one d-orbital with a high-spin state due to the strong Hund's rule exchange J_H (compare Fig. 2.5). The electrons in the t_{2g}-orbitals can be considered as localized and have the core spin $S = \frac{3}{2}$. The additional electron in the Mn^{3+}–ion occupies one of the e_g–orbitals and can hop to another site, provided that the core spins are parallel. Treating this fact classically, the effective hopping can be written in terms of

$$t_{ij} \rightarrow t_{eff} = t \cos \frac{\theta_{ij}}{2} \tag{2.7}$$

where θ_{ij} is the angle between the spins of the sites i, j. For an antiferromagnetic arrangement $\theta_{ij} = \pi$ and $t_{eff} = 0$, but for a ferromagnetic system with $\theta_{ij} = 0$ the electron can move freely, since $t_{eff} = t$. Then, for a tight binding approximation, a band forms with an energy dispersion of

$$\epsilon(k) = -2t_{eff}(\cos k_x + \cos k_y + \cos k_z) \tag{2.8}$$

for a cubic lattice with lattice vectors $k_{x,y,z}$. Since the number of electrons is not very large they occupy mainly the lower edge of the band at $\epsilon_{min} = -6t_{eff}$. For the latter case the hamiltonian, including Hund's coupling, is

$$H^{DE} = -\sum t \cos \frac{\theta_{ij}}{2} c_i^\dagger c_j + J_H \sum \mathbf{S_i} \cdot \mathbf{S_j}. \tag{2.9}$$

The energy per site can be approximated to

$$E(\theta) = J_H S^2 \cos\theta - 6\, t\, x \cos \frac{\theta}{2} \tag{2.10}$$

(x is, as given above, the doping level) with a minimum in θ of

$$\cos\frac{\theta}{2} = \frac{3}{2}\frac{t}{J_H S^2}x. \tag{2.11}$$

Above the critical value $x > x_c = 2/3J_H S^2/t$ a ferromagnetic ordering is established. The hopping here is different, compared to the Mott insulators, since no activation energy is needed yielding a ferromagnetic state. It can be used to explain the change of the magnetic ordering with doping and the occurrence of metallicity with ferromagnetism.

The above discussed model is also referred as part of the one-orbital model [13], since only one orbital on each site was considered. It should be emphasized, that a lot of simplifications were made, to understand the basic mechanism. They can describe some of the situations quite well, but in reality the systems are much more complex. For instance in the last considerations the Jahn-Teller splitting, the other ions or other orbitals and the bond angles between the d- and p-orbitals have been neglected. Nevertheless these simple mechanisms give some insights into the understanding of the physics in manganites. For instance, the competition between antiferromagnetic (AF) and ferromagnetic (FM) ordering is revealed by the exchange mechanisms. The idea of the CMR is, that the additional electrons (holes) from the doping can move through the crystal, but are influenced by the localized spins.

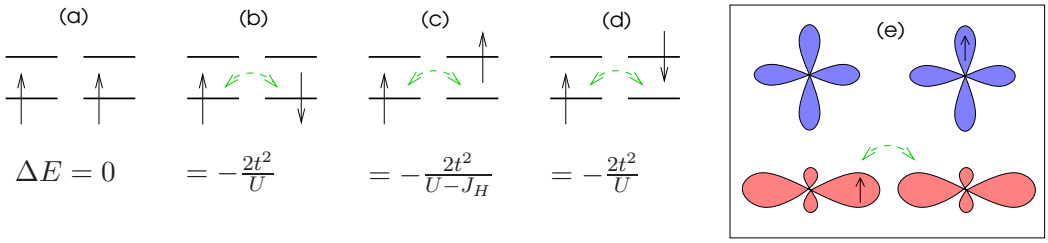

Figure 2.9.: One possible mechanism leading to orbital ordering: The interaction between two ions with two degenerate orbitals occupied with one electron can cause a ferromagnetic spin ordering coupled with an orbital ordering. Four possible situations (a-d) are shown, while (c) is the preferred one and could be compared to an ordering of the d_{e_g}-orbitals (e). The d_{z^2} orbital (red) should be oriented along the z-direction, while the others lie in the x-y-plane.

Another point is the orbital ordering [26]. Here an example, which can also be explained by the superexchange in a two-orbital model [13], is given. In the case of orbital degeneracy of the ions, for example two ions with two degenerate orbitals occupied by one electron, can lead to a preferred ordering due to energy lowering. The two orbitals are named by 1 and 2 and it is assumed that only diagonal hopping is allowed, that is $t_{i=j} = t$ and $t_{i\neq j} = 0$. This can for instance reflect the situation of two d_{e_g}-orbitals with the d_{z^2} orbitals pointing towards each other and overlap, while the others are orthogonal. It is demonstrated in Fig. 2.9, in which four different possibilities are shown, but only the third one (c) is most

probable for energetic reasons. Here, since the Hund's coupling energy is gained $U \gg J_H$, a weak ferromagnetic spin ordering ($J_H \ll 1$) is preferred together with the orbital ordering. The latter occurs quite often in manganites and is therefore an important issue.

The one- and two-orbital models have been widely discussed [13, 14] and used for model calculations within the physics of manganites. In these models already the different influences of the Coulombic, antiferromagnetic and ferromagnetic interactions can be taken into account to form reasonable phase diagrams. On the other hand, the situation is much more complex and it is difficult to separate the different contributions from each other. An example for an even more detailed analysis with a complex consideration of the electronic effects is the LDA+U method [7, 6] (*local density of states calculation*, taking the Coulomb interaction into consideration) and also in combination with the DMFT (*dynamical mean-field theory*) method [47, 20, 30, 43].

2.1.4. Beyond the simple mechanisms: Polarons

The simple models, introduced so far, are usually not sufficient to explain the complex properties of the manganites. In particular, magnetic ordering can be observed together with very different transport properties, like a FM state coupled together either with a metallic or insulating state, or an AF state which is metallic [4]. The radius of the ions used for doping, and the concomitant lattice distortions do not scale linearly with the resistivity [17]. Moreover the residual resistivities at low temperatures ($T \cong 4.2\,\mathrm{K}$) are quite different. It is important to consider further mechanisms [50].

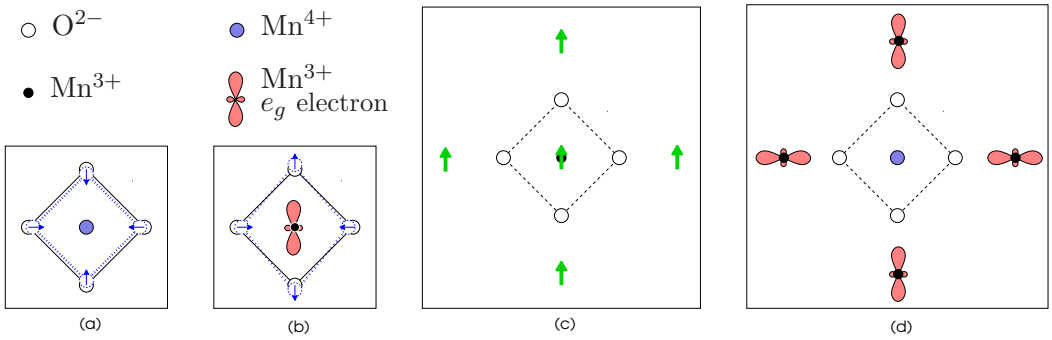

Figure 2.10.: Schematic representation different types of polarons: dielectric polaron (a), Jahn-Teller polaron (b), spin (magnetic) polaron (c) and orbital polaron (d).

One of them is the electron-lattice interaction. The hopping of the electron between the Mn-sites, influenced by the phonons, can be regarded within the polaron model, for instance as (Jahn-Teller-) polarons. The formation of polarons is indicated by large effective masses and a thermally activated charge carrier transport. A polaron can be regarded as a small region with a lattice distortion, caused by the localized electron or hole. This local short range correlation of the environment with the electron can move with it through the lattice [54] and manifests in the transport properties through a temperature activated hopping mechanism.

There are different kinds of polarons: the dielectric, Jahn-Teller and spin and orbital polaron. The first is probably the most simplest case; due to the different ionic radii of differently charged ions (e.g. Mn^{4+} is smaller compared to Mn^{3+}) a distortion can occur and the surrounding ions move towards the ion with smaller radius, as shown in Fig. 2.10 (a). Also a bound pair like a bipolaron or Zener polaron can be formed [71, 18]. With the Jahn-Teller polaron a Jahn-Teller distortion is bound to the electron (hole), Fig. 2.10 (b). A magnetic or spin polaron (c) consists of an electron with its spin and the surrounding, which is forced to have a parallel spin. The last one mentioned is the orbital polaron (d) [37], in which the orbitals take on a specific orientation with respect to the electron (hole). Additionally one differs between small and large polarons. The first is reduced to a single site, while the second describes an extension, which is larger than a lattice spacing. In manganites polarons were already seen experimentally, but are still an issue of controversial discussions [1, 63, 32], since their role with respect to the transport is not finally clarified.

Above T_C the activated transport behavior was very clearly associated with polarons, since the resistivity followed an activated insulating like behavior with temperature, that is $\rho \sim \exp(T_0/T^{1/4})$ [68]. Some papers report on the correlated polarons, observed by X-ray scattering or small angle neutron diffraction [16, 1, 39] For the low temperature metallic phase also indications of polarons are given – at least nearby the MIT – and discussed controversially [25]. The nature of the polarons is not clear in detail, though a magnetic character is expected due to the large resistance changes around T_C. At least some spin correlations were observed for LCMO $x = 0.3$ [44] and Jahn-Teller polarons are indicated by the temperature dependent anomalies in the lattice parameters around T_C in various compounds with $x \approx 0.3$ [57]. Regarding the CMR effect, a magnetic field might suppress the formation of polarons. It has also been reported, that the occurrence of correlated polarons can be attributed with an orthorhombic structure, but not with the rhombohedral one [39].

2.2. Phase separation

From the DE mechanism (Sec. 2.1.3, Eq. 2.11) a kind of spin canting as a function of doping x would be expected from the calculations. This is a controversial issue, since the compressibility is $-d^2E/dx^2 < 0$ and gives a hint for an instability towards phase separation into FM metallic and AF insulating phases [33], which has been already shown experimentally. Also the two-orbital model gives hints for a phase separation with Jahn-Teller phonons taken into account [14].

In general, phase separation means that two competing phases coexist in the compound. The different phases are characterized by different symmetry braking patterns, which are based on the spin, charge and orbital patterns in manganites. Here a ferromagnetic ordered phase competes with a spin antiferromagnetic or charge ordered phase. In terms of manganites a phase does not necessarily consist of regions with a large number of electrons, which would be the case for a strict thermodynamic definition, but small clusters on the scale of the lattice spacing are

expected from the models, like for example the double exchange mechanism with long range Coulomb interactions [13]. On the other hand experimentally also phase separation within the micrometer range were found.

Calculating the phase separation and modeling the transport properties is quite a demanding task. The probably most prominent phenomenological model for phase separation is the two resistor model by Mayr et al. [45]. It is a percolative model of two phases, an insulating and metallic like, with the relative amount of phases p (relative fraction of metallic resistances). In models of this kind, percolation paths of the one phase in between parts of the other are important for the properties. If there is a path through the network, which consists of the metallic phase, then the sample becomes metallic, Fig. 2.11 (a). The more of these paths become disconnected with increasing temperature, the more insulating the sample state is. A mathematical description about percolation can be found in [23, 13]. The model here uses two phases with two different resistivities, namely an insulating one with R_I with an increasing resistivity with decreasing temperature, see Fig. 2.11 (a-c), and the effective resistance R_M^{per} representing the metallic like state via the percolation paths with an increasing resistance with temperature and a large residual resistance due to the complex network of percolation paths. The critical and therefore most interesting values for percolation are $p = 0.5$ in a two-dimensional and $p = 0.25$ in a three-dimensional model [13].

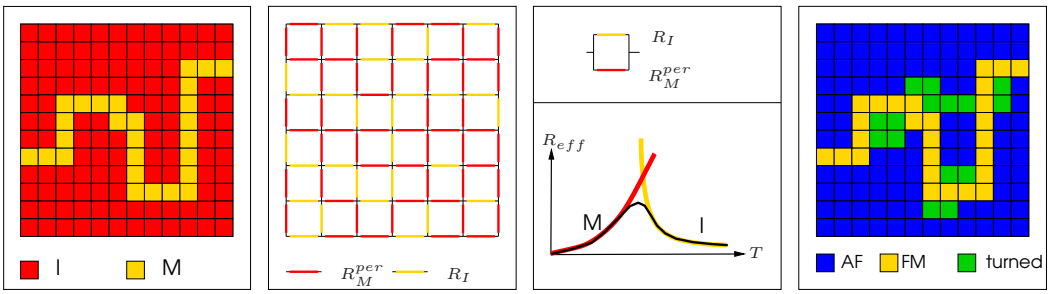

Figure 2.11.: The percolation model of Mayr et al. for phase separation : In between a matrix of insulating parts (I) metallic percolation paths (M) can form (effective resistor network approximation) (a). Schematics of a resistor network (b) of insulating R_I and effective metallic R_M^{per} resistances representing the two phases for the calculation of the global resistance R_{eff} as a function of temperature (c). Regions with AF and FM ordering for a Monte Carlo simulation with disorder, with AF regions turned (turned) from AF to FM ordering under an applied field (d).

The overall transport characteristic of the manganite is then the global calculated resistance and leads to the typical peaked resistance curve as a function of temperature for the metal insulator transition. For the simulation a random network of squares which are associated with either of the two resistivities is used, including ideal leads. For the resistivities realistic values from Uehara et al. [66] for a $(La_{1-y}Pr_y)_{1-x}Ca_xMnO_3$ system were used. The simulated resistivity curves

qualitatively reflect the features of the MIT in manganites and also the insulating behavior over the full temperature range for constant p-values. The model describes the situation sufficiently well, but could be improved in detail. This was also done by Mayr in fact, by varying p with the temperature and lead to a much more pronounced peak in the resistivity curves [45].

Another approach comes from Moreo et al. [52], in which disorder plays a crucial role. Since the chemical doping alters the arrangements within the crystalline structure with respect to bonding angles and distortions, also a corresponding distribution of hopping matrix elements per site is expected, which leads to the different regions. Moreo did some Monte Carlo simulations for the one– and two–orbital models in which some disorder was added. In the vicinity of a first-order transition, two different limits are interesting: For very strong disorder, clusters with the size of a few lattice spacings were found, while in the case of weak disorder also much larger clusters emerge, since too many interfaces would cost too much energy.

A similar result with respect to the domain sizes was obtained for a corresponding Random Field Ising Model [52]. This model considers a hamiltonian of

$$H = -J \sum_{ij} S_i^z \cdot S_j^z - \sum_i h_i \cdot S_i^z \tag{2.12}$$

with the Ising variables $S_i^z = +1, -1$ arranged locally according to the random field h_i. A system with only ferromagnetic interactions would prefer a uniform ordering in this case with a first-order phase transition, but the added disorder parameter with the random field introduces small clusters into the system, even at low temperatures $T < T_C$. In this case the different regions have either spin up or spin down configuration and the main issue is to determine the cluster sizes with respect to the disorder. The tendency of avoiding interfaces leads to a separation with some clusters of varying size with h for small h, very small clusters for a large h and huge clusters for small h/J. By switching on an external magnetic field H, some narrow parts of the spin down regions flip into spin up regions such that the latter grow in size, Fig. 2.11 (d). The three dimensional case of this model shows a different result. Then a strong disorder would lead to large clusters while the weak disorder tends to a more or less uniform state.

Another approach [59, 34] considers the phase-separation with especially regarding the Jahn-Teller distortions. It was found that there are less itinerant charge carriers than the doping level would suggest. Like the other models mentioned so far, the latter can mainly describe nanoscale phase-separation, which does not seem to be sufficient to describe the experimental results. Ahn et al. [3] consider strain effects within the sample and argue with an intrinsic elastic energy landscape causing the micrometer scale multiphase separation. These considerations differ from the others with respect to the lattice degrees of freedom and electron-lattice couplings. It says that the phase separation is driven by the self-organization of elastic inhomogeneities. On the other hand, again a percolative result is obtained for the application of a magnetic field, which induces current paths in the sample. In this

model also the phases are distinct by a ferromagnetic metallic state (here denoted as the undistorted state) and an insulating (distorted) state, which produces a gap in the DOS. Another view is given by Milward et al. [51], who talks about electronically soft phases. The Ginzburg-Landau theory is used with the magnetization $M(r)$ and the charge-orbital modulation $\Psi_{CO} = A(r)\exp\left[i(\mathbf{Q_c}r + \Phi(r))\right]$[3] as order parameters in the free energy density. The competition between the phases is given here between the magnetic order and charge modulation in new thermodynamic phases. Since the charge disproportionation between the Mn ions is not necessarily unity, this model emphasizes a less localized charge-density wave picture.

In contrast to the other models, the latter considers a continuous phase transition, which would not show phase separation or a percolative picture of the phases. On the other hand the authors emphasize that a localized phase separation could exist due to strain or disorder. Additionally the orbital ordering is described in a simple way, which does not involve different kinds of ordering. The other models introduced so far, normally emanate from a first order, that is, a discontinuous phase transition. This question is still under debate and depending on the model either kind of the transition is possible. None of the models can predict a full picture of the manganites, because always some simplifications had to be made in order to calculate or simulate the properties of the manganites. On the other hand it is clear for everybody that there is a very strong interplay between the different mechanisms in the manganites and neglecting a small part could already change the picture. This is the reason why experiments considering this issue are still necessary to reveal more about the manganite physics. In the next section some of the experimental results with respect to LCMO will be given as a short overview.

2.3. The case of LCMO

In the following a short summary of the properties of LCMO is given. This includes the basic properties and some newer results of intrinsic mechanisms in LCMO. The part about phase separation, for which already experiments and the respective publications exist, is displaced into the discussion with the results obtained in this work.

The peculiarity in LCMO is, that the ionic radius of Ca $r_{\mathrm{Ca}} \cong 1.14\,\text{Å}$ is very similar to that of La $r_{\mathrm{La}} \cong 1.172\,\text{Å}$ [61] and a true solid solution is possible over the entire doping range x. The phase diagram is given in Fig. 2.12 [11]. It is similar to $La_{1-x}Sr_xMnO_3$, which only exists up to $x \approx 0.6$. The CMR can be observed for Ca concentrations of $0.2 \leq x \leq 0.5$, coupled to a transition from a ferromagnetic metal to a paramagnetic insulator.

The structure is normally orthorhombic for all doping levels below approximately 700 K. In the very low doping ($x < 0.2$) and very high doping ($x > 0.8$) regions the properties are less clear than in between, which might be associated to the role of oxygen excess and deficiency observed for the end regions respectively. The largest

[3] r spatial coordinate, A amplitude of modulation, $\mathbf{Q_c} = a^*/n$ wave vector commensurate with lattice with a^* as reciprocal lattice vector, n integer, Φ phase incorporating structures with incommensurate periodicities.

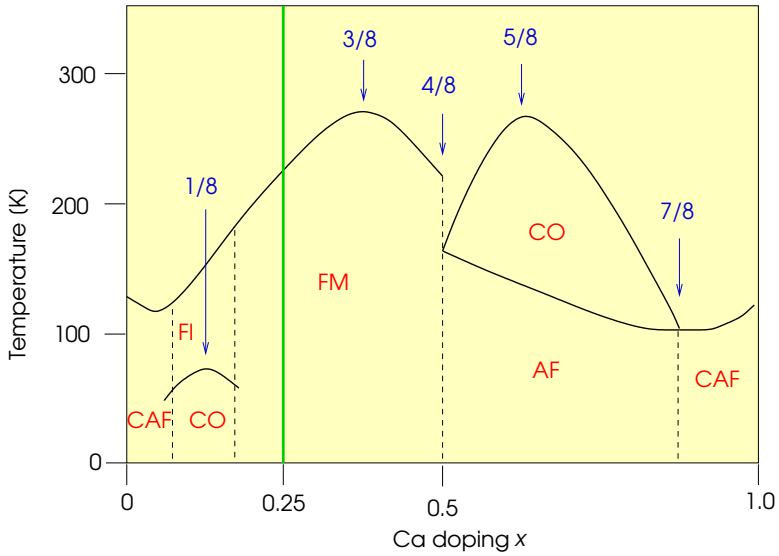

Figure 2.12.: Phase diagram from $La_{1-x}Ca_xMnO_3$. Numbers in blue denote special (commensurate) concentrations which show anomalies. The green line indicates the composition used for this work. FM: Ferromagnetic metal, FI: Ferromagnetic insulator, AF: Antiferromagnet, CAF: Canted antiferromagnet, CO: Charge/orbital ordered state. Redrawn according to [11].

regions show either a ferromagnetic metallic or an antiferromagnetic insulating low temperature phase, while the latter undergoes also a charge/orbital ordering transition. Some special points can be seen in the phase diagram, marked by the blue numbers, for commensurate electron concentrations. These might be the important hint to electron-lattice coupling in mixed-valent manganites. At these points either the critical temperature of the transition is largest ($x = 1/8, 3/8, 5/8$) or an abrupt change of the sample properties can be observed with a critical competition between the neighboring ordering phenomena ($x = 4/8, 7/8$). Remarkably there is an asymmetry between hole and electron doping of the end members $LaMnO_3$ and $CaMnO_3$.

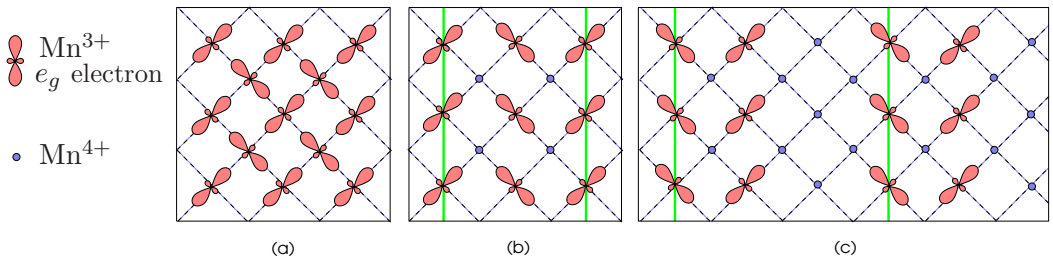

Figure 2.13.: Charge and orbital ordering in $La_{1-x}Ca_xMnO_3$ with $x = 0$ (a), $x = \frac{1}{2}$ (b), $x = \frac{2}{3}$ (c). The green bars mark the periodicity of the formed charge stripes.

The charge and orbital ordered lattice [53, 10], was first observed for $x \geq 0.5$, but

it can also occur in lower doping regions (see below). The e_g–orbitals of the Mn^{3+}–ions are arranged in a zigzag pattern with an adjacent number of Mn^{4+}–ions in between. This ordering is shown in Fig. 2.13 for some commensurate compositions. For $x = 0$ the typical AF pattern of $LaMnO_3$ is seen, but it is coupled to an orbital ordering of the e_g orbitals. For the higher commensurate doping charge stripe patterns develop. In between these doping levels an interplay of the adjacent stripe phases leads to a mixed pattern.

The compound used here ($La_{0.75}Ca_{0.25}MnO_3$), is situated in the CMR region with a transition of a ferromagnetic metal to a paramagnetic insulator (see also the general properties introduced at the beginning of this chapter). It has a tolerance factor of about $f \approx 0.89$ calculated from the average ionic radii [61]. The structural properties were intensively regarded by Radaelli et al. [57] for polycrystalline bulk samples. The authors found an orthorhombic structure with space group P_{nma}. At the MIT at $T_C = 240\,\mathrm{K}$, it shows an interesting anomaly. A small structural change, which is manifested in the change of the Mn-O bond lengths, although the crystal structure is maintained, takes place. The average bond length <Mn-O> is strongly increased with temperature and then, above T_C, the curve is abruptly changed to a more or less linear shape with a much smaller slope, see Fig. 2.14 (a). Concurrently the coherent Jahn-Teller distortion, determined by

$$\sigma_{JT} = \sqrt{1/3 \sum_i [(Mn-O)_i - < Mn-O >]^2}, \tag{2.13}$$

shows a kink around T_C (Fig. 2.14 b), while the JT distortion in the apically elongated type can be as large as that for $LaMnO_3$. Additionally the Mn-O bond angles are decreasing with temperature within a range of 200 K up to T_C and then are increasing again. Due to the oxygen Debye-Waller factors also an indication of incoherent JT distortions above T_C is given, this is ascribed as indication of present static disorder [57].

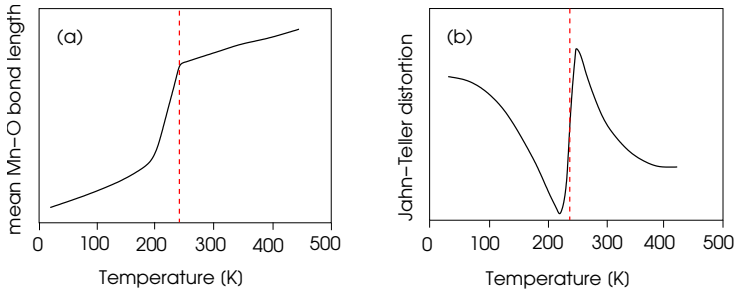

Figure 2.14.: Mean Mn-O bond length for $La_{0.75}Ca_{0.25}MnO_3$ as a function of temperature (a), σ_{JT} for $La_{0.75}Ca_{0.25}MnO_3$ (b). The broken lines mark T_C. For further details see reference [57].

The question of the order of the phase transition has also been examined experimentally. It can give a hint on the kind of phase transition and accordingly phase separation, but the results are still controversial and probably depend on the sample fabrication. For example Kim et al. [38] observed different transitions

for $La_{1-x}Ca_xMnO_3$ polycrystalline samples and found a first-order transition for $x = 0.33$ expressed by a small discontinuity in the magnetization and volume expansion, determined from the Clausius-Claperon equation. On the other hand the $x = 0.4$ sample showed a second-order transition for which the tricritical point exponents were identified. This group claims that $La_{1-x}Ca_xMnO_3$ tends to a first-order transition for $x < 0.4$ and a second-order transition for $x > 0.4$. In contrast to these observations Yanagisawa et al. [72] find a second-order transition in $La_{1-x}Ca_xMnO_3$ with $x = 0.35$ by electron paramagnetic resonance. Souza et al. [62] analyzed the phase transition of $La_{1-x}Ca_xMnO_3$ with $x = 0.3$ as a polaronic compound with a second-order transition. Again others report about a transition somewhere in between [56], which is neither exactly first or second order.

As already mentioned before, a simple mechanism is not sufficient to describe the manganites, which also applies to LCMO [15]. Also polarons might play an important role. Some neutron scattering experiments on $La_{1-x}Ca_xMnO_3$ give hints to polaron formation [44, 2]. The spin and charge dynamics leads to a formation of correlated polarons, which is consistent with the formation of charge stripes. An oxygen isotope effect (by replacing ^{16}O by ^{18}O) underlines the importance of electron lattice couplings.

Finally it should be mentioned that the properties observed for bulk samples do not necessarily have to be exactly the same as for thin films. Regarding thin films deposited on a substrate the lattice mismatch between the crystalline substrate and the thin film structure has to be taken into consideration as well. Due to stress or strain in the film, the critical temperatures can be shifted and the residual resistivity can be different, and the reduced size or film thickness effect the properties of thin films [49]. These issues will be discussed at the end of this work with respect of the samples used in this thesis.

Bibliography

[1] C. P. Adams, J. W. Lynn, Y. M. Mukovskii, A. A. Arsenov, and D. A. Shulyatev. *Phys. Rev. Lett.*, 85(18):3954, 2000.

[2] C. P. Adams, J. W. Lynn, V. N. Smolyaninova, A. Biswas, R. L. Greene, W. Ratcliff II, S.-W. Cheong, Y. M. Mukovskii, and D. A. shulyatev. *Phys. Rev. B*, 70:134414, 2004.

[3] K. H. Ahn, T. Lookman, and A. R. Bishop. *Nature*, 428:401, 2004.

[4] T. Akimoto, Y. Manyama, Y. Moritomo, A. nakamura, K. Hirota, K. Oboyama, and M. Ohashi. *Phys. Rev. B*, 57:R5594, 1998.

[5] P. W. Anderson and H. Hasegawa. *Phys. Rev.*, 100:675, 1955.

[6] V. I. Anisimov, F. Aryasetiawan, and A. I. Lichtenstein. *J. Phys.: Cond. Mat.*, 9:767, 1997.

[7] V. I. Anisimov, J. Zaanen, and O. K. Anderson. *Phys. Rev. B*, 44:943, 1991.

[8] K. Chahara, T. Ohno, M. Kasai, and Y. Kozono. *Appl. Phys. Lett.*, 63:1990, 1999.

[9] A. Chainami, M. Mathew, and D. D. Sarma. *Phys. Rev. B*, 47:15397, 1993.

[10] C. H. Cheong, S.-W. Cheong, and H. Y. Hwang. *J. Appl. Phys.*, 81:4326, 1997.

[11] S.-W. Cheong and H. Y. Hwang. *Colossal-magnetoresistive oxides*, chapter 7. Ferromagnetism vs. Charge/Orbital Ordering. Gordon and Breach Science Publisher, 200.

[12] J. M. D. Coey, M. Viret, and S. von Molnár. *Adv. Phys.*, 48:167, 1999.

[13] E. Dagotto. *Nanoscale Phase Separation and Colossal Magnetoresistance.* Springer Verlag Berlin Heidelberg, 2003.

[14] E. Dagotto, T. Hotta, and A. Moreo. *Phys. Rep.*, 344:1, 2001.

[15] P. Dai, J. A. Fernandez-Baca, E. W. Plummer, Y. Tomioka, and Y. Tokura. *Phys. Rev. B*, 64:224429, 2001.

[16] Pengcheng Dai, J. A. Fernandez-Baca, N. Wakabayashi, E. W. Plummer, Y. Tomioka, and Y. Tokura. *Phys. Rev. Lett.*, 85(12):2553, 2000.

[17] F. Damay, A. Maignan, C. Martin, and B. Raveau. *J. Appl. Phys*, 81:1372, 1997.

[18] A. Daoud-Aladine, J. Rodriguez-Carvajal, L. Pinsard-Gaudart, M. T. Fernández-Diaz, and A. Revcolevschi. *Phys. Rev. Lett.*, 89:097205, 2002.

[19] P.-G. de Gennes. *Phys. Rev.*, 118:141, 1960.

[20] A. Georges and G. Kotliar. *Phys. Rev. B*, 45:6479, 1992.

[21] J. B. Goodenough. *Magnetism and chemical bond*. Interscience Publishers, New York, 1963.

[22] L. P. Gor'kov and V. Z. Kresin. *Phys. Rep.*, 400:149, 2004.

[23] G. Grimmelt. *Percolation*. Springer, 1999.

[24] R. Gross and A. Marx. Spinelektronik. Lecturenotes from http://www.wmi.badw.de/teaching/Lecturenotes/, Walther-Meissner-Institut, Garching, 2004.

[25] Ch. Hartinger, F. Mayr, A. Loidl, and T. Kopp. *Phys. Rev. B*, 73:024408, 2006.

[26] T. Hotta. *Rep. Prog. Phys.*, 69:2061–2155, 2006.

[27] J. Hubbard. Electron correlations in narrow energy bands. *Proc. Roy. Soc. A*, 276:238, 1963.

[28] M. Imada, A. Fujimori, and Y. Tokura. *Rev. Mod. Phys.*, 70:1039, 1998.

[29] H. A. Jahn and E. Teller. *Proc. Royal Soc. London A*, 161:220, 1937.

[30] M. Jarrell. *Phys. Rev. Lett.*, 69:168, 1992.

[31] G. H. Jonker. *Physica*, 22:707, 1956.

[32] Ch. Jooss, L. Wu, T. Beetz, R. F. Klie, M. Beleggia, M. A. Schofield, S. Schramm, J. Hoffmann, and Y. Zhu. *Proc. Natl. Acad. Sci.*, 2007.

[33] M. Yu. Kagan, D. I. Khomskii, and M. V. Mostovoy. *Eur. Phys. J. B*, 12:217, 1999.

[34] M. Yu Kagan and K. I. Kugel. *Physics-Uspekhi*, 44:553, 2001.

[35] D. Khomskii. Electronic structure, exchange and magnetism in oxides. In M. J. Thornton and M. Ziese, editors, *Spin electronics*, volume 569 of *Lecture notes in physics*, 2001.

[36] D. Khomskii and G. Sawatzky. *Solid State Comm.*, 102:87, 1997.

[37] R. Kilian and G. Khaliullin. *Phys. Rev. B*, 60:13458, 1999.

[38] D. Kim, B. Revaz, B. L. Zink, F. Hellman, J. J. Rhyne, and J. F. Mitchell. *Phys. Rev. Lett.*, 89:227202, 2002.

[39] V. Kiryukhin, T. Y. Koo, H. Ishibashi, J. P. Hill, and S-W. Cheong. *Phys. Rev. B*, 67(6):064421, 2003.

[40] E. Koch. Correlated electrons. In S. Blügel, Th. Brückel, and C. M. Schneider, editors, *Magnetism goes Nano*, volume 36 of *Spring School of the Institute of Solid State Research*. Forschungszentrum Jülich GmbH, Institut für Festkörperforschung, 2005.

[41] R. M. Kusters, J. Singleton, D. A. Keen, R. McGreevy, and W. Hayes. *Physica B*, 155:362, 1989.

[42] A. I. Lichtenstein. Electronic structure of magnetic oxides. In P. H. Dederichs, P. Grünberg, and R. Hölzle, editors, *Magnetische Schichtsysteme*, volume 30 of *Spring School of the Institute of Solid State Research*. Forschungszentrum Jülich GmbH, Institut für Festkörperforschung, 1999.

[43] A. I. Lichtenstein. Electronic structure of complex oxides. In S. Blügel, Th. Brückel, and C. M. Schneider, editors, *Magnetism goes Nano*, volume 36 of *Spring School of the Institute of Solid State Research*. Forschungszentrum Jülich GmbH, Institut für Festkörperforschung, 2005.

[44] J. W. Lynn and C. P. Adams. *J. Appl. Phys.*, 89:6846, 2001.

[45] M. Mayr, A. Moreo, J. A. Verges, J. Arispe, A. Feiguin, and E. Dagotto. *Phys. Rev. Lett.*, 86:135, 2001.

[46] M. McCormack, S. Jin, T. H. Tiefel, R.M. Fleming, and J.M. Phillips. *Appl. Phys. Lett.*, 64:3045, 1994.

[47] W. Metzner and D. Vollhardt. *Phys. Rev. Lett.*, 62:324, 1989.

[48] H. P. Meyers. *Introductory Solid State Physics*. Taylor & Francis, 1997.

[49] A. J. Millis, T. Darling, and A. Migliori. *J. Appl. Phys.*, 83:1588, 1998.

[50] A. J. Millis, P. B. Littlewood, and B. I. Shraiman. *Phys. Rev. Lett.*, 74:5144, 1995.

[51] G. C. Milward, M. J. Calderón, and P. B. Littlewood. *Nature*, 433:607, 2005.

[52] A. Moreo, M. Mayr, A. Feiguin, S. Yunoki, and E. Dagotto. *Phys. Rev. Lett.*, 84, 2000.

[53] S. Mori, C. H. Chen, and S.-W. Cheong. *Nature*, 392:473, 1998.

[54] N. F. Mott. *Metal insulator Transitions*. Taylor & Francis, 1997.

[55] W. Nolting. *Quantentheorie des Magnetismus*, volume Teil 1 - Grundlagen. B. G. Teubner Stuttgart, 1986.

[56] P. Novák, M. Maryško, M. M. Savosta, and A. N. Ulyanov. *Phys. Rev. B*, 60:6655, 1999.

[57] P. G. Radaelli, G. Iannone, M. Marezio, H. Y. Hwang, S.-W. Cheong, J. D. Jorgensen, and D. N. Argyriou. *Phys. Rev. B*, 56:8265, 1997.

[58] M. B. Salamon and M. Jaime. *Rev. Mod. Phys.*, 73:583, 2001.

[59] A. O. Sboychakov, K. I. Kugel, and A. L. Rakhmanov. *Phys. Rev. B*, 74:014401, 2006.

[60] C. W. Searle and S. T. Wang. *Can. J. Phys.*, 47:2023, 1969.

[61] R. D. Shannon. *Acta. Cryst.*, A 32:751, 1976.

[62] J. A. Souza, Y.-K. Yu, J. J. Neumeier, H. Terashita, and R. F. Jardim. *Phys. Rev. Lett.*, 94:207209, 2005.

[63] L. Sudheendra, V. Moshnyaga, E. D. Mishina, B. Damaschke, Th. Rasing, and K. Samwer. *Phys. Rev. B*, 75:172407, 2007.

[64] Y. Tokura, editor. *Colossal-magnetoresistive oxides*. Gordon and Breach Science Publishers, 2000.

[65] Y. Tokura. *Rep. Prog. Phys*, 69:797, 2006.

[66] M. Uehara, S. Mori, C. H. Chen, and S.-W. Cheong. *Nature*, 399:560, 1999.

[67] J. H. van Santen and G. H. Jonker. *Physica*, 16:599, 1950.

[68] M. Viret, L. Ranno, and J. M. D. Coey. *Phys. Rev. B*, 55(13):8067, 1997.

[69] R. von Helmolt, J. Wecker, B. Holzapfel, L. Schultz, and K. Samwer. *Phys. Rev. Lett.*, 71:2331, 1993.

[70] E. O. Wollan and W. C. Koehler. *Phys. Rev.*, 100:545, 1955.

[71] L. Wu, R. F. Klie, Y. Zhu, and Ch. Jooss. *Phys. Rev. B*, 76:174210, 2007.

[72] O. Yanagisawa, M. Izumi, K.-H. Huang, W.-Z. Hu, Y. Shen, K. Nakanishi, Y. Takahashi, and H. Nojima. *J. Magn. Magn. Mat.*, 211:254, 2000.

[73] J. Zaanen, G. A. Sawatzky, and J. Allen. *Phys. Rev. Lett.*, 55:418, 1985.

[74] C. Zener. *Phys. Rev.*, 82:403, 1951.

3. Scanning tunneling microscopy and spectroscopy – Fundamental considerations

Scanning tunneling microscopy (STM) has developed into a standard technique to analyze sample surfaces of metals and semiconductors on a very local scale, down to subatomic dimensions. The concept of the STM is based on the measurement of the tunneling current between a metallic tip and the sample. Since the tunneling current is exponentially dependent on the tip-sample separation, it is very sensitive to any height changes.

The STM has been first developed by Binning and Rohrer [3, 4] in 1982 with the idea of a microscope to observe the topography locally. In more detail, the tunneling current depends on the local electronic structure of the tip and the sample which invented much more related applications in the past decades. An example is the additional electronical and even chemical analysis of a surface with the spectroscopy modes. In comparison with other spectroscopy techniques the advantage of *scanning tunneling spectroscopy* (STS) is again the determination of localized features, e.g. surface states and band gaps, on an atomic scale, although the interpretation is non-trivial.

The concepts of the STM and STS techniques will be described briefly in the following. For a more comprehensive review, the author would also like to refer to the relevant literature, since it has grown to a large field of research with respect to the development of the technique itself as well as the interpretation of the results achieved. Some well known examples are the books by Wiesendanger et al. [10] and further references like [6, 2, 18].

3.1. Basic concepts of STM

The functional principle of an STM is based on the quantum mechanical tunneling effect, which appears between two electrodes separated by an insulating ("forbidden") region, that is a barrier of height U. An electron with energy $E < U$ situated in one of the electrodes, has a small probability of being found in the other electrode due to its wave function, which decays exponentially inside the barrier. The tunneling can occur (in case of sufficiently overlapping wave functions of the electrons in both electrodes) from both sides of the electrodes of the tunnel junction, but the net tunneling current is zero for zero bias. If a voltage is applied to the electrodes a net tunnel current can flow through the junction (for the tunneling effect in detail, see the basic literature of quantum mechanics and for example [19, 9, 8]).

In the one-dimensional case of the semi-classical WKB[1] approximation, the resulting probability of for example an electron of the tip being localized in the sample at position z is

$$|\Psi(z)|^2 = |\Psi(0)|^2\, e^{-2\kappa z} \tag{3.1}$$

with

$$\kappa = \sqrt{\frac{m_e}{\hbar^2}\,(\Phi_t + \Phi_s - eV)}, \tag{3.2}$$

in which m_e is the electron mass and $\Phi_{s/t}$ are the work functions for the two electrodes. It is evident that the tunneling probability $I \propto |\Psi(z)|^2$ is exponentially dependent on the tip-sample separation, (lying in the z-direction)

$$I \propto e^{-\kappa z}. \tag{3.3}$$

Taking reasonable values for a metallic tunneling system with work functions about 4-5 eV [11], then $\kappa \approx 10\,\mathrm{nm}^{-1}$, which means that a change in z of about 0.1 nm alters the tunneling probability by about one order of magnitude.

In the STM the tunneling system is built out of a sharp metallic tip and the sample as electrodes and the (air or vacuum) gap between both as the tunneling barrier. Since our microscope was operated under *ultra high vacuum* (UHV) conditions, here only the vacuum tunneling through a vacuum gap is of interest. Via scanning the tip in $x-y-$direction above the surface, the local variation of the tunnel current is used in an STM to image the surface or the electronic properties of the surface due to its exponentially dependence $I(z)$. Ideally, it is usually assumed that the tunneling current flows between the outermost apex atom of the tip and the sample surface atoms leading to a highly corrugated tunneling current distribution and therefore atomic resolution can be achieved. For a schematic view see Fig. 3.1, the technical realization is described in Chap. 5. The materials probed need to be metallic or semiconducting. At first, for the interpretation of the STM measurements it is important to understand, which parameters enter the tunneling equation.

The tunnel current between the sample (s) and the tip (t) depends on their electronic structure, which can be locally different. The diagram in Fig. 3.2 demonstrates the tunneling situation. Electrons can tunnel from each side of the barrier, but with a bias V applied a net tunneling current towards the lower potential side is flowing. (In the convention used here, a positive voltage applied to the sample means, that the Fermi energy of the tip E_{F_t} is increased with respect to the Fermi energy of the sample E_{F_s}.) Electrons can only tunnel from occupied states of the one electrode to appropriate empty states of the other electrode. Fig. 3.2 only shows the simple picture for $T = 0$, the filling of the states is sharply limited by the Fermi energy E_F. For higher temperatures this border is broadened, and the occupation probability of a state is described by the Fermi-Dirac distribution function

$$f(E) = (1 + \exp\,[E/k_B T])^{-1}. \tag{3.4}$$

[1] WKB means Wentzel-Kramers-Brillouin-Jeffreys approximation.

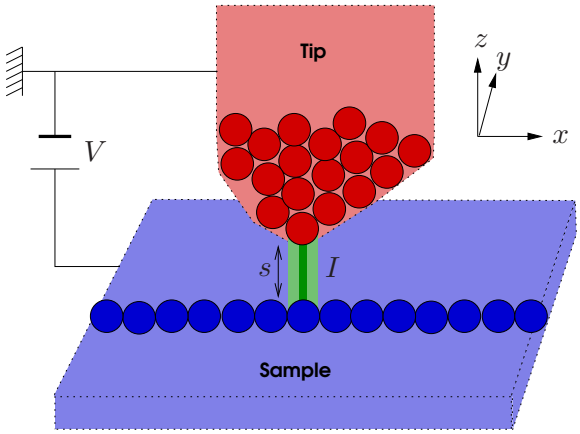

Figure 3.1.: Basic principle of an STM: Ideally an atomically sharp tip is scanned over a surface in x–y–direction. Between the tip and sample a tunneling current I is flowing, when a bias voltage V is applied.

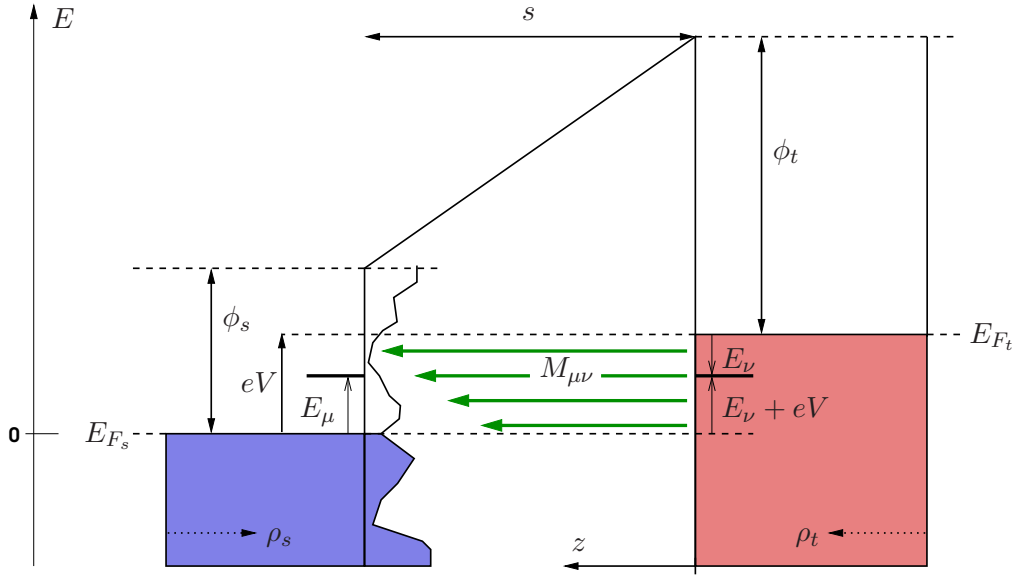

Figure 3.2.: Energy diagram of a tunnel junction in one dimension at $T = 0$, with z as the separation of the electrodes. The left electrode represents the sample (s) with its special features in the local density of states (LDOS) ρ_s, indicated in blue, and the right an ideal tip (t) with a constant LDOS ρ_t, indicated in red. With a positive voltage V applied to the sample a net tunneling current can flow from occupied states of the tip into unoccupied states of the sample. The tunneling probability between two states (E_ν, E_μ) is determined by the tunneling matrix elements $(M_{\mu\nu})$. The Fermi energies are indicated by $E_{F_{s,t}}$, the individual work functions of the electrodes are $\Phi_{s,t}$. If one is defining an effective work function $\Phi_{eff} = (\Phi_s + \Phi_t - eV)/2$, mainly states nearby the Fermi level of the electrode with higher energy are involved, where Φ_{eff} is smallest.

Here the energies are given with respect to the Fermi energy. The total current is given by the sum over all possible states for an approximation with independent electrodes. For example electrons from occupied states of the tip (with $f_t(E_\nu)$ and index ν) can tunnel into unoccupied states of the sample (with $[1 - f_s(E_\mu)]$ and indexed by μ). Taking a current into both directions into account the net tunneling current is:

$$\begin{aligned} I &= \frac{4\pi e}{\hbar} \sum_{\mu\nu} \{f(E_\nu)\,[1 - f(E_\mu)] - f(E_\mu)\,[1 - f(E_\nu)]\} \\ &\qquad \cdot |M_{\mu\nu}|^2 \cdot \delta(E_\mu - (E_\nu + eV)) \qquad (3.5) \\ &= \frac{4\pi e}{\hbar} \sum_{\mu\nu} [f(E_\nu) - f(E_\mu)] \cdot |M_{\mu\nu}|^2 \cdot \delta(E_\mu - E_\nu - eV). \qquad (3.6) \end{aligned}$$

The energies E_μ, E_ν are given with respect to the Fermi energies E_{F_s}, E_{F_t} respectively, which is shown in Fig. 3.2 by the marked arrows. This case describes elastic tunneling without any scattering and energy losses. Both states involved have the same energy, denoted by the δ-function.[2] $M_{\mu\nu}$ are the tunneling matrix elements. They connect the wave functions (Ψ^s_μ and Ψ^t_ν) of the electrons of both electrodes and describe the tunneling probability between states μ and ν.

The tunneling current is determined by summing over all possible states. Instead of considering the states itself, it is beneficial to consider the *density of states* (DOS) $\rho(E)$ at an energy E. With this concept and changing the summation into an integration (for a sufficiently large number of states involved) the tunneling equation (Eq. 3.6) becomes

$$I = \frac{4\pi e}{\hbar} \int_{-\infty}^{+\infty} d\epsilon\, [f_t(\epsilon - eV) - f_s(\epsilon)] \cdot \rho_t(\epsilon - eV)\rho_s(\epsilon) \cdot |M(\epsilon, \epsilon - eV)|^2. \qquad (3.7)$$

The energies are given with respect to the Fermi energy of the electrodes.

Bardeen [1] formulated a way to describe the tunneling matrix elements from a many particle point of view by perturbation theory. Its modified approximation leads to

$$M_{\mu\nu} = -\frac{\hbar^2}{2m} \int d\mathbf{S} \left(\Psi^*_\nu \nabla \Psi_\mu - \Psi^*_\mu \nabla \Psi_\nu \right). \qquad (3.8)$$

The integration takes place over a surface $\mathbf{S}$ in between the electrodes within the barrier. The dimension of the element is energy. It is justifiable to assume the matrix elements to be nearly constant in the regime of small bias voltage ($eV \ll \Phi$ and $eV \ll E_F$). Physically the matrix element corresponds to the energy lowering caused by the overlap of the wave functions.

The most difficult task is to determine the matrix elements without knowing exactly the properties of the tip and the sample, since they depend on the exact positions of the atoms in space and the respective wave functions are energy dependent. Ideally the DOS of the tip would be constant, since one is only interested

[2] Mathematically the δ-function is not absolutely correct in the sum, but it is often used for a better understanding.

to image the sample properties with the STM. It would be appreciable to know exactly the shape of the tip and its electronic structure, but in practice only some assumption about the tip can be made, which is generally sufficient to understand the basic properties of the tunneling system.

Tersoff and Hamann [16, 17, 5] found such a method to describe the tunneling between a surface and a model tip. They used a spherical s-wave like tip, shown in Fig. 3.3.

The tip wave functions are approximated by a spherical harmonic expansion with the tip apex atom as the origin $\vec{r}_0$, shown in Fig. 3.3. In this case the matrix elements can be simplified to

$$M = -\frac{2\pi C\hbar^2}{\kappa m_e}\Psi_\mu(\vec{r}_0) \tag{3.9}$$

in which C is a constant referring to the coefficient for the tip state [7] and Ψ_μ are the wave functions of the sample at the position of the tip. In comparison with Eq. 3.1 again the exponential dependence on the tip-sample separation s is given by $|\Psi(\vec{r}_0)|^2 \propto e^{-2\kappa(R+s)}$.

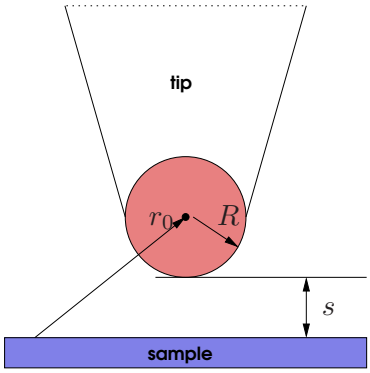

Figure 3.3.: Schematic view for the considerations in the Tersoff-Hamann model. In an s-wave like tip only the spherical like apex with radius R and origin r_0 is considered.

The *local density of states* (LDOS) of the sample at the position $\vec{r}$ is

$$\rho(\vec{r}, E) \equiv \lim_{\epsilon\to 0}\frac{1}{\epsilon}\sum_{E_\mu=E}^{E+\epsilon}|\Psi_\mu(\vec{r})|^2 = \sum_\mu |\Psi_\mu(\vec{r})|^2\,\delta(E_\mu - E), \tag{3.10}$$

which is the density of states per energy interval at the position $\vec{r}$.

Entering this new form for the matrix element (Eq. 3.9 into Eq. 3.7) it can be rewritten to a much simpler expression for the case of low temperatures and $|V| \ll \frac{\Phi}{e}$. At very small temperatures $T \to 0$ the Fermi-Dirac distribution $f(E)$ becomes a step function and therefore the integral changes into the following:

$$I = \frac{16\pi^3 C^2\hbar^3 e}{\kappa^2 m_e^2}\rho_t \int_0^{eV}\rho_s(\vec{r_0}, \epsilon)d\epsilon. \tag{3.11}$$

Chen [7] refined this theory by calculating models for p- and d-states of the tip.

3.1.1. Topographic imaging

In the last section the basic mechanisms of tunneling with respect to the STM were recovered. Since the tunneling current is exponentially dependent on the distance between tip and sample, it can be used as a measure of the sample height and therefore the topography. The distance between tip and sample is very small (only a few Å), such that an imaging of the topography by keeping a constant height

between the tip and sample and measuring the tunneling current is normally not very practicable due to the danger of tip crashes at higher steps. Generally, the constant current method is the standard method for STM usage. In this case the tunneling current I as the feedback parameter is kept constant and a regulator loop (described technically in Chap. 5) adjusts the tip-sample distance. The distance changes correspond to the changes of the surface, which is scanned.

Normally in an imaging device the original object is converted into an image, which can be described by a convolution function. For the STM the situation is somewhat different, since there are overlapping electron wave functions involved. There is no sharp spacial distinction in the sense of structural boundaries possible and the description as a simple transformation fails. Only if the length scale of imaging is larger than the interaction length scales of the probing particles the imaging of real pictures is valid.

For the STM it is justiciable to say that on length scales larger than about 1 nm the image corresponds to realistic topographical images, since here normally the properties of the electronic structure play only a minor role. For example the step heights (on metallic surfaces) are such features which are normally of topographical nature and can be interpreted as "real" image.[3] Of course for the resolution on this scale the aspect ratio of the tip, its real shape and the roughness of the sample still play a crucial role. Therefore the image can be interpreted as a geometrical convolution of the tip shape and sample surface (Fig. 3.4). An example are deep and small valleys, of which the width would always appear a little bit too small, since the tip is not infinitely sharp and electrons could also tunnel from the side of the tip.

For the sub-nanometer scale a different approach is necessary. In the last part already the basic assumptions and calculations were shown. For a constant current I the tip follows a surface of constant LDOS. The tunnel current depends on the sample LDOS at the tip position integrated over an energy window $E_F \leq E \leq E_F + eV$, if the DOS of the tip is assumed to be sufficiently constant (compare Eq. 3.11). Either occupied states ($V < 0$) or unoccupied states ($V > 0$) of the sample are detected (see also Fig. 3.2).

[3] This is e.g. not the case for insulating islands in metallic surfaces.

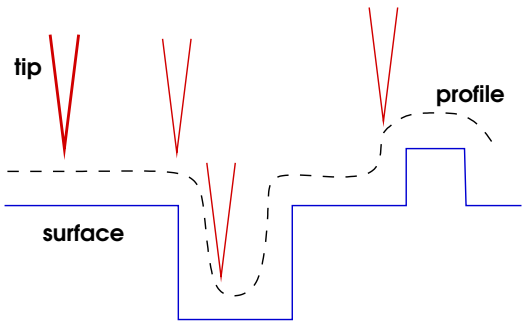

Figure 3.4.: Schematic view for the height profile (dashed line) as a convolution of the tip shape and sample surface structures.

Now, one could take images at different voltages to observe different spacial features of the electronic structure of the sample. This was done for instance on GaAs(110) [14], but it is not always as easy as in this example, where the valence states and conduction states appear quite distinct from each other. Another method would be the tunneling spectroscopy, which is described next.

3.2. Spectroscopy

Scanning tunneling spectroscopy is a very powerful tool used with the STM. There are several methods to do spectroscopic measurements (the fixed separation or variable separation $I(V)$ modes or a constant resistance mode [18]), but mainly the determination of the current-voltage characteristics at a constant tip-sample separation is performed. With this technique special features in the LDOS can be determined. The spectroscopy data is taken by stopping the scanning and holding the tip at a constant height above a point of the sample, while the feedback loop is switched off. In order to measure the tunnel current as a function of the sample bias $I(V)$, the bias voltage is then changed (see also Chap. 5).

In Eq. 3.7 an expression for the tunneling current I is given. For a sufficiently small sample bias ($eV \ll \Phi_t, \Phi_s$) the matrix elements M can be approximated as being constant. The tunnel current I can then be expressed by the simplified expression

$$I \propto \int_{-\infty}^{\infty} d\epsilon\, \rho_s(\epsilon)\rho_t(\epsilon - eV)\left(f_t(\epsilon - eV) - f_s(\epsilon)\right). \tag{3.12}$$

Its derivative is

$$\begin{aligned}\left.\frac{\partial I}{\partial V}\right|_{V_0} \propto \int_{-\infty}^{\infty} d\epsilon \quad & \left[-\rho_s(\epsilon)\rho_t'(\epsilon - eV_0)f_t(\epsilon - eV_0)\right. \\ & -\rho_s(\epsilon)\rho_t(\epsilon - eV_0)f_t'(\epsilon - eV_0) \\ & \left.+\,\rho_s(\epsilon)\rho_t'(\epsilon - eV_0)f_s(\epsilon)\right]\end{aligned} \tag{3.13}$$

with the partial derivative of the DOS

$$\rho' = \frac{\partial \rho}{\partial \epsilon} \tag{3.14}$$

and the derivative $f'(\epsilon)$ of the Fermi-Dirac distribution function. (Here, for a reversed bias the indices for the tip and sample could be exchanged, since the tunneling equation is symmetric.)

It is now assumed that $\rho_t' \equiv 0$ corresponding to a constant DOS of the tip, then only the second term in Eq. 3.13 remains. For $T \to 0$, the Fermi-Dirac distribution becomes a step function $f(\epsilon)|_{k_BT\to 0} = \Theta(\epsilon)$ and its derivative is a $\delta-$function, therefore

$$\left.\frac{\partial I}{\partial V}\right|_{V_0} \propto \rho_t \int_{0}^{eV} d\epsilon\, \rho_s(\epsilon)\delta(\epsilon - eV_0) = \rho_t \cdot \rho_s(eV_0). \tag{3.15}$$

This equation shows that within the made assumptions $\partial I/\partial V$ is proportional to the DOS of the tip and sample. Since ρ_t is supposed to be constant for these considerations, changes in $\partial I/\partial V$ at a given V_0 correspond to changes in the DOS of the sample for the corresponding energy.

So far only the case of low temperatures was considered, which does not apply for the measurements taken within this work. The general idea remains valid for higher temperatures, that is, the proportionalities are not changed in principle. At higher temperatures the Fermi-Dirac distribution becomes less sharp and the transition from occupied to unoccupied states around E_F is much broader. From its derivative

$$f'(\epsilon) = \frac{\partial f}{\partial \epsilon} = \frac{-\exp(\epsilon/k_BT)}{k_BT\left[1+\exp(\epsilon/k_BT)\right]^2} = \frac{1}{2k_BT}\cdot\frac{1}{\cosh^2(\epsilon/2k_BT)}. \tag{3.16}$$

the energy broadening can be estimated for finite temperatures. The derivative $\partial f/\partial\epsilon$ is a peak function. To estimate the temperature related broadening of the line width of spectroscopic features, a sample with an infinitely sharp $\delta-$peak like feature in the DOS $\rho_s = A\delta(\epsilon-\epsilon_0)$ is considered [15]. With Eq. 3.13 (again for a constant DOS of the tip)

$$\left.\frac{\partial I}{\partial V}\right|_{V_0} \propto \int_{-\infty}^{\infty} d\epsilon\ \delta(\epsilon-\epsilon_0)\, f_t'(\epsilon - eV_0) \tag{3.17}$$

the energy broadening by the convolution of ρ_s with $f'(\epsilon)$ of Eq. 3.16 leads to:

$$\left.\frac{\partial I}{\partial V}\right|_{V_0} \propto\ \rho_t\cdot\frac{1}{k_BT}\cdot\frac{1}{\left[\cosh\left(\frac{\epsilon_0-eV_0}{2k_BT}\right)\right]^2}. \tag{3.18}$$

The latter[4] is a peaked function with its maximum at $\epsilon_0 = eV_0$. The full width at half maximum (FWHM) can be determined by a Gaussian approximation to about FWHM $2\sigma \approx 3.2\,k_BT/e$, which is the minimum separation to resolve two such peaks. Therefore an energy resolution of about $\Delta E \approx 100\,\mathrm{meV}$ is possible for a temperature of 300 K.

[4] Remarkably, only the temperature of the tip enters in this simplified consideration. Generally (and also in the case of this work) both, tip and sample, have the same temperature and thermoelectric voltages [13, 12] between tip and sample can be excluded.

Bibliography

[1] J. Bardeen. *Phys. Rev. Lett.*, 6:57, 1961.

[2] G. Binning and H. Rohrer. Scanning tunneling microscopy – from birth to adolescence. *Rev. Mod. Phys.*, 59:615, 1987.

[3] G. Binning, H. Rohrer, Ch. Gerber, and E. Weibel. *Appl. Phys. Lett.*, 40:178, 1981.

[4] G. Binning, H. Rohrer, Ch. Gerber, and E. Weibel. *Phys. Rev. Lett.*, 49:57, 1982.

[5] S. Blügel. *Theorie der Rastertunnelmikroskopie*, volume 29. Ferienkurs der Festkörperphysik, Physik der Nanostrukturen, chapter A3. Institut für Festkörperforschung, Forschungszentrum Jülich, 1998.

[6] Dawn. A. Bonnell, editor. *Scanning Tunneling Microscopy and Spectroscopy.* VCH Publishers, Inc., 1993.

[7] C. J. Chen. *Phys. Rev. B*, 42:8841, 1990.

[8] C. Julian Chen. *Introduction to Scanning Tunneling Microscopy.* Oxford University Press, 1993.

[9] C. B. Duke. *Tunneling in solids.* Academic Press, Inc., 1969.

[10] H.-J. Güntherodt and R. Wiesendanger, editors. *Scanning Tunneling microscopy*, volume I-III of *Springer Series in Surface Science.* Springer-Verlag, 1992.

[11] H. B. Michaelson. *J. Appl. Phys.*, 48:4729, 1977.

[12] M. A. Schneider, M. Wenderoth, K. J. Engel, M. A. Rosentreter, A. J. Heinrich, and R. G. Ulbrich. *Appl. Phys. A.*, 66:S161, 1998.

[13] J. A. Støveng and P. Lipavský. *Phys. Rev. B*, 42:9214, 1990.

[14] J. Stroscio, R. Feenstra, and A. Fein. *Phys. Rev. Lett.*, 57:2579, 1986.

[15] Markus Ternes. *Scanning tunneling spectroscopy at the single atom scale.* PhD thesis, École Polytechnique Fédérale de Lausanne, 2006.

[16] J. Tersoff and D. R. Hamann. *Phys. Rev. Lett.*, 50:1998, 1983.

[17] J. Tersoff and D. R. Hamann. *Phys. Rev. B*, 31:805, 1985.

[18] L. E. C. van de Leemput and H. van Kempen. *Rep. Prog. Phys.*, 55:1165, 1992.

[19] E. L. Wolf. *Principles of electron tunneling spectroscopy.* Oxford University Press, 1985.

4. Sample preparation and characterization (the standard techniques)

In the following sections most practical issues important in the course of this work will be covered, while the STM and STS techniques will be discussed in the next chapter (Chap. 5). The samples investigated here were thin films of $La_{0.75}Ca_{0.25}MnO_3$, prepared by the metal organic aerosol deposition technique, which is rather new and not very widespread. It was introduced at the institute three years ago and the realization turned out to be straightforward. As a matter of routine the samples were characterized by standard techniques with respect to their structure, resistance and magnetization to classify them in a larger context. The latter is important for a comparison with other measurements on similar samples. Since the main issue in this work are the STS measurements, the following paragraphs are kept short and the techniques are recapitulated very briefly for the sake of completeness. The interested reader will find everything about these widespread techniques in the literature cited and the references therein.

4.1. Metal organic aerosol deposition

The so called ***m****etal organic* ***a****erosol* ***d****eposition* technique (MAD) [15, 16, 14] is similar to the metal organic chemical vapor deposition (MOCVD) [19], but differs in some important aspects. The MAD technique can be used to produce all kinds of oxidic thin films and was initially developed to grow high T_C superconductors [12].

The technical principle is based on spraying a solution of the metal organic precursors, which are being pyrolized to form the oxidic films to be deposited, onto a heated substrate.

The metal atoms are bound in appropriate chemical precursor compounds. These are metal-chelate complex compounds with a coordination bound between the metal atom and the next neighboring oxygen atom of the ligand (Fig. 4.2). One of the simplest compounds are the metal-acetylacetonates $[M^{n+}(C_5H_7O_2)^-_n]$ where M denotes the metal atom. They are mixed in the respective ratio in an organic solvent like in this case dimethylformamide (DMFA). The solutions reach the reaction zone right above the heated substrate as small droplets. The solvent is evaporated very fast and is pumped away. In the ideal case of optimum conditions the remaining precursor particles are sublimated in the hot zone above the heated substrate such that the deposition occurs out of the gas phase (as in MOCVD). A pyrolysis reaction takes place as in the following example for Cu:

$$Cu(C_5H_7O_2)_2 + 12\ O_2 \xrightarrow{T_0} CuO + 10\ CO_2 + 7\ H_2O.$$

The pneumatic nozzle (Fig. 4.1) is operated with a carrier gas like oxygen or (cleaned) compressed air under a pressure between 2 - 3 atm. It produces an aerosol by vortices at the end of a small capillary with small droplets of about 10 - 50 μm in diameter, while a gas flow rate of ≈10 l/min. can be reached. At the bottom of the chamber a pump stabilizes the aerosol flux and removes the exhaust. On account of aerodynamic reasons this works only under atmospheric or a little bit lower (down to ≈150 mbar) pressure, but not in vacuum. The flow rate is measured with laser light scattered by the droplets passing by which is detected by a photodiode. The substrate is mechanically clamped on a SiC heater (possible temperature range up to 1500°C) of which the temperature is measured via an optical fiber with a pyrometer.

The main advantage of this method is the flexibility of the compounds. There is no need of expensive targets with a fixed composition. It is also possible to deposit on large area substrates or probably even bands which could transported through the reaction zone. The deposition rates can be chosen from very fast (≈1 μm/min) down to a fraction of a nm per second. A disadvantage is the required test series in which the composition of the solutions has to be adjusted. Since there might be some amount of water bound in the complex compounds, the exact ratios are difficult to determine, since the precursors are weighed before mixing.[1]

[1] For the different preparation conditions, precursor solutions, etc. see the Appendix.

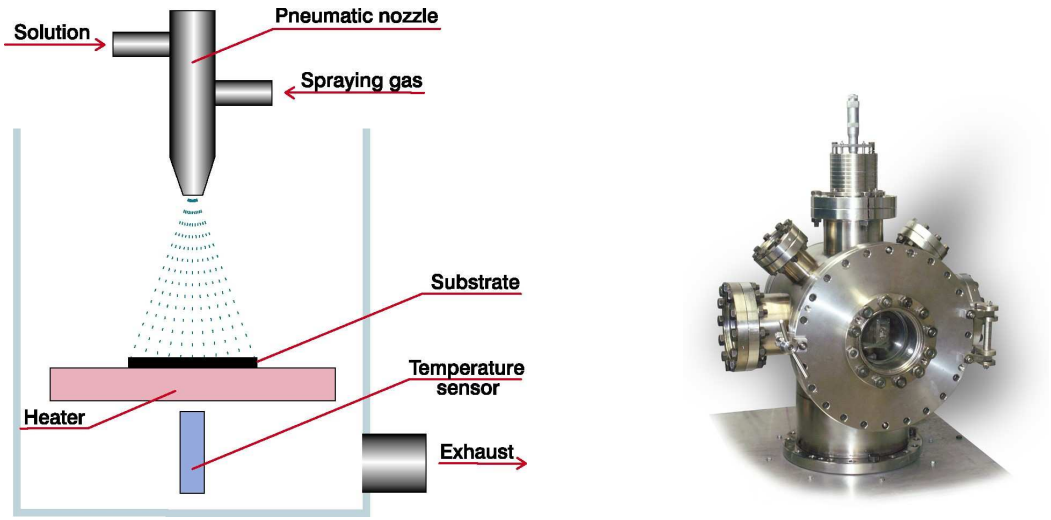

Figure 4.1.: Left: Schematic of the metal organic aerosol deposition. An organic solution with the respective metals dissolved in ionic form is sprayed as an aerosol onto the substrate. A carrier gas is stabilizing the flow and provides the oxygen. The evaporated solvents are pumped away as exhaust. The temperature of the substrate heater is measured by a pyrometer. Right: The MAD chamber.

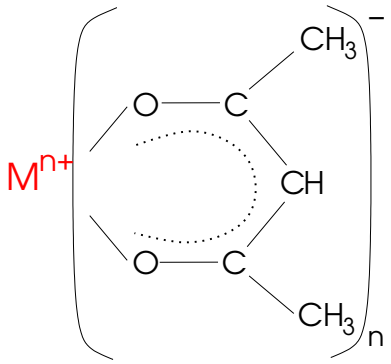

Figure 4.2.: General formula of the metal-acetylacetonate (ACEC) complex compounds in which the element is bound before deposition. M is the metal atom with charge n+ and has n ligands of the negatively charged (ACEC).

4.2. Standard characterization

4.2.1. X-Ray scattering

The structural properties of the LCMO films were determined by means of X-ray scattering [3]. The measurements were mainly performed in a two-axis Siemens D5000 diffractometer (and partially in a Bruker AXS D8 diffractometer) with Cu-K_α radiation. Two different X-ray techniques are employed here. The first one, ***X**-**r**ay **d**iffraction* (XRD), was used in the so called $\Theta/2\Theta$ geometry in which the angle of incidence is typically $\Theta > 10°$. (In the case of X-ray diffraction the angle of incidence Θ is always the angle between the lattice planes and the incident beam.) In the second one a grazing incidence with $0.5° \lesssim \Theta \lesssim 10°$ is used, a reflection and refraction method which is called ***X**-**r**ay **r**eflectometry* (XRR). In more general terms, very often it is distinguished between ***w**ide **a**ngle **X**-ray **s**cattering* (WAXS) and ***s**mall **a**ngle **X**-ray **s**cattering*[2] (SAXS).

Wide angle X-ray diffraction

To determine crystal structures and the corresponding lattice parameters, commonly wide angle XRD is used. The $\Theta/2\Theta$ geometry, the Bragg-Brentano geometry, is demonstrated in Fig. 4.3. The geometry of the X-ray source, sample and detector is maintained in such a way that always the angle of incidence is equal to the angle of reflection.

The momentum transfer defined by the scattering vector $\vec{q} = \vec{k}_i - \vec{k}_r$ between the incident and reflected beam vectors, always lies normal to the lattice planes. With this kind of measurement a pattern with maxima at the respective angles for the corresponding reflecting lattice planes – specified by the Miller indices – is obtained (for the intensity of the reflections and the diffraction/selection rules see the given literature (e.g. [7]) or the textbooks on solid state physics [11, 2]).

According to the respective space group symmetry the lattice parameters can be

[2] SAXS includes also special small angle diffraction techniques.

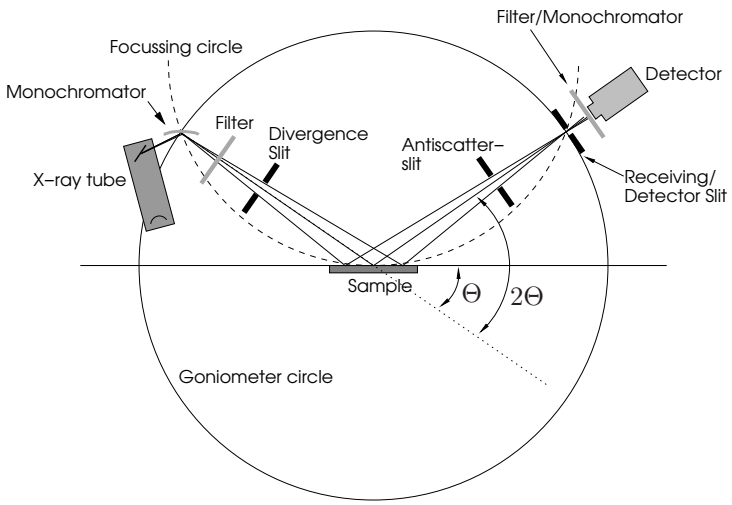

Figure 4.3.: Schematic diagram of an X-ray diffractometer in Bragg-Brentano ($\Theta/2\Theta$) geometry. The X-ray tube and the detector always reside on the intersections of the goniometer and focusing. With the divergence slit the area irradiated on the sample can be set, while with the antiscatter-slit unrequested stray radiation is gated out. Additional filters or monochromators can enhance the performance of the measurement.

calculated from the position $\Theta_{(hkl)}$ of the peaks in the pattern. As an the example for a simple cubic lattice with its Miller indices h, k, l, unit cell parameter a and for a wavelength λ the following relation holds valid:

$$d_{hkl} = \frac{a}{\sqrt{h^2 + k^2 + l^2}} \quad \text{with} \quad 2d_{hkl} \sin \Theta_{(hkl)} = \lambda \tag{4.1}$$

The technique utilizes the fact, that monochrome (and parallel[3]) X-rays are scattered from a crystalline structure according to this well known Bragg reflection [7].

Small angle X-ray reflectivity

Especially for thin films the techniques under grazing incidence have been developed, because then the scattering vector, $\vec{q}$, becomes much shorter and therefore more information of the films can be gathered. Measuring the reflectivity of X-rays has some similarities to optical refraction, with a difference in wavelength and the appropriate indices of refraction. The X-rays are scattered at the interfaces of different materials, schematically shown in Fig. 4.4, and the real and imaginary part of the index of refraction can be determined, comparable to optical ellipsometry. XRR reveals information about the film thickness, surface roughnesses and electron density (which indirectly contains some chemical information).

The index of refraction for X-rays is

$$n = 1 - \delta - i\beta \quad \text{where} \quad \delta = r_e N_e \lambda^2 / 2\pi \quad \text{and} \quad \beta = \mu\lambda / 4\pi, \tag{4.2}$$

[3] Parallel beams are realized with special crystals or Göbel mirrors, which only some reflectometers use like the Bruker AXS D8.

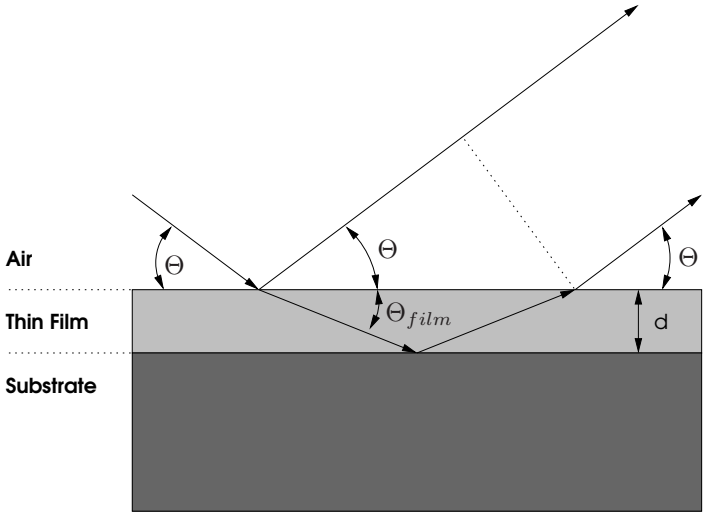

Figure 4.4.: The principle of XRR: Due to the different indices of refraction the beam is reflected at the interface. Depending on the angle of incidence, Θ, the phase changes and the intensity is altered corresponding to constructive or destructive interference.

with the dispersion δ related to N_e the electron density[4], $r_e = e^2/mc^2$ the classical electron radius and the absorption index β related to μ the attenuation coefficient [20, 23]. For the thin film/air interface a total reflection occurs at an angle Θ_t, since $n < 1$

$$\Theta_t \approx \sin\Theta_t = \sqrt{2\delta}. \tag{4.3}$$

With theses quantities the electron density and with known chemical composition the density of the material can be calculated. By varying the angle of incidence Θ on a single thin film like in Fig. 4.4 for instance, one obtains an array of interference maxima[5] m from which the film thickness d can be determined. The pattern behaves like

$$\sin^2\Theta_m = 2\delta + (m + \Delta m)^2\lambda^2/4d^2 \tag{4.4}$$

with Δm either being 0 or 1 if no phase shift occurs (in the case of reflection). There is no analytical solution for the intensity of the oscillations due to repeated reflections, but they can be simulated [9]. Here for the simulation a recursive formula from Parratt [17] is used within the program "Parratt32" [5]. It models the roughness and film thickness.

4.2.2. Resistance measurements

The resistance measurements were performed in a PPMS-9 System from Quantum Design [1]. The temperature control covers a range between 1.9 K and 400 K and

[4] Sometimes the mass density ρ is used and leads to a modified expression $\delta = \rho N_A \frac{\sum_i (Z_i f_i)}{\sum_i M_i} \frac{\lambda 2 r_e}{2\pi}$ with N_A the Avogadro number, Z_i the atomic number with a dispersion correction f_i and M_i the atomic weights.

[5] also known as "Kiessig-fringes" [10].

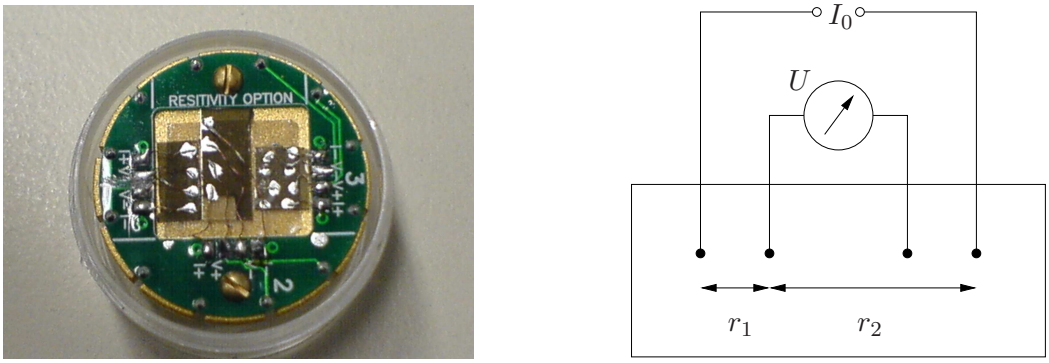

Figure 4.5.: Left: PPMS dc sample holder with three samples attached. Right: Principle of resistivity estimation for the four point probe technique (I_0: applied current, U: measured voltage).

magnetic fields up to 9 T can be reached. A dc resistance bridge for four-wire (or van der Pauw [21]) measurements of three samples simultaneously is available and provides a very comfortable and easy to handle resistance probe (Fig. 4.5). The standard four-point-probe geometry was used to eliminate the wire resistance from the measurement.

To contact the samples small drops with silver paste were used to connect them with copper wires to the sample holder. In the special geometry of four contacts in one line, the resistivity ρ can be estimated [22] in the following way according to Fig. 4.5:

$$\rho = \left| \frac{\pi}{\ln \frac{r_1}{r_2}} \right| \cdot d \cdot \frac{U}{I_0} \tag{4.5}$$

This formula is valid for point-like contacts (realized as tips) in one exact line. In this case of course it can only be used as an estimation, which is a little bit larger than the real resistivity, but it does not constitute a severe problem as long every measurement is analyzed the same way.

With the standard sample holder of the PPMS system the sample plane is placed perpendicular to the magnetic field.

4.2.3. Magnetization measurement

To determine the integral magnetic properties of the LCMO films, that is the magnetization, a SQUID-magnetometer MPMS-5s from Quantum Design was used [18]. The magnetometer is equipped with a superconducting solenoid for fields up to ± 50 kOe and a He gas flow cryostat which provides sample temperatures from 1.8 K to 400 K. The sample holder permits measurements in the sample plane as a function of temperature and magnetic field. In special cases also the resistance of the sample can be measured, or the sample can be turned in its plane to measure in-plane anisotropies.

A SQUID[6] (*superconducting* ***qu****antum* ***i****nterference* ***d****evice*) is one of the most

[6]Here the sensor itself is meant in contrast to the whole machine, the SQUID-magnetometer.

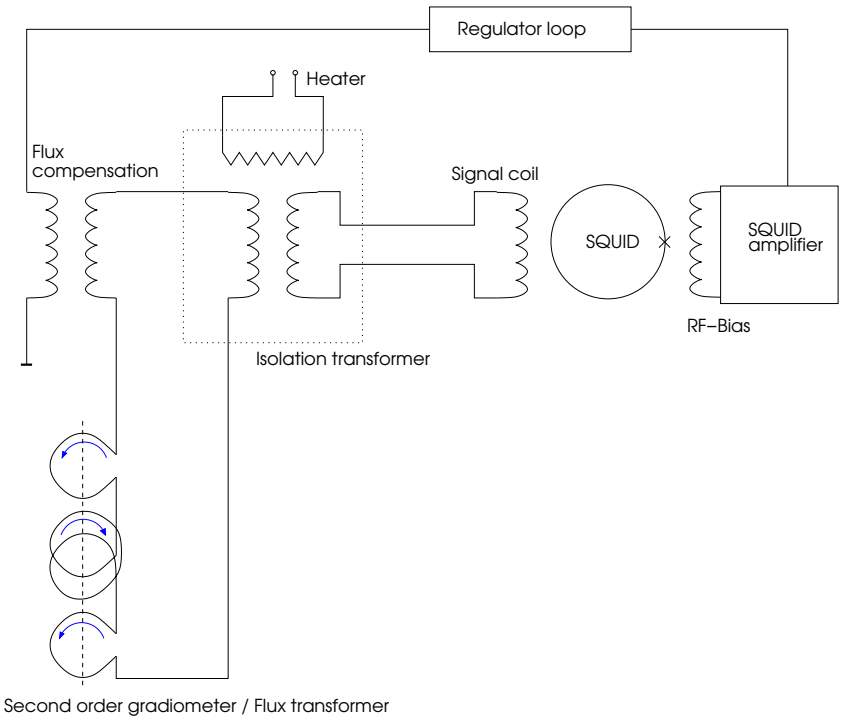

Figure 4.6.: Working principle of a rf-SQUID magnetometer with a second order gradiometer. The broken line indicates the sample movement within the detection coils, in which the dipole moment of the sample is measured. The isolation transformer provides a low-noise performance and the heater is needed to remove persistent currents in the superconducting coils. Via the signal coil the external flux is coupled into the SQUID. The flux compensation via the regulator loop permits to measure fluxes smaller than the flux quantum Φ_0.

sensitive devices to measure magnetic fields. It exploits the effect of flux quantization in a superconducting ring with one or two Josephson contacts [6, 8]. In the case of a rf-SQUID, discussed here, only one Josephson contact is used. The SQUID itself is coupled only inductively via a radio frequency oscillator. The total flux Φ enclosed in the ring is given by the periodic function

$$\Phi = \Phi_{ext} - LI_0 \sin 2\pi(\Phi/\Phi_0) \tag{4.6}$$

while the external flux Φ_{ext} is the sum of the flux to be measured (Φ_m) and the flux from the rf-circuit. The maximum superconducting current in the ring is I_0 and L is its self inductance.

For enhanced sensitivity the magnetometer uses a so called second order gradiometer [13], which describes the geometry of the detection coils in which the sample is moved for a measurement. In fact in this way the dipole moment of the sample is measured. With the help of a flux compensation via a regulator loop, fluxes even smaller than the flux quantum Φ_0 can be measured. If a lock-in technique is used, a sensitivity down to 10^{-7} emu can be reached. The SQUID operates as a flux-voltage converter, that is the flux is detected as small variations of the

voltage in the detection system (see also Fig. 4.6). With the help of a computer based measurement system, different measurements can be recorded automatically. For a more detailed description of the system see also [4].

Bibliography

[1] PPMS – Physical property measurement system. Technical Report Rev. 9.06, Quantum Design, 2006. www.qdusa.com.

[2] N. W. Ashcroft and N. D. Mermin. *Solid State Physics*. Saunders College Publishing, 1976.

[3] M. Birkholz. *Thin Film Analysis by X-Ray Scattering*. WILEY-VCH Verlag GmbH & Co. KGaA, 2006.

[4] A. Bracchi. *Structural and Magnetic Properties of the Glass-Forming Alloy* $Nd_{60}Fe_{30}Al_{10}$. PhD thesis, University of Göttingen, 2004.

[5] Christian Braun. Parratt32 - or the reflectivity tool. HMI Berlin, 1997-2002.

[6] W. Buckel. *Supraleitung - Grundlagen und Anwendungen*. Physik Verlag.

[7] B. D. Cullity. *Elements of X-ray Diffraction*. Addison-Wesley, USA, 1987.

[8] E. du Trémolet de Lacheisserie, D. Gignoux, and M. Schlenker, editors. *Magnetism, II - Materials and Applications*. Kluwer Academic Publishers, 2002.

[9] V. Holý, U. Pietsch, and T. Baumbach. *High-resolution X-ray scattering: from thin films and multilayers*. Springer tracts in modern physics. Springer Verlag, 1999.

[10] H. Kiessig. *Ann. d. Phys.*, 10:769, 1931.

[11] C. Kittel. *Einführung in die Festkörperphysik*. Oldenbourg Verlag GmbH, München, 1980.

[12] I. V. Koroshun, E. V. Kryaev, V. T. Moshnyaga, G. A. Klosse, M. A. Krachun, V. M. Zakosarenko, and V. Yu. Davydov. *Supercond. Sci. Technol.*, 3:493, 1990.

[13] Mike McElfresh. Fundamentals of magnetism and magnetic measurements: Featuring quantum design's magnetic property measurement system. Technical report, Purdue University, 1994.

[14] V. Moshnyaga. Metalorganic aerosol deposition technique. Personal communication.

[15] V. Moshnyaga, I. Khoroshun, A. Sidorenko, P. Petrenko, A. Weidinger, M. Zeitler, B. Rauschenbach, R. Tidecks, and K. Samwer. *Appl. Phys. Lett.*, 74:2842, 1999.

[16] V. Moshnyaga, I. V. Koroshun, and E. V. Karyaev. Preparation of oxide thin films from coordination compounds. Unpublished.

[17] L. G. Parratt. *Phys. Rev.*, 2:359, 1954.

[18] Quantum Design. *MPMS XL Hardware Reference Manual*, 1996.

[19] D. L. Schulz and T. J. Marks. *Advanced Materials*, 6:719, 1994.

[20] A. Segemüller. *Thin Solid Films*, 18:287, 1973.

[21] L. J. van der Pauw. *Philips Technical Report*, 26:220, 1958.

[22] R. von Helmolt. *Magnetowiderstandseffekte in heterogenen Legierungen und magnetischen Oxiden*. Doktorarbeit, Universität Augsburg, 1995.

[23] G. Zorn. The new Siemens X-ray reflectometer. Analytical Application Notes Ausg. 1, SIEMENS AG, Jan. 1994.

5. Scanning tunneling microscopy and spectroscopy – Setup and experiments

Although STM is a very widespread and commonly used technique, coping with its details is still a demanding task. An overall stability of the mechanical and electronic units below the nm-scale needs to be realized to compass the usage of all its capabilities. In this chapter some of the practical concepts of an STM will be presented as well as their realization in the present work. A detailed depiction of the *Cryogenic SFM - System* from Omicron Nanotechnologies – setup within this work – is then given, including the required changes and improvements.

The LCMO films were investigated by STM to determine the topography and, as a main part, by STS. The latter was used in order to analyze the electronic structure at the Fermi edge by means of measuring the local tunneling conductivity. STS measurements on $La_{0.75}Ca_{0.25}MnO_3$ thin films with respect to different temperatures have been already performed in earlier work [7, 8] using a different microscope. Here, the experiments are extended to measurements in magnetic fields at temperatures in the vicinity of the metal-insulator transition. STS measurements within magnetic fields in a variable temperature environment are still not a standard task. The combination of different requirements like a mechanically stable system, but at the same time a good thermal connection, combined with magnetic fields have to be established. Not many groups around the world have presented data measured under similar conditions on such systems.

The theoretical aspects of STM and STS were discussed in Chap. 3. Here the different realizations will be shown briefly and the most important technical requirements to be met will be presented. The discussion will be limited to the capabilities of the equipment used here, the reader will find more details in the literature [10, 9].

5.1. General considerations about STM/STS measurements

5.1.1. Measuring modes

In the STM a conducting (semiconducting) surface is scanned (in $x-y$ direction) with a metallic tip while several quantities to be measured are detected (Fig. 3.1), that is the current I, voltage U and height z (as the change of piezo voltage). It happens simultaneously (for example $z(x,y)$ with $I = const$) or at certain topography points like in the STS mode ($I(U)$ is measured at $(x,y) = const$). To describe the system different units have to be considered: a coarse positioning unit, a scanner unit together with the detection and feedback unit. The coarse positioning will

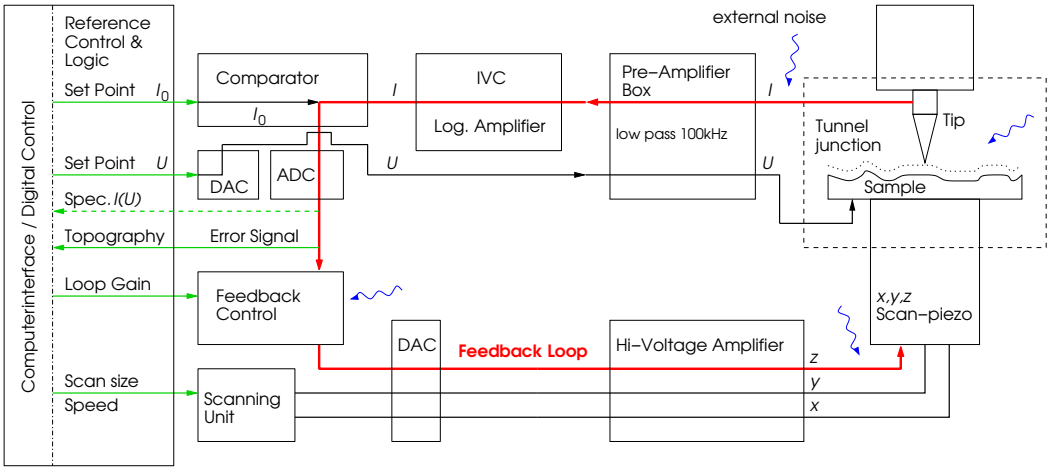

Figure 5.1.: Schematic diagram of the feedback system for the constant current mode. The feedback loop is marked in red: The tunneling current I is measured, amplified and then compared as a converted voltage with the reference signal given by the user via a computer digital control system. The error signal, that is the difference to the reference, converted into a respective voltage is used to drive the z-piezo, which is adjusted to regain the reference value of the current. At the same time the error signal corresponds to the changes in topography (or more precisely constant electron density) and is recorded by the computer as the z-signal reproducing the topographic features. Also the voltage U is set via the control unit and it transverses a low pass filter. In case of the spectroscopy measurements the comparator and feedback control are switched off. The parts responsive to external noise are marked with blue arrows. (IVC: current/voltage converter, VIC: voltage/current converter, ADC: analog/digital converter, DAC: digital/analog converter)

be described together with the microscope itself (Sec. 5.2).

The sample movement is accomplished by a piezo drive while piezoelectric coefficients down to 0.2 nm/V can be easily established [1]. One of the important fields is the electronics responsible for the feedback loop and especially the sample and hold circuits, which are used, if the STS measurements are implemented in a topography measurement.

The most commonly used measuring mode of an STM is the *constant current mode*, in which the current is kept constant ($I = const$) and the topography is measured as the height changes of the piezo, $z(x, y)$. It provides the possibility to look at not well known surfaces without too much danger to damage the tip (or surface). The *constant height mode* ($z = const$) which measures $I(x, y)$ for example requires some prerequisites like a quite smooth surface and therefore small scanning areas to prevent the tip running into any obstacles, but might be advantageous for atomic resolution pictures.

In this case only the constant current mode was used and its working principle is drawn in Fig. 5.1. A fixed bias is applied to the sample and the tip is approached until a pre-defined tunneling current is achieved (the tip-sample distance is hereby typically ≈ 0.1 nm). To maintain the current during scanning it is constantly

[1] It is easy to find construction guidances for very simple (home-built) STMs in air.

measured and compared with the reference value I_0 and the error (difference) signal is used to adjust the voltage applied to the z-piezo. This is done by the main feedback loop. Since the tunneling current is very small (in the range of nA), it has to be amplified. The first amplification step is realized in the ideal case as close as possible to the tunneling junction such that it becomes less interference-prone and then it is further amplified in a second step. Due to the non-linear response normally a logarithmic amplifier is used. For comparison and regulation the current is converted to a voltage. Analogue implementations have generally a smaller signal to noise ratio and therefore are used in combinations of a digital control unit [16].

For the spectroscopic techniques the scanning has to be stopped at certain points (generally in a form of a grid) by a sample and hold circuit. Depending on the spectroscopy technique the feedback loop has to be opened like in the case of $I(U)$ spectroscopy at constant height. The tip is stopped scanning and held at the feedback value, then the loop is opened such that the tip-sample distance is not changed while the spectroscopy curve is recorded. Before data acquisition can be started it is advisable to wait until any transient effects are worn off. It is very important that the tip-sample distance is not changing during the acquisition period. For example drift effects where the tip-sample distance is varying slightly would show up in terms of a modified slope of the curve.

5.1.2. Mechanical damping and electrical noise

The design of an STM governs its performance, whereat two sources of noise can be distinguished:

1. Mechanical noise, which affects the tip sample distance and therefore the measurement accuracy.

2. Electrical noise, originating from the amplifiers, cables and electronics.

The stability and fastening has to be chosen deliberately, which becomes more advantageous the more features are involved as for example variable temperatures and magnetic fields or a UHV system where the damping behaves totally different compared to atmospheric conditions. It is important to consider how much noise and vibrations can reach the STM and how the STM is responsive to these disturbances. In detail mechanical resonances which can be excited in the STM system have to be considered.

For a UHV-STM at least two mechanical systems have to be taken into account: the STM itself and the chamber(s) surrounding it. A simple model is a system for two coupled oscillators [21, 15],demonstrated in Fig. 5.2, with different masses (m_t, m_s for the tunneling and surrounding systems respectively) and spring constants (k_t, k_s) with the respective displacements (x_t, x_s).

The transfer function Z for such system is

$$Z = 20 \log \left[x_t - \frac{x_s}{x_t} \right] . \tag{5.1}$$

The vibration isolation of the external part acts as a low-pass filter, while the inner system with the microscope is a high pass filter. Now the cut-off frequencies should

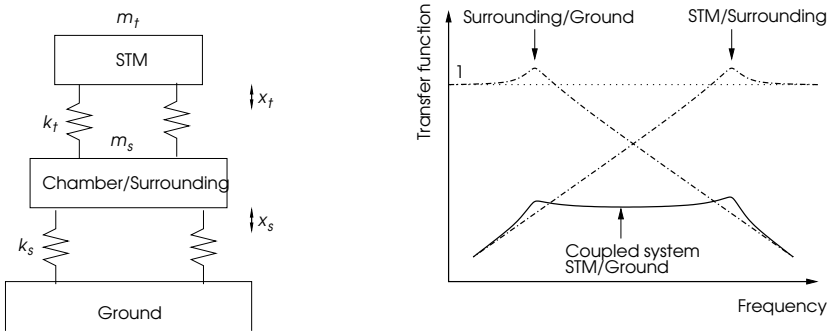

Figure 5.2.: Left: Vibrational system as a coupled oscillator of the STM and the surrounding chamber. Right: Schematic drawing of the transfer functions for the noise propagation.

be as far away as possible and the plateau in between (see Fig. 5.2) should be as low as possible.

Another contribution to noise in the tunnel current measurement comes from the coaxial cable used for the connection between tip and pre-amplifier. Coaxial cables represent capacitors which are not absolutely stiff on very small scales. Their parts can move against each other due to sound noise resulting in a change of capacitance C with time t. This induces small voltage changes dU and leads to small currents

$$I = C\frac{dU}{dt} + U\frac{dC}{dt} \tag{5.2}$$

These small disturbances are amplified together with the tunneling current and are one major source of noise. In general there are suitable amplifiers available which can be mounted directly into the UHV, but with the additional temperature changes it is nearly impossible to establish a stable working amplifier nearby the STM directly in the chamber. Therefore a low pass filter in the feedback system is indispensable.

5.2. The Cryogenic SFM by Omicron

The Cryogenic SFM (**s**canning **f**orce **m**icroscope) in Fig. 5.9 from Omicron is a system with a combined STM and AFM/MFM (**a**tomic/**m**agnetic **f**orce **m**icroscope) measuring head. The microscope is placed in a UHV chamber within a cryostat from Oxford Instruments. Sample temperatures in between 7 K and RT (300 K) and magnetic fields up to 8 T can be reached.

The system had to be set up for usage in this work. In microscopes of this type the connection of thermal stability with an undisturbed measuring system is, in general, a demanding task. In the following the system will be described in more detail split into the different parts. A lot of improvements were required with respect to the STM usage[2] and are described as well in the last part.

[2] The atomic force microscope was also assembled within this work, but not used for the main measurements; some MFM measurements are presented in the appendix.

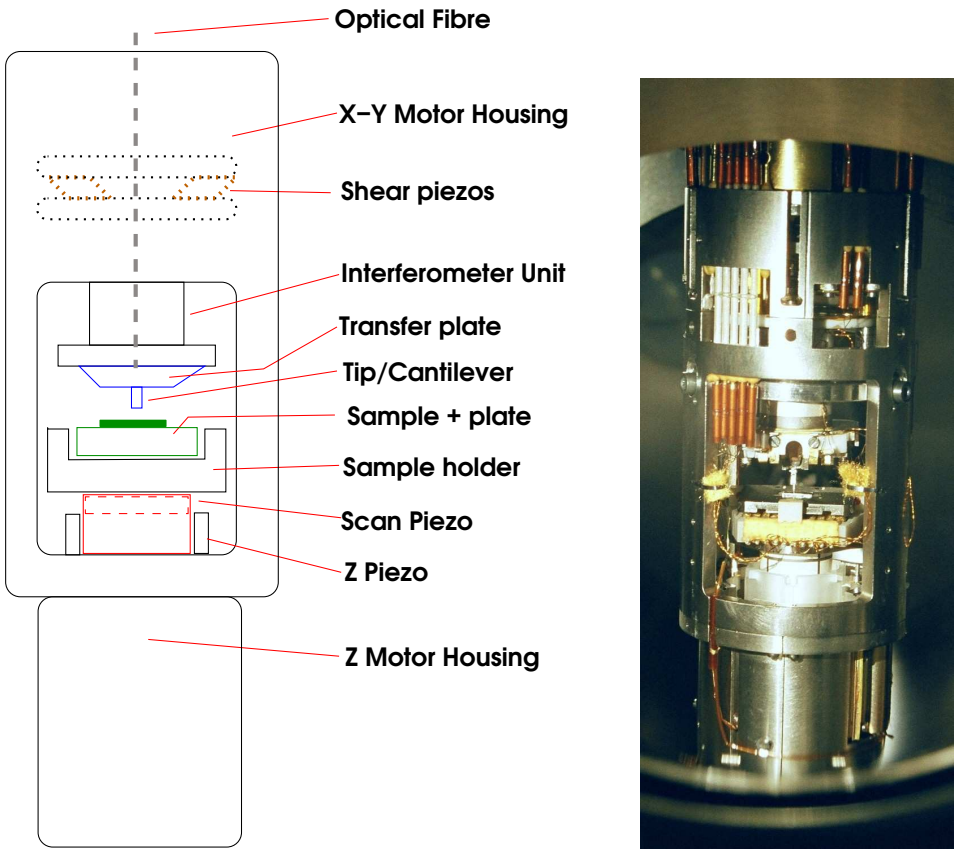

Figure 5.3.: Left: Drawing of the Omicron Cryogenic SFM microscope head in front view [16], which can be used for AFM as well as STM measurements. Here the sample is scanned and the tip/cantilever stays fixed. Right: Image of the installed head in the UHV system with a tip loaded (back view).

5.2.1. Inner system: The microscope and connected components

The microscope of the system is based on a combined STM/AFM measuring head (Fig. 5.3), which is optimized for MFM usage. Although atomic resolution on HOPG was reported for an STM measurement with the head suspended in air, the supplied system does not fulfill the specifications for atomic resolution, especially not under UHV conditions. It is built out of a scanner for both STM and AFM usage. In this case the sample holder is situated on the scanner piezo[3] (X-,Y-,Z-direction) and a coarse positioning piezo drive in Z-direction (perpendicular to the sample surface). The counterpart is the transfer (tip/cantilever) plate holder with a coarse positioning in X-Y-direction (the sample plane).

The coarse positioning is implemented by shear piezo stacks driven by a stick-slip mechanism [16, 4] demonstrated in Fig. 5.4. A saw tooth voltage is applied to the piezos in a way that the sample/tip is moved during the rising period (about 1 ms) of the voltage (sticking to moved parts) and it slips due to its inert mass during the fast ($\sim$ 2 μs) decay. The magnitude of the force F onto the slider system is

[3] Commonly the scanner is situated at the tip side due to its smaller inert mass.

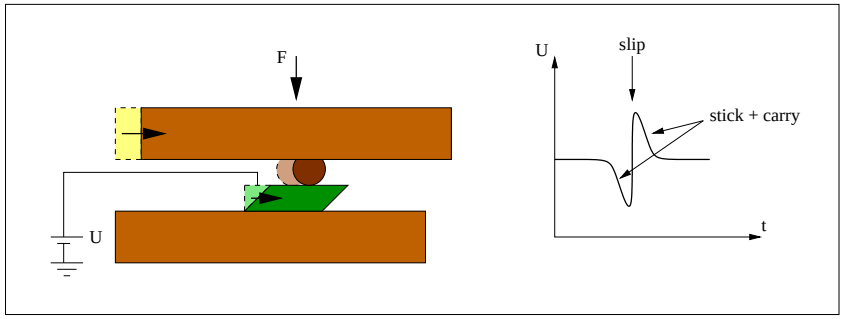

Figure 5.4.: Coarse positioning mechanism with shear piezo stacks. An asymmetrical saw tooth voltage is applied. The transport takes place during the rising parts of the voltage, where the stacks stick to the plates. When the voltage is changed fast, the plates slip over the stacks due to their inert mass (according to [4]).

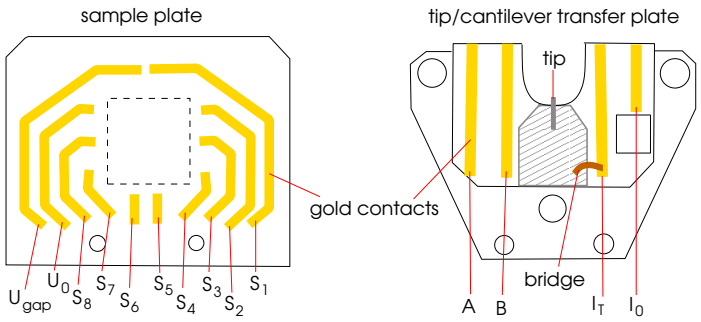

Figure 5.5.: Left: Drawing of ceramic sample plate with eight gold contacts (S_i). Right: Transfer plate, contacts A and B are free to use. Either a cantilever or a tip can be attached to the transfer plate [16].

important for a proper transport. The latter is a critical point of the system, since the clamping springs of the motor are often stressed a little bit during tip exchange.

Some sample holders give the opportunity to put eight contacts onto the sample (Fig. 5.5).[4] Normally the sample was glued and contacted with silver paste onto the sample holder.[5] The transfer plates on which either a AFM cantilever or a tip can be mounted, also have additional contacts and are attached directly to the interferometer unit. The support for the transfer plate is mounted on the piezo tube of the interferometer unit for the AFM function and has four springs under which the transfer plates are fixed. The temperature close to the sample is measured by a temperature sensor (cernox) with minimum magneto resistance.

The microscope itself is hanging at the end of a long rod, the baffle stick, inside the UHV system, see Fig. 5.6. It can be lifted with a crane to exchange tips and samples in the upper part of the UHV system and lowered into the cryostat for

[4] For normal usage there are titanium holders without gold contacts, which are easier to handle.
[5] Another self-built holder has titanium springs under which the sample can be fixed with two screws.

measurements. With copper wires for thermal coupling and allegedly mechanical damping the measuring head is fixed at the end of the rod [12]. All the cabling attached to the microscope is guided along the baffle stick and fixed at the radiation shields (baffles) in Fig. 5.6. The cabling is connected via UHV plugs at the top of the baffle stick where all feedthroughs are placed, including the preamplifier. The lower part of the baffle stick is made out of a good heat conducting, nonmagnetic material, while the upper part is of stainless steel. The UHV chamber for the microscope in the cryostat is coupled to a variable temperature insert (VTI), in which the UHV chamber is connected with a Helium space (annular pumping space) for cooling. When the baffle stick is led down it sits on a cone which provides the thermal coupling (Fig. 5.7). The VTI Helium space is connected to the He bath in the main cryostat via a thin capillary by a needle valve (NV). It is possible to pump at the end of the helium space such that the He flow is increased. To achieve low temperatures, it is necessary to pump liquid He into the helium space. It is also possible to achieve lower temperatures than 7 K by pumping the annular space continuously and lowering the temperature of the liquid He.

The microscope is only heated indirectly via the heater and needle valve at the cone. Therefore the temperature regulation of the system is very slow. For a comparison of the temperatures on the sample plate and at the sensor in the microscope an example for a test measurement is shown in Fig. 5.8, which was taken during the heating of the system from a temperature of about 200 K. It can be seen that the temperature sensor, which provides the temperature for the regulator, rises quite fast (the beginning of the heating is not shown), while the sensor in the microscope shows a much slower increase in temperature. Since the sample plate is only connected via the piezos and the small contacts and is otherwise surrounded by a cold environment, the temperature remains a little bit smaller (the difference does not exceed 5 K), than in the microscope. Fortunately it saturates within one or two days, and then stays at a constant temperature. The temperatures given in Chap. 7 are those measured at temperature sensor 3 in the microscope.

The microscope is operated using the omicron (AFM and STM) electronics and the omicron software Scala Pro. By the coarse positioning motors the tip is positioned above the sample. A movement of ~ 5 mm in X-Y-direction and ~ 10 mm in Z-direction is possible. The scanner sensitivities can be gathered from table 5.1. Since the piezo voltages are dependent on temperature T the calibration has to be calculated in the following way [16]:

$$\frac{\text{Piezo coefficient}\,(T)}{\text{Piezo coefficient}\,(293\,\text{K})} = 0.18 + 2.21\cdot 10^{-3}\,T - 1.63\cdot 10^{-6}\,T^2 + 1.26\cdot 10^{-8}\,T^3 \quad (5.3)$$

Specifications	300 K	77 K	4.2 K
Maximum scan size	$(20\times 20)\ \mu\text{m}^2$	$(8.7\times 8.7)\ \mu\text{m}^2$	$(3.6\times 3.6)\ \mu\text{m}^2$
Piezo sensitivities X and Y	24 nm/V	20.5 nm/V	4.3 nm/V
Piezo sensitivity Z	12 nm/V	5.2 nm/V	2.1 nm/V

Table 5.1.: Scanner piezo data for different temperatures (from [16]).

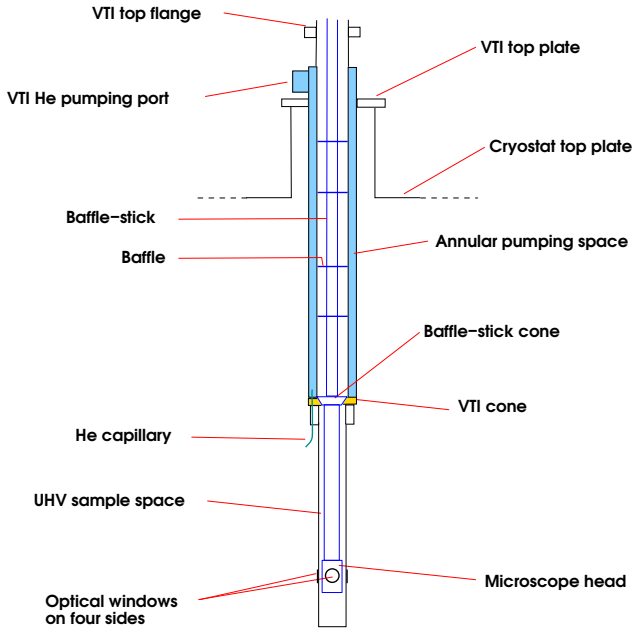

Figure 5.6.: The baffle-stick within the system, according to [17], lowered into the cryostat: The baffles touch the inner walls of the UHV chamber and are fixed by springs. Thermal connection is established via the cone.

5.2.2. Outer part: Cryostat, UHV system and environment

The cryostat attached to the system is from Oxford Instruments and shown in Fig. 5.10. It is constructed out of several dewars, of which already the annular He space in the VTI was described in the last part. The latter is situated in the middle of the cryostat in such a way that the microscope is placed directly in the homogeneous part of the magnetic field (marked by a cross in Fig. 5.10). Additionally it is shielded by a copper tube from the outside and the main He bath, which surrounds it, to minimize thermal radiation. A superconducting split coil magnet (NbTi) provides magnetic fields perpendicular to the sample surface up to 7 T for normal use. It is also equipped with a lambda point fridge [11, 6] to obtain a field of 8 T. For a better thermal insulation a liquid nitrogen bath encloses the He dewar in the upper half. In the lower half it is extended by a thermal shield down to the bottom of the cryostat[6] (blue line in Fig. 5.10). The nitrogen dewar and radiation shield are wrapped by a superinsulation and all dewars are separated by an insulation vacuum (outer vacuum shell, OVC). For further purposes the microscope can be optically accessed through four windows in the lower part of the cryostat (dashed line). The retention time for the liquid He is about two days (three days stand-by at moderate temperatures) depending on the magnetic fields and temperatures used.

The baffle stick with the microscope can be lifted within the vacuum chamber

[6] The reason for the latter construction which leaves some empty space is intended for the possibility of a second magnet with its field direction perpendicular to the other.

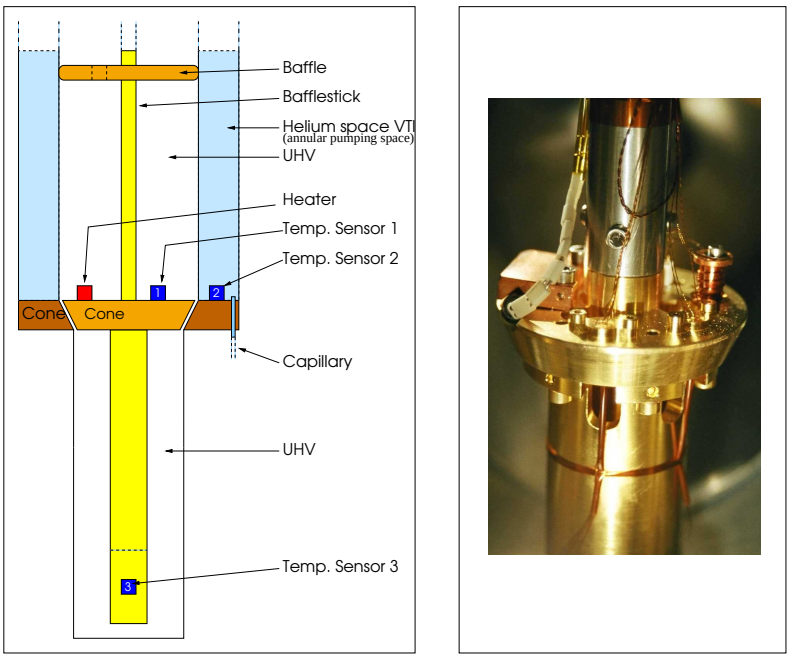

Figure 5.7.: Left: Schematic diagram of thermal connections (no true-to-scale representation). Thermal coupling takes place via the cone. The temperature is measured at three points (sensors 1-3) and regulated with the help of the needle valve, the heater and sensor 1. Right: Picture of the cone with the heater (left) and temperature sensor (right).

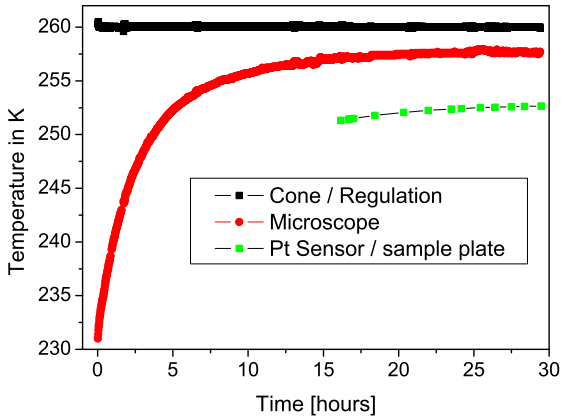

Figure 5.8.: Plot of temperature evolution at cone (where the temperature sensor 1 is situated for regulation), microscope (temperature sensor 3) and the samples plate (measured by a Pt resistor).

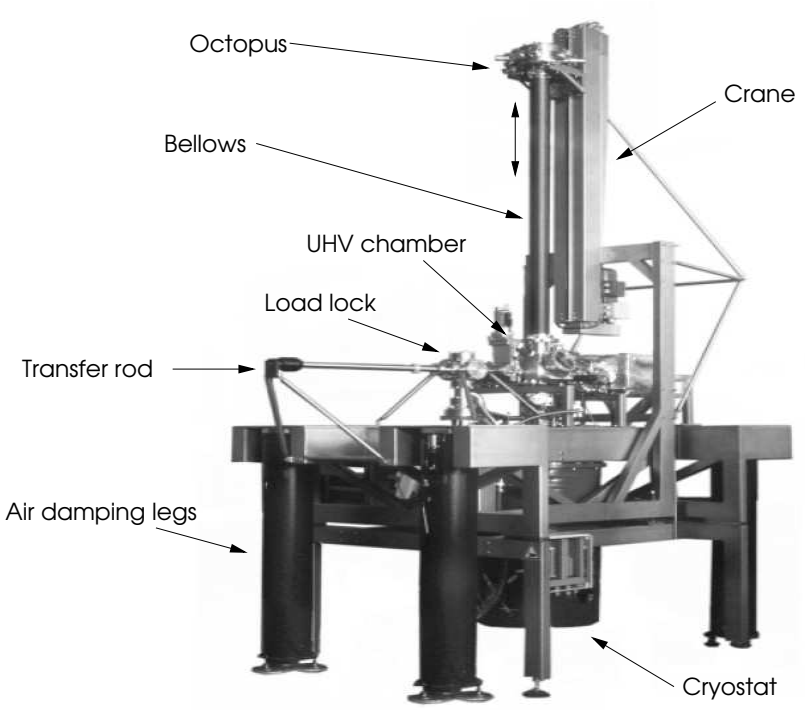

Figure 5.9.: The Omicron Cryogenic SFM System (modified according to [16]). There are two systems decoupled from each other: the crane and the UHV chamber - cryostat system. The latter is carried by the air damping legs during measurement. For tip and sample exchange the microscope can be lifted out of the cryostat within the UHV chamber. With the help of a load lock chamber tips and samples can be transferred into the UHV chamber without breaking the vacuum. The cabling for the microscope is supplied via the octopus, a small chamber with cable feedthroughs at the end of the microscope suspension.

above the cryostat without breaking the vacuum. There, the samples and tips can be transferred into the UHV chamber and the microscope using a wobble stick. It is possible to store four samples and tips in the chamber. A load lock chamber provides the possibility to exchange tips and samples without braking the vacuum.[7]

The UHV is mainly generated by an ion getter pump and a titanium sublimation pump (TSP)[23]. The load lock chamber is pumped by a turbo molecular pump. In both chambers the pressure is measured by ion gauges. A bake out tent belongs to the system and wraps the whole UHV chamber. The system can be heated up to 150 °C, larger temperatures would cause depolarization of the piezos. Also the UHV chamber in the cryostat can be baked. The bake out is controlled by several heating circuits and three temperature sensors in the cryostat, the UHV chamber and the bellows respectively.

The whole system stands on a special foundation in the laboratory decoupled from the rest of the building. An additional mechanical damping is given by four

[7] The samples were cleaned with isopropanol and put onto a heating plate at > 120°C at ambient pressure, before they were mounted in the load lock chamber to minimize any contaminations and the water film on the sample.

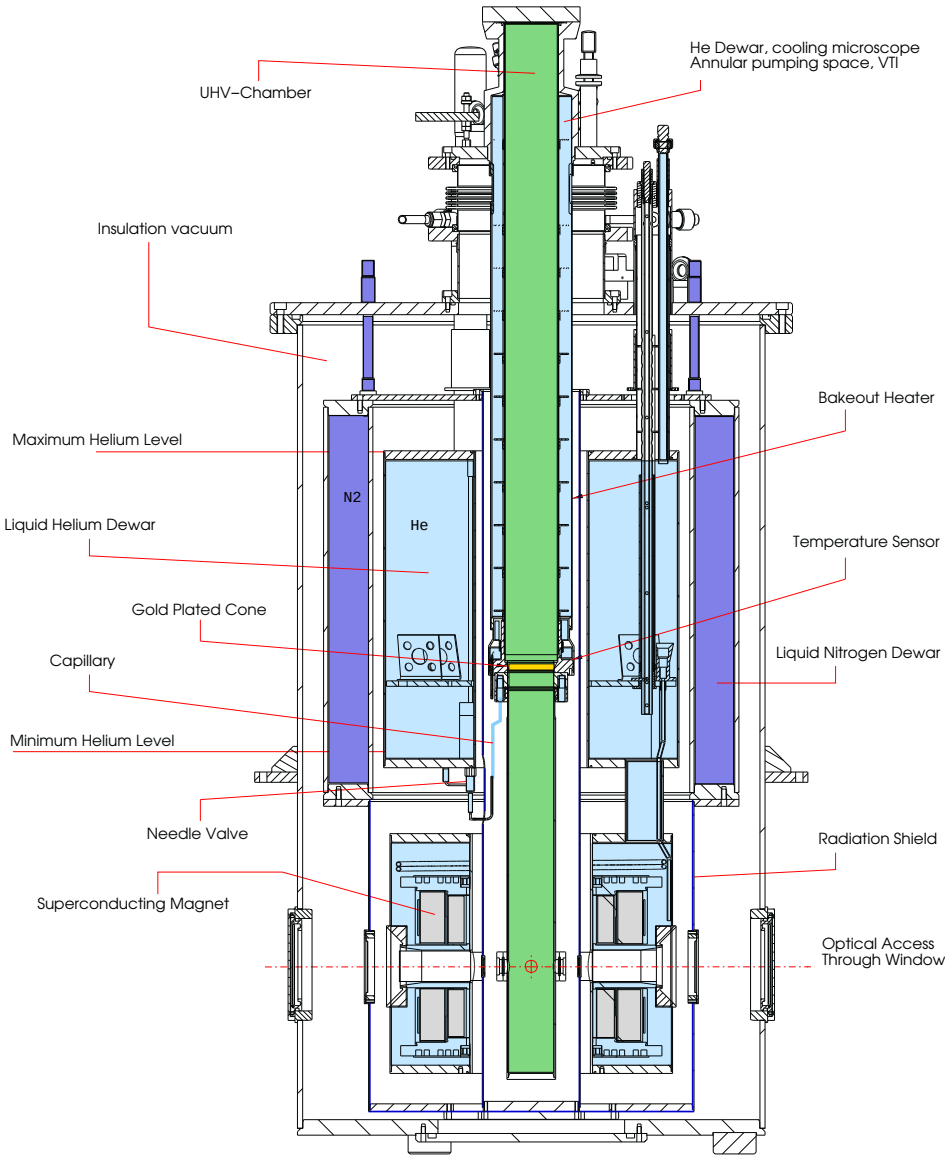

Figure 5.10.: The Omicron SFM Cryostat: In the middle the VTI (variable temperature insert) is situated with the UHV chamber in it (green), where the baffle stick with the microscope is placed. It is surrounded by the annular pumping space for cooling with He and coupled by the gold plated cone. During measurement the microscope is hanging in the position of the red cross in the middle of the superconducting magnet. The latter is situated in a liquid He bath dewar (light blue). A liquid nitrogen dewar (dark blue) with its radiation shield functions as an additional thermal insulation. The different parts of the system are isolated by an insulation vacuum (white).

damping legs which are operated by compressed air. These legs are coevally pendulums balancing lateral forces. They are carrying the complete UHV system and the cryostat and can only be used when the microscope and the baffle stick are in the measurement position. Then also the crane is mechanically decoupled from the system.

5.2.3. Operation, electronics and important improvements

This part describes the operational properties of the microscope, the control electronics and their intricatenesses. Using the setup as supplied by the manufacturer, it was hardly possible to achieve decent STM images and an adequate stability for the spectroscopy. Therefore substantial improvements had to be made such that the results were enhanced considerably (see also Fig. 5.11).

The microscope is operated by the Omicron (AFM and STM) electronics and the omicron software Scala Pro. Although a lot of the noise comes from the outside, external excitations can cause problems within the electronics and regulation. Generally the regulation contains two parts, namely an integral and proportional gain [20]. The proportional gain P reacts very fast on the time-dependent error signal $e(t)$ and multiplies a constant K_P

$$P = K_P\, e(t) \tag{5.4}$$

while the integral gain I integrates the error signal over a certain time τ and then multiplies a constant K_I

$$I = K_I \int_0^\tau e(t)dt. \tag{5.5}$$

In a well tuned regulator loop the interplay between both should lead to a fast settlement to the setpoint. The Omicron electronics works only with a combined loop gain, whereas the proportional and integral gain cannot be tuned by the user.

One major problem is the regulator loop by itself: It produces a self driven 2 kHz oscillation, which excites additionally a 5 kHz oscillation. In order to work against this problem some of the operational amplifiers within the regulator circuits were changed to somewhat slower ones, which exert a supplementary low pass effect.[8]

As a matter of principle, mechanical vibrations are always found in the tunneling system, altering the tip-sample distance and as mentioned in Chap. 5.1.2 also through a coaxial cable noise enters. High frequencies of more than several kHz are dispensable, since the regulator loop always exerts a low pass effect. Very low frequencies can be balanced, but disturb the z-regulation and therefore also have to be kept out of the system (see next Chapter). The 2 kHz oscillation and other excitations within that order of magnitude and above could be damped out by adding a low pass filter between the preamplifier and the measuring electronics. The filter cut-off frequency should be as low as possible, but is limited by the scanning speed.

[8] A crosstalk between the coarse positioning and the scanner has not been observed within the operational range in this case, so the idea of a voltage divider was abandoned, although some people working with the Omicron electronics reported about more electronic disturbances becoming important in case of atomic resolution [22].

For a better monitoring of the disturbances an oscilloscope was added. All the electronics is connected to the same circuits to prevent ground loops and a filter at the mains supply avoids electronic noise from the electricity network. The reader might wonder about not using a lock-in technique for the spectroscopy measurements. The coaxial cable and overall setup limits the frequency, which can be used and demands a certain integration time (up to seconds). Since the temperatures normally used during the measurements were lying not far below room temperature, drift effects had to be taken into account and it was impossible to integrate over longer time periods than in the microsecond range. It was much easier to proceed with the spectroscopy in the typical sample and hold method.

5.2.4. Mechanical insulation and damping of the system

Another part of the noise comes from the microscope itself, which has a low resonance frequency due to its architecture. Since it is not absolutely mechanically decoupled from the rest of the system it was necessary to keep the whole system as calm as possible. (A pen dropping down caused a spike in the tunneling current.) With a sound generator it was shown that especially frequencies in the audible range coupled into the tunneling system. Eminently the small coaxial cable carrying the tunneling current underlies the sound effect [10]. Another reason is the mechanical coupling at the cone of the VTI. Therefore the whole electronics and the measuring computer were put into the neighboring room and a sound insulation cabin was built around the system.

The cabin was installed by Hüppe [1] in an octagon around the foundation of the system. It has one door to access the system during the measurement periods. Since the cabin is built out of several single parts it can be moved away into a parking position in case of extensive work on the system. It has one fixed element used for the supply line and cable feedthroughs. According to sound propagation principles the cabling in the feedthroughs were mechanically insulated and none of the cables was allowed to touch the channel walls.

A noise reduction by more than 43 dB was measured within the cabin using white sound noise at the outside. With the additional laboratory door tip crashes due to any noise or other disturbances in the hall can be prevented. With the cabin it is also possible to run a rotary pump in the laboratory without causing too much disturbances during a measurement.

For tip changes the sample always has to be taken out of the microscope to prevent dirt falling onto the sample. The springs clamping the transfer plate holder onto the coarse positioning are very sensitive to lateral forces. As a result they become loose, which might also be the reason for further instabilities due to disturbances. These clamps had to be fixed twice during this work. Once in a while the springs holding the transfer plates might over bent a little bit during transferring plates with too long feet and had to be adjusted. This can be done when the system is open, but it is also possible with the wobble stick for trained hands.

In Fig. 5.11 the noise problems are demonstrated by examples of STS curves. From a more or less unstable behavior, the spectroscopy data (upper left in Fig. 5.11) improved to smooth curves (lower left in Fig. 5.11, none of the curves here is

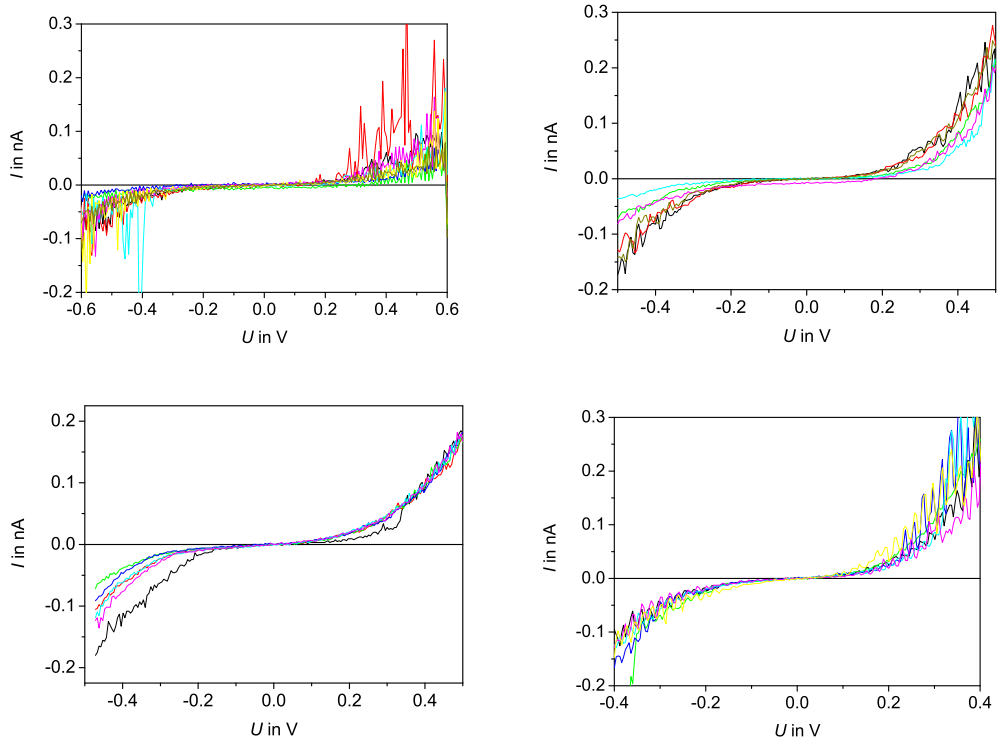

Figure 5.11.: Examples for noise improvements in spectroscopy (current I versus voltage U curves). Upper left: Before moving all control elements out of the room. Upper right: With the filter added and longer waiting times for the system to settle. Lower left: Additionally the nitrogen was pumped solid. Lower right: Example for incidental periodical vibration.

smoothed or filtered).

Another source of disturbance, not mentioned up to now, are the cryogenic liquids in the dewars of the cryostat. The liquid nitrogen boils giving rise to gas bubbles, hence it was pumped to a solid. The melting point is at 63.2 K, which is also the triple point at a pressure of about 129 mbar [5]. Since in contrast to water ice the volume of the solid nitrogen is decreased compared to the liquid [13], so that there is no danger to the dewar. The walls of the dewars seemed to be less excited to vibrations with an appropriate amount of liquid inside. At the outlet of the main He bath an extra reservoir filled with batting was added to prevent oscillations of He gas pressure.

Incidentally, it happened that a periodical vibration coupled in, like in the last curves of Fig. 5.11. It should be noted that the noise problems occur differently depending on the samples. If there is a very small height scale (less than 1 nm) the system is much more stable than on a sample with grains of several nm height, when the z-regulation is increased. In summary, due to a lot of changes the stability of the STM was conspicuously improved for spectroscopy measurements at higher temperatures and magnetic fields.

5.3. Computer based analysis

The main purpose of the spectroscopy measurements is to analyze the tunneling conductivity at 0 V that is the derivative dI/dU of the $I(U)$ curves. Particularly the spatial distribution of $\frac{dI}{dU}|_{U=0V}$ is of interest and has to be determined in terms of two-dimensional maps comparable to the topography. The software supplied with the system is not sufficient to analyze these special aspects. For this reason a homemade software developed by Thomas Becker [7] in the IDL [2] language was used to analyze the $I(U)$ curves at 0 V. The program was extended for this work for a correlation analysis of the data. In the following, after a brief description of the general features of the program, the additional parts will be introduced.

The program saves the spectroscopy curves in an array for further processing. The derivatives of the curves at $U = 0$ V are determined in two different ways shown in Fig. 5.12. On the one hand the curves are fitted with a polynomial of 5th order and then differentiated. Afterwards the point $\frac{dI}{dU}|_{U=0V}$ is determined. This seems to be a quite exact method, but the more noise in the data the more difficult is the fitting, even in cases of periodic vibrations. In some cases it would be sufficient to fit a polynomial of 3rd order or it would be better to use one with 7th order. On the other hand the second analysis is a very simple method: Only the linear part of the spectroscopy curve is used and fitted with a straight line, while the number of data points used in the vicinity of 0 V could be chosen by hand. This method has the advantage that outlier points at higher voltages do not play a role in the fitting. One disadvantage is the difficulty to find the purely linear part which might vary slightly for each spectroscopy curve. For a mainly qualitative analysis the latter is a minor problem and produces some systematic errors within the linear slope, but the differences in the slope between individual curves can be compared very well. All the derivatives are then plotted in a two-dimensional map corresponding to the topographic points of the picture. The program also can determine possibly existing gaps, described in the thesis mentioned above. In addition histograms could be plotted. They show the distribution of the conductivities taken within one picture and can be used to gather the nature of the distribution, which was mainly Gaussian like.

The method described so far was used to find local differences of the local tunneling conductivity in order to gain insight into phase separation phenomena. For a deeper insight additionally a correlation analysis was implemented, such that more could be learned about the occurrence of the different regions and a possible connection to the topography. With the help of an autocorrelation it is possible for example to compare structures within one picture. It is a self-correlation and can be calculated via two dimensional Fourier transforms[18, 3] as a convolution. Simply speaking, an autocorrelation compares a picture with itself by moving a copy of the picture on top of the "original" one and summing up the (topography) values with respect to the shifting of both pictures. This leads to the two-dimensional autocorrelation. Similar to height-height correlation functions [19, 14] an auto-correlation between the tunneling conductivities was calculated here and then averaged radially.

For the analysis in this case it was less profitable to analyze the two dimensional

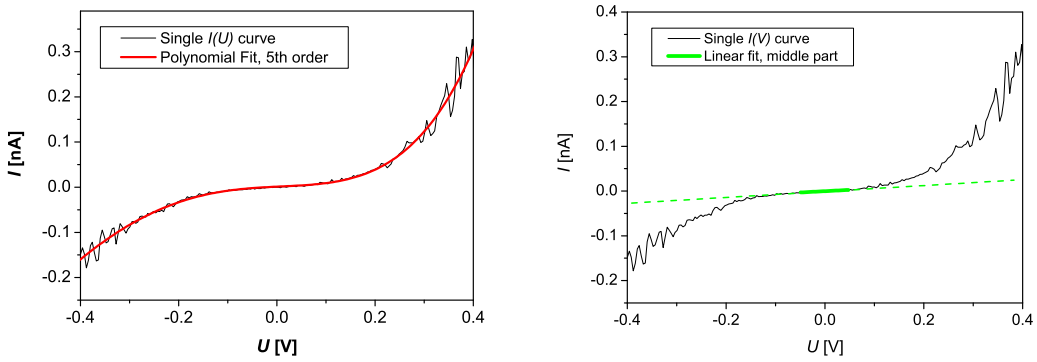

Figure 5.12.: Fitting example for a single $I(U)$ curve with a polynomial of 5th order (left) and a line for the linear part (right).

correlation maps. They show changes of the regular structure, including the contained tip structure, but the determination of relevant length scales is inefficient. Due to this fact the radially averaged autocorrelation function, $C(r)$, is calculated. The radii r are computed in terms of pixel integer values and for the final radial correlation function the pixel radii are converted into the topographic scale in nm. The correlation functions then are normalized, while a mean value was subtracted before from the uncorrelated two-dimensional maps to eliminate plane effects. To show an example the test pictures in Fig. 5.13 were drawn and saved in the format of the microscope program, such that they could be analyzed in the same way as measured data. The respective two-dimensional autocorrelation image is presented in the lower left of Fig. 5.13. The radial autocorrelation function is demonstrated in Fig. 5.14.

For the size analysis only empirical formalisms can be used. Since it does not yield exact length scales it is mostly important to analyze the radial correlation curves consistently. There are three features, which might be evaluated, that is the first decay, the first minimum and the first maximum of $C(r)$. Intuitively the first decay is related to the dimensions of corresponding structures (the correlation decreases with further shifting of the pictures). In the same way the first minimum might be interpreted of a mean corresponding to the largest dimensions of the existing structures (where the concurrence is minimal) and the first maximum occurs on a length comparable to the distance between regularly distributed objects. If there is no periodicity of the occurrence of structures (i.e. there is no distinctive distance) no maximum will occur. Often the first decay length, also called the correlation length, is determined as the radius r_l at which the normalized correlation $C_{\mathrm{norm}}(r)$ is decreased to $1/e$ by fitting a simple exponential function $y = A \cdot \exp(-r/r_l) + y_0$.

To demonstrate the effect of noise, which is always present in measurements, some artificial noise was added to the test picture (Fig. 5.13 upper right). Due to the noise the analysis does not find any correlation between neighboring pixels, which appears as the steep decay at the smallest radii (Fig. 5.14 a), whereat the structure of the curve remains the same. The latter problem can be solved by

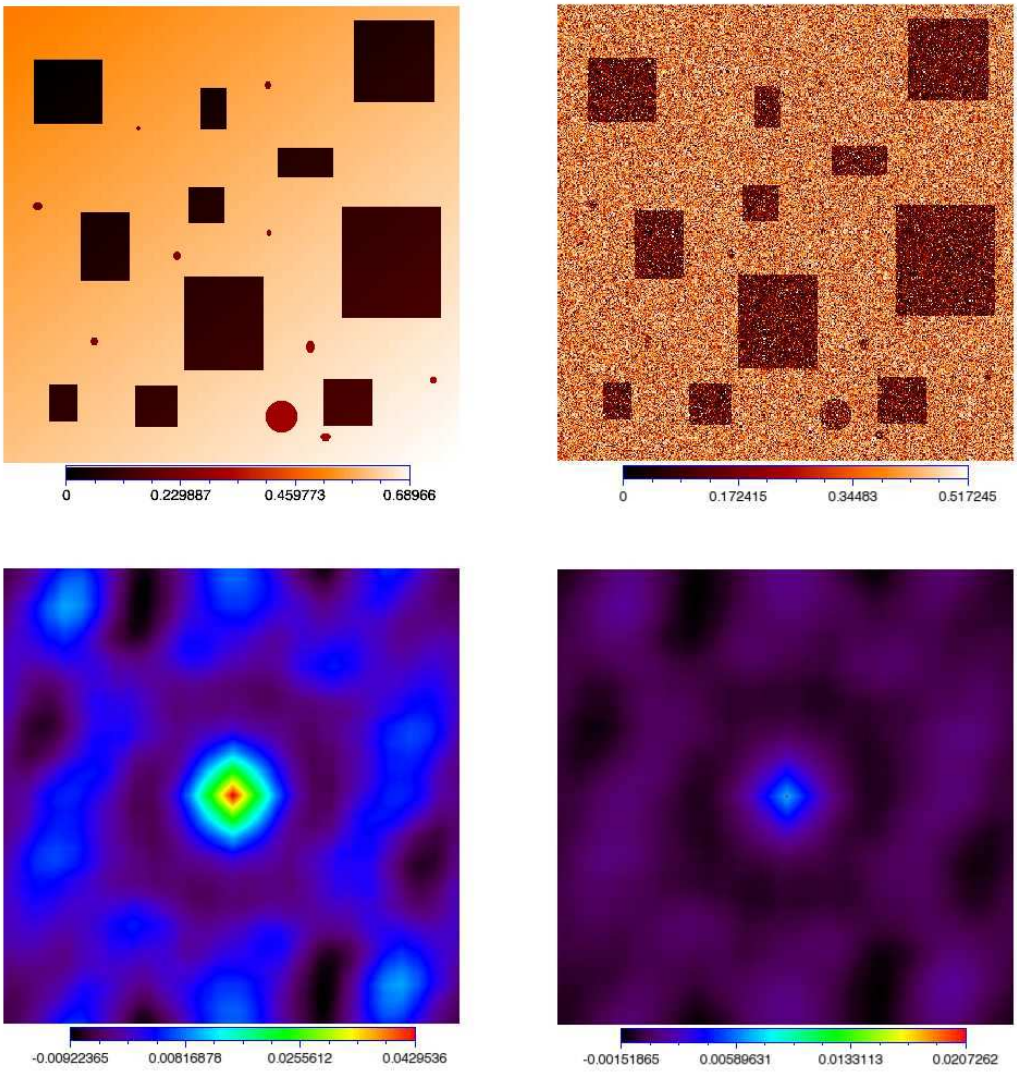

Figure 5.13.: Upper part: Test pictures (topographies) to demonstrate the correlation analysis with a given "fake" size of 200 nm×200 nm and height scales (arbitrary units).In the right picture virtual noise was added. Lower part: Two dimensional autocorrelation function of the pictures above.

taking out the first point of $C(r)$ and normalization with respect to the next point (Fig. 5.14 b). For the test picture without noise, this length is $r_l = 11.9(4)$ nm and for the picture with noise $r_l = 12.2(5)$ nm, which agrees quite well and corresponds roughly to the smallest side length of the rectangles. It shows, that within a certain noise range the data still can be evaluated without loss in accuracy. For larger radii this problem is wiped out by averaging over a larger number of pixels lying in the respective range. In any case it is only possible to determine sizes with minimum of a few pixel or otherwise the statistics fails. In most cases the maxima and minima were not very pronounced and therefore not analyzed. Of course the exponential

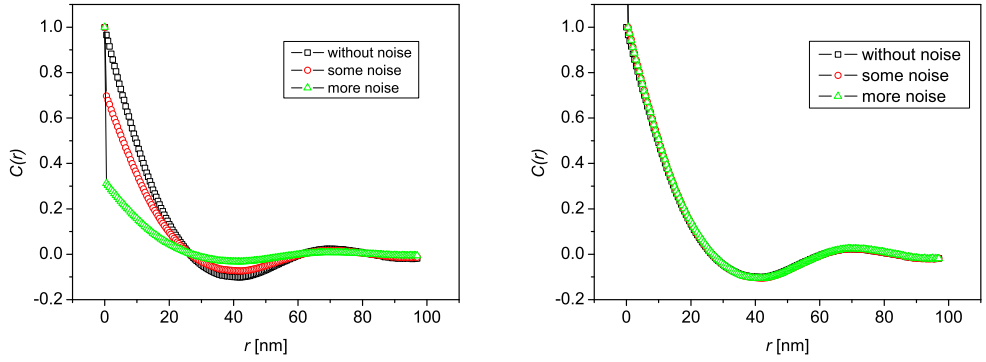

(a) **(b)**

Figure 5.14.: Normalized radial correlation functions $C_{\text{norm}}(r)$ of the pictures in Fig. 5.13 with different noise levels (a). The highest noise level corresponds to the upper right picture in Fig. 5.13. The noise leads to a step function at the first point, but the overall shape remains the same. The radial correlation functions for the noise included analysis are normalized on their second point (b).

decay is also only an approximation and does not reproduce the $C(r)$ curves exactly. It is mainly important to use always the same analysis for a relative comparison between different pictures. In case of a topography with flat terraces it was not possible at all to see any exponential decay, since the terraces are no distinguishable and restricted structures.

Bibliography

[1] DORMA Hüppe Raumtrennsysteme GmbH, Westerstede/Ocholt, Deutschland.

[2] IDL – Interactive data language. Research Systems, Inc. Version 6.0.

[3] IDL – Reference guide. Technical report, Research Systems, inc., 1998.

[4] Pico - the omicron nanotechnology newsletter. Technical report, Omicron, December 2003.

[5] Teragon's summary of cryogen properties. http://www.trgn.com/database/cryogen.html, February 2005. Teragon Research, San Francisco, CA.

[6] N. H. Balshaw. Practical cryogenics. Technical report, Oxford Instruments Superconductivity Limited, 2001.

[7] T. Becker. *Untersuchung der elektrischen Phasenseparation in dünnen Manganatschichten mit Rastersondenspektroskopie*. Doktorarbeit, Universität Göttingen, 2004.

[8] T. Becker, C. Streng, Y. Luo, V. Moshnyaga, B. Damaschke, N. Shannon, and K. Samwer. *Phys. Rev. Lett.*, 89:2372038, 2002.

[9] Dawn. A. Bonnell, editor. *Scanning Tunneling Microscopy and Spectroscopy*. VCH Publishers, Inc., 1993.

[10] C. Julian Chen. *Introduction to Scanning Tunneling Microscopy*. Oxford University Press, 1993.

[11] C. Enss and S. Hunklinger. *Tieftemperaturphysik*. Springer-Verlag, Berlin, 2000.

[12] D. Frickel. Omicron nanotechnologies, Personal communication.

[13] David R. Lide, editor. *CRC Handbook of Chemistry and Physics*. CRC Press. Boca Raton, Florida, 2003.

[14] S. G. Mayr. *Oberflächenrauigkeit von amorphen ZrAlCu-Schichten*. Diplomarbeit, Universität Augsburg, 1997.

[15] M. Okano, K. Kajimura, S. Wakiyama, F. Sakai, W. Mizutani, and M. Ono. *J. Vac. Sci. Technol. A*, A5:3313, 1987.

[16] Omicron Nanotechnology. *Cryogenic SFM: User's Guide and Service Manual*, 2001.

[17] Oxford Instruments. *Operator's handbook: Spectromag SFM*, February 2003.

[18] W. H. Press, S. A. Teukolsky, W. T. Vetterling, and B. P. Flannery. *Numerical Recipes in C*. Cambridge University Press, 1992.

[19] B. M. Reinker. *STM-Untersuchungen an amorphen ZrCo- und CrAlCu-Aufdampfschichten*. Doktorarbeit, Universität Augsburg, 1997.

[20] U. Tietze and Ch. Schenk. *Halbleiter-Schaltungstechnik*. Springer Verlag, 1971.

[21] L. E. C. van de Leemput and H. van Kempen. *Rep. Prog. Phys.*, 55:1165, 1992.

[22] W. Wulfhekel. Personal communication.

[23] M. Wutz, H. Adam, and W. Walcher. *Theorie und Praxis der Vakuumtechnik*. Friedr. Vieweg & Sohn Verlagsgesellschaft mbH, Braunschweig, 1988.

6. The basic sample properties

Different films of $La_{0.75}Ca_{0.25}MnO_3$ were prepared by the MAD technique (Chap. 4.1) on MgO(100) substrates. By varying the deposition parameters (see detailed data App. A), different growth modes were observed, that is from a grain like (3D) growth to a layer-by-layer (LL) growth. The films differed slightly in their general properties like the microscopic structure, the resistivity and the metal-insulator transition temperature, but the sharpness of the MIT varies with the differences in structure. Expressing the growth modes either a grainy surface or flat terraces were observed by STM measurements. In other words a different degree of lattice distortions and ordering in the samples could be accounted for the different growth conditions. The varying microstructures play a crucial role in the magnetic and electronic properties in manganites [9], being rooted in the exchange mechanisms which rely sensitively on bond angles and distortions (Chap. 2). An evolution with respect to the ordering in dependence on the growth modes was observed for a series of films. It was impossible to investigate all these films with STS, but the overall structural and other general properties are important in order to put the used films into a more general perspective. In a sample series even a cation ordering on the A-site as the "top end" of stringent ordering was observed by HRTEM pictures [6] and STM investigations on atomic scale [8]. In this case not only a perfectly oriented crystal lattice, but also an ordering of the ions evokes the sharp and pronounced MIT.

In this chapter the structural and commonly measured standard properties will be given to summarize the sample characteristics. These results are essential to understand the microstructure and hence the following results of the electronic properties, which are observed on a microscopic scale by the STS measurements. There are different models to explain the MIT and its mechanism, but they can only be discussed knowing the microstructure of the samples. There might be differences due to not perfectly built samples, that is, some effects might arise from extrinsic effects like structural irregularities [1, 10, 9] caused by lattice strain from the substrates, grains in different orientations, oxygen content, etc. Since it is therefore in general difficult to produce perfect manganite samples and especially thin films, the latter effects have to be considered in a discussion of the electronic mechanisms.

6.1. Growth mode

As a starting point the topographies from two of the differently prepared films give an impression about the structural sensitiveness in relation to the deposition conditions. These differences can be ascribed mainly to the different deposition rates, which were 0.64 ml/min (precurser solution per time) for the 3D and 0.125 ml/min

for the LL sample in this special case. The STM images of the two films used throughout this work are shown in Fig. 6.1. They were taken under UHV condition (and the scanning parameters were 0.7 V/0.2 nA for the LL sample and 0.5 V/0.2 nA for the 3D sample). The difference in morphology evidently can be seen in these pictures. The 3D sample[1] shows grains and sometimes even observably growth spirals like for the grain on the lower left corner. The rectangular shape of the grains could be expected from the tetragonal structure for $La_{0.75}Ca_{0.25}MnO_3$. In contrast, the LL film shows a terrace structure with a terrace width of about 60-80 nm and a height[2] of roughly 0.4 nm reflecting the lattice parameter of the perovskite cell. Mainly steps of one unit cell height are observed, sometimes a double step occurs. Within one terrace a buckling can be observed, some assumptions about a possible explanation are given later. The root mean square (rms) roughnesses σ determined from these STM images ($\sigma_{3D} \approx 2$ nm and $\sigma_{LL} \approx 0.2$ nm for the plane fitted samples) are practically the same as those measured by SAXS shown below. The 3D film is much rougher than the LL film as expected from the optical impression of the STM images.

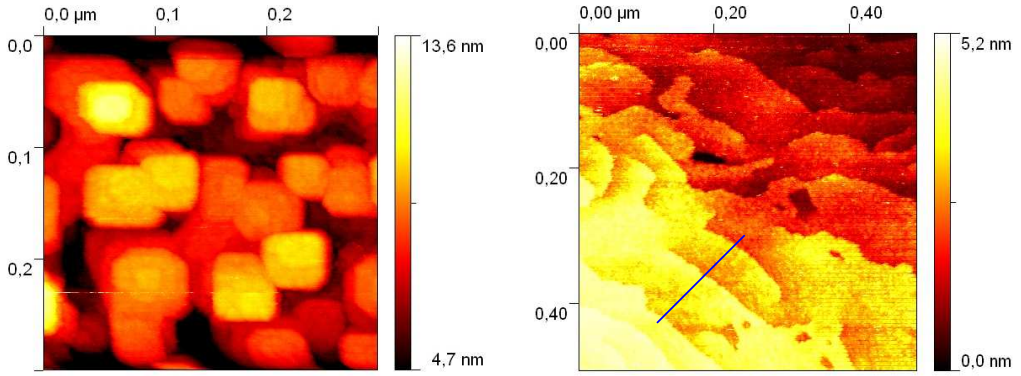

(a) 3D Topography **(b)** LL Topography

Figure 6.1.: Topographies of 3D (left) and LL (right) film showing a grain-like and layer-by-layer growth measured by STM. The rms roughnesses are $\sigma_{3D} \approx 2$ nm for the 3D and $\sigma_{LL} \approx 0.2$ nm for the LL film.

6.2. Structural properties

The structure of the films was investigated by wide angle X-ray scattering. The perpendicular to plane lattice parameter (of the pseudo-cubic perovskite structure) a_p and the film thickness d as well as possibly different phases were determined. The $\Theta/2\Theta$ diffraction patterns of the 3D and LL samples are shown in Fig. 6.3, in

[1] The image is plane fitted, that is, a global plane was subtracted from the image, which is a typical procedure to make the structures visible, in the case of a somewhat tilted sample plane with respect to the x-y-scanning plane.

[2] The resolution is not sufficient to determine the exact terrace height.

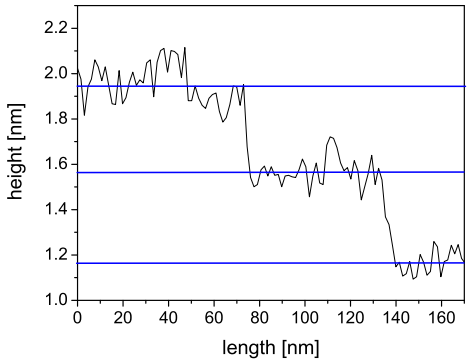

Figure 6.2.: Lineprofile for the LL sample (line is marked in the right image of Fig. 6.1). The step heigth is about 0.4 nm.

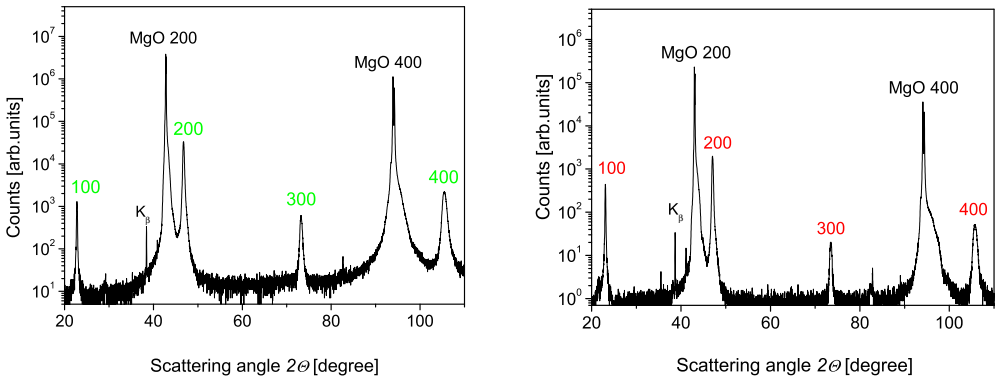

Figure 6.3.: XRD patterns of the LL (left) and 3D (right) sample. Only the peaks for the (h00) planes can be seen. (The background for the measurements is different, since they were taken in two different diffractometers.)

which only the (h00) planes of the pseudo-cubic perovskite cell can be seen and no other orientations or manganite phases occur.[3] For the calculation of the lattice parameter, the MgO(200) peak was taken as a reference and the 2Θ angle was corrected respectively before the calculation was made. The (200) peaks were taken for the determination and fitted by Gaussian functions. The calculated parameters can be seen in Tab. 6.1, they correspond to the bulk value of $a_p^{bulk} = 0.3876\,\text{nm}$ [7]. The lattice parameter of the cubic MgO is $a = 0.42112\,\text{nm}$ [2] and the lattice mismatch is 8 %. Therefore some strain could be expected, but the latter relax by misfit dislocations within the first atomic layers (see HRTEM picture) on the substrate. The experience with similar films and their HRTEM pictures [5, 6], also predicts that there is no significant strain.

In this case the film thicknesses are about $d \approx 50 - 70\,\text{nm}$ (compare Fig. 6.4).

[3] The very small additional peaks for the pattern of the 3D sample arise from the Al-sample holder, since the sample was quite small and did not cover the holder completely.

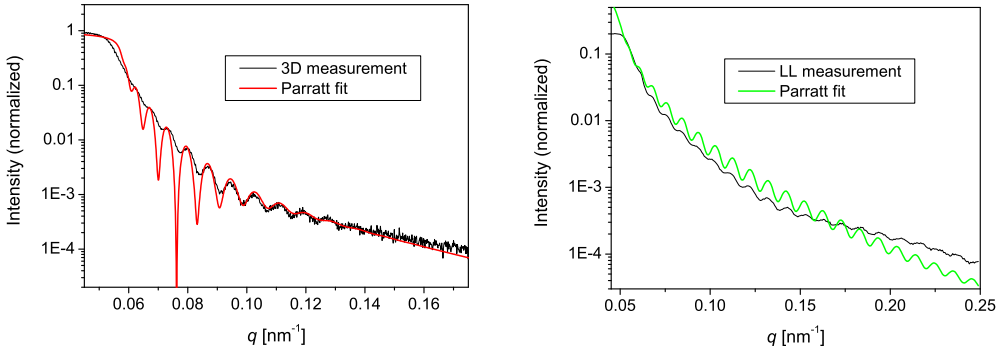

Figure 6.4.: SAXS measurements for the 3D (left) and LL (right) sample and their respective Parratt fits.

The roughnesses (see Tab. 6.1) determined by fitting the SAXS measurements with the Parratt algorithm reflect the different topographies afore mentioned. They are slightly higher than those measured by STM. But this is expected, since SAXS is covering a much bigger area on the sample and any greater irregularity is influencing the whole measurement.

In Fig. 6.5 a TEM cross-section of an LL film shows the homogeneity of the films. The HRTEM picture in the same figure demonstrates the relaxation mechanism of the LCMO film grown on a MgO substrate[4]. The first 3-4 layers grow epitaxially (that is atom on atom) on the MgO substrate and are expected to be strained. Nevertheless, most probably the stress is prevented by misfit dislocations which is indicated by the broken lines in Fig. 6.5 for an LL sample.

Additionally, instead of the typical orthorhombic (P_{nma}) structure the rhombohedral ($R\bar{3}c$) structure was observed for the LL films [6, 4] in electron diffraction (ED) patterns (compare structures in Fig. 2.4, p. 9), see the examples in Fig. 6.6; it accommodates to the cubic perovskite structure. Instead, the 3D films are a little bit different and show the typical orthorhombic structure expected for $La_{0.75}Ca_{0.25}MnO_3$, that is the perovskite cell is tetragonal. Since the films used for the TEM measurements show very similar characteristics compared to the films described in this thesis, these structural properties are expected to be the same for the 3D and LL films shown in Fig. 6.1 and used for the STS measurements, although there are no

[4]Both pictures are not taken from the samples demonstrated so far, similar samples with similar characteristics were used for the TEM pictures.

Sample	lattice parameter a_p [nm]	thickness d [nm]	roughness σ [nm]
LL	0.3872(4)	59(5)	≈ 0.4
3D	0.3869(5)	62(5)	≈ 2.6

Table 6.1.: Lattice parameter a_p (out-of-plane) taken from the {200}-peaks of the XRD patterns, thickness d and (rms) roughness σ from SAXS for the LL and 3D film determined by X-ray scattering.

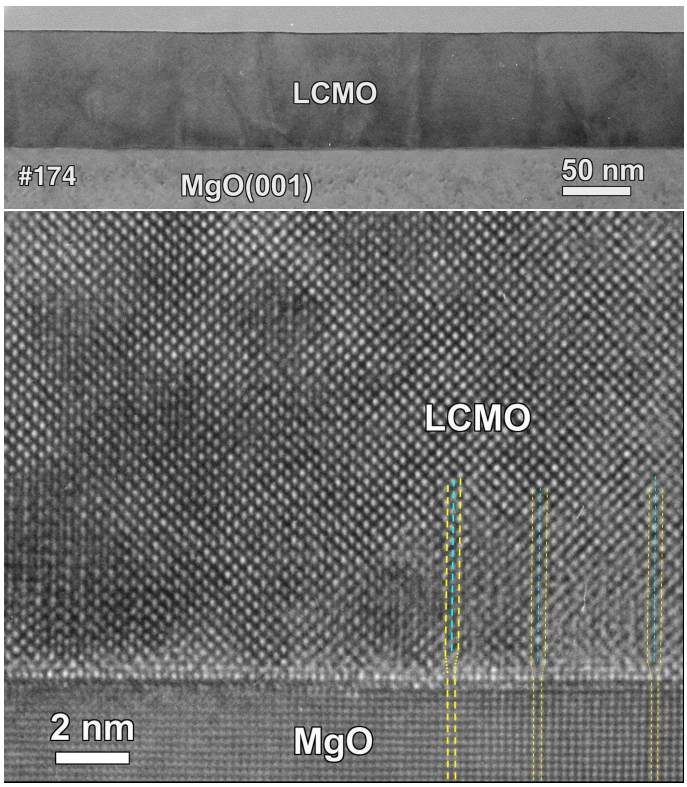

Figure 6.5.: Upper: TEM cross section of a film similar to the LL-film used here. Lower: HRTEM picture of LL-film to demonstrate the relaxation by misfit dislocations (broken lines).[a]

[a]The TEM measurements were done by O. I. Lebedev in the group of G. van Tendeloo, EMAT, University of Antwerp, Groenenborgerlaan 171, 2020 Antwerpen, Belgium

HRTEM images and ED patterns available for exactly these films.

6.3. The metal-insulator transition

The temperature dependence of the resistance of the films shows the typical behavior for manganites in this doping region (see Chap. 2). The metal-insulator transition takes place at T_{MI}=270 K for the LL sample and at T_{MI} =263 K for the 3D sample (the values for the bulk transport properties are summarized in Tab. 6.2). The T_{MI} can be read directly from the resistance curves. The $R(T)$ curves are plotted in Fig. 6.7 (a) and it can be seen that the specific resistivity is somewhat lower for the LL sample.

The sharpness of the transition can be analyzed according to Mitra et al. [3] with the help of the logarithmic derivative

$$\alpha = d\ln R/d\ln T \tag{6.1}$$

as a kind of quality factor. It is physically motivated by disorder effects (Chap. 8)

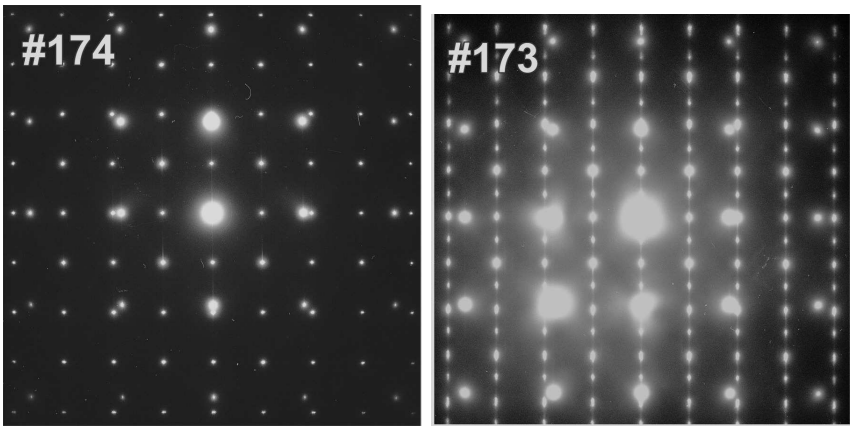

Figure 6.6.: Cross-section electron diffraction patterns of an LL film (left) with a rhombohedral structure and a 3D film (right) with an orthorhombic structure (indicated by the additional rows of spots).[a]

[a] TEM measurements done by O. I. Lebedev, group of G. van Tendeloo, EMAT (Antwerpen, Belgium).

and it describes the curve and takes on a maximum value α_{max} at the steepest slope. At the transition temperature $\alpha = 0$ due to the derivative dR/dT being zero. In general the sharpness of the transition is a measure for the quality of the transition and therefore the quality of the sample. The logarithmic derivative behaves comparably to the transition temperatures, namely the transition for the LL film is sharper since $\alpha_{max} = 46$ is higher than for the 3D film with $\alpha_{max} = 26$ (Fig. 6.7 b). The structural changes of the films are connected with the MIT characteristics and is discussed in Chap. 8.

6.4. Magnetic properties and magnetoresistance

The temperature dependent magnetization can be see in Fig. 6.8. The curves are normalized to the lowest temperature of 5 K and behave similarly to the resistance with respect to the sample differences. This again can be determined by the logarithmic derivatives according to the analysis of the resistance. The T_C for both samples is about 260 K, but the transition for the 3D sample is broader. The magnetization versus field[5] in the vicinity of the transition is shown in Fig. 6.8 on the

[5] In course of the diamagnetic substrate signal, a straight line was subtracted from the measurements.

Sample	T_{MI} [K]	ΔT_{trans} [K]	α_{max}	MR_{max} [%]
LL	270(1)	≈ 9	46	79(2)
3D	262(1)	≈ 19	26	77(2)

Table 6.2.: Transport properties of the films: Metal insulator transition temperature T_{MI}, width (FWHM) of transition ΔT, sharpness α_{max} and maximum MR_{max}.

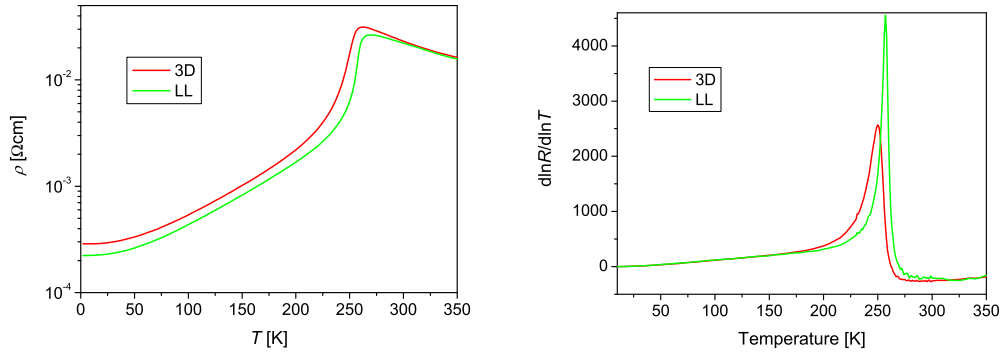

(a) (b)

Figure 6.7.: Specific resistivity of measured 3D (red) and LL (green) sample (a). The sharpness of the transition demonstrated by the logarithmic derivatives α for 3D and LL sample (b).

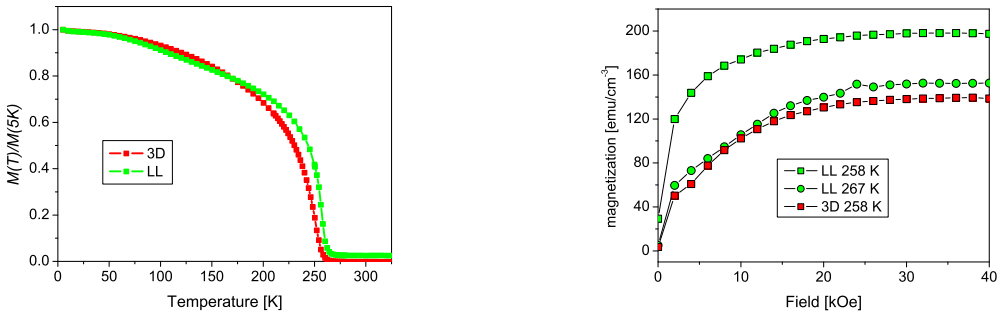

Figure 6.8.: Left: Normalized magnetization versus temperature at $H = 100\,\mathrm{Oe}$ for 3D (red) and LL (green) sample. Right: $M(H)$-curves for 3d and LL film at transition temperatures, which were also used for the STS measurements.

right. For the LL film the curve at 258 K is higher than those for 267 K reflecting the transition, since one lies below and the other one slightly above the magnetic transition. The magnetoresistance (MR) curves shown in Fig. 6.9 below demonstrate a matching behavior. In case of the 3D film the measured $M(T)$ curve shows a lower magnetization than for the LL film at the same temperature, although it is lying below the transition. But since the transition is broader, it should be expected to observe somewhat lower values for this film at this temperature.

Since the STS measurements were performed in magnetic fields, the MR

$$MR(T) = \frac{R(H=0,T) - R(H,T)}{R(H=0,T)} \tag{6.2}$$

was determined in a 40 kOe field for the whole temperature region (upper part of Fig. 6.9). For some temperatures in the vicinity of the MIT the MR with respect to the field is drawn in Fig. 6.9. The slopes of the curves at smaller fields $\approx 10\,\mathrm{kOe}$

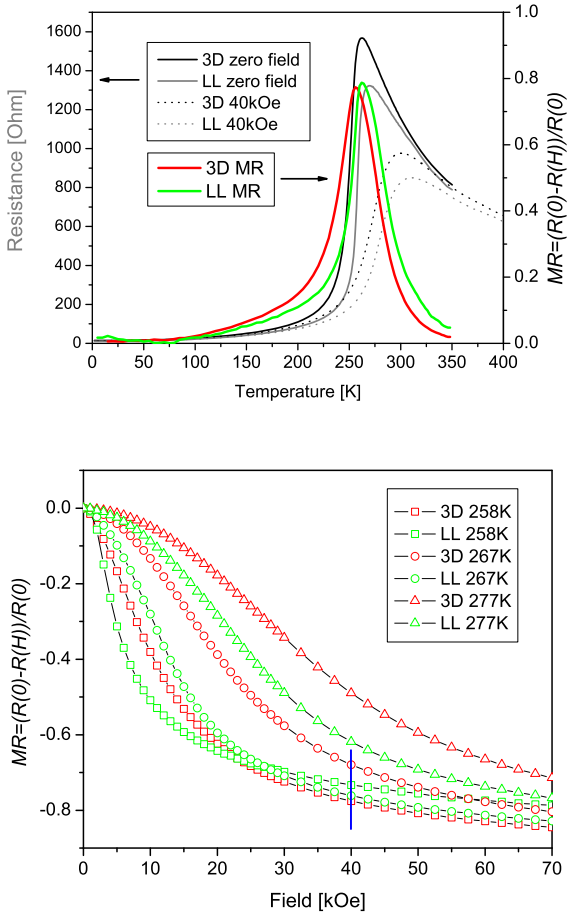

Figure 6.9.: Magnetoresistance at different temperatures for the 3D (red) and LL (green) sample, with the field applied out of plane. The parameter region used mainly for the STS measurements is marked in blue.

are largest in the temperature region of the MIT, representing the magnetization behavior. For fields $\geq$ 40 kOe (depending on the temperature) the MR starts to approximate a saturation value, although there is no "real" saturation observable for manganites [9].

Bibliography

[1] B. I. Belevtsev. *Low Temp. Phys.*, 30:421, 2004.

[2] A. Kern, R. Doetyer, and W. Eysel. JCPDS-International Center for Diffraction Data, 1995. MgO, CuKα_1 radiation.

[3] J. Mitra, M. Paranjape, A. K. Raychaudhuri, N. D. Mathur, and M. G. Blamire. *Phys. Rev. B*, 71:094426, 2005.

[4] V. Moshnyaga. Personal communication.

[5] V. Moshnyaga, B. Damaschke, O. Shapoval, A. Belenchuk, J. Faupel, O. I. Lebedev, J. Verbeeck, G. van Tendeloo, M. Müksch, V. Tsurkan, R. Tidecks, and K. Samwer. *Nat. Mat.*, 2:247, 2003.

[6] V. Moshnyaga, L. Sudheendra, O. I. Lebedev, S. A. Köster, K. Gehrke, O. Shapoval, A. Belenchuk, B. Damaschke, G. van Tendeloo, and K. Samwer. *Phys. Rev. Lett.*, 97:107205, 2006.

[7] P. G. Radaelli, G. Iannone, M. Marezio, H. Y. Hwang, S.-W. Cheong, J. D. Jorgensen, and D. N. Argyriou. *Phys. Rev. B*, 56:8265, 1997.

[8] L. Sudheendra, V. Moshnyaga, E. D. Mishina, B. Damaschke, Th. Rasing, and K. Samwer. *Phys. Rev. B*, 75:172407, 2007.

[9] Y. Tokura, editor. *Colossal magneto-resistive manganites*. Gordon and Breach Science Publishers, 2000.

[10] M. Ziese. *Rep. Prog. Phys.*, 56:143, 2002.

7. STM and STS results

In the following chapter the STM and STS measurements of the 3D and LL samples are described. The spectroscopy analysis will be presented together with the topographies of the sample areas on which the spectroscopy data were taken. The emphasis lies on the measurements in a magnetic field in comparison with measurements without a field applied. The STM and STS measurements will be presented for the 3D and LL samples in two separate parts, a comparison between these samples and with the results from other groups is going to follow in the discussion Chap. 8.

The magnetic field tunes the properties of the samples while it shifts the MIT towards higher temperatures which is a nice opportunity to learn more about the MIT behavior and additionally this can be done on a very localized scale. The measurements regarding magnetic field effects extend the STS measurements of T. Becker [1], which could only be performed with respect to different temperatures. It should be noted at this stage, that the samples used by T. Becker were mainly produced by sputtering and show a different morphology, namely a grain growth, and a larger resistivity. The MAD samples are further developed and therefore better characterized in their nature. The investigations of this work concentrated mainly on observations nearby the metal insulator transition temperature, since a detailed study including temperature dependencies was unfortunately not possible under the given conditions.

On the basis of the resistance measurements a temperature range near the MIT was chosen to perform the main STS measurements within magnetic fields. At these temperatures the field effects are expected to be high while the samples are turned into more metallic like behavior by the magnetic field.

In this chapter the tunneling conductivities from the STS measurements will be presented. At first it is important to note that the tunneling conductivity and the bulk conductivity are not the same quantity and the first should not be confused with the latter described in the last chapter[1].

Here the spectroscopy data was analyzed by the linear part of the $I(U)$-curves as stated in Chap. 5.3 and this will also be the case in the following images, if not anything else is stated. The spectroscopy data was plotted with respect to its topographical location and forms a conductivity map, which can be directly compared to topographical features at the same position.

[1] In connection with the STS measurements always the tunneling conductivity is meant within the discussion, even if it is only written about the conductivity.

7.1. Film with three dimensional growth mode

7.1.1. Histogram analysis

In the last chapter it was shown how the individual spectroscopy curves are analyzed with respect to the tunneling conductivity at zero bias. For each measurement the determined values of the tunneling conductivities are plotted in a two-dimensional conductivity (or STS) map and additionally summarized in a histogram. The histograms help to compare the different measurements more quantitatively with respect to the mean tunneling conductivities. A positional correlation is not included in these considerations, but will be discussed later (Chap. 8).

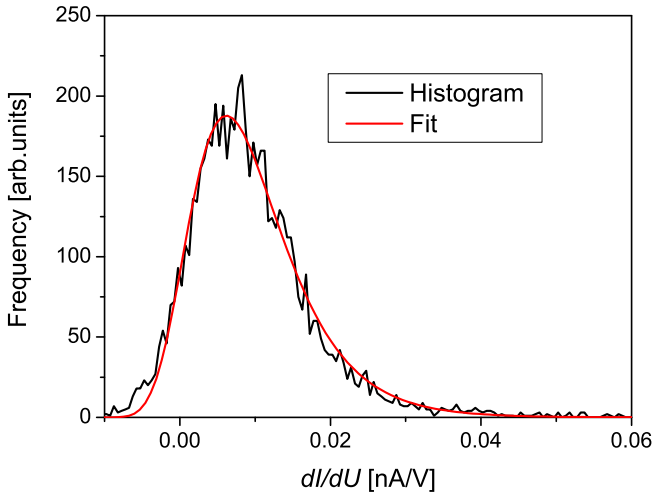

Figure 7.1.: Example for fitting a histogram curve with the extreme function for the tunneling conductivities.

An example for a histogram and its fitting curve is shown in Fig. 7.1. For the fitting function the extreme peak function with amplitude A, width w and center x_c

$$y = y_0 + A \cdot e^{\left(-e^{(-z)}-z+1\right)} \quad \text{with} \quad z = \frac{x - x_c}{w} \tag{7.1}$$

was chosen. This matches best with the slight asymmetry of the histograms. This asymmetry is only observed for the 3D samples and will be discussed again later (Chap. 8). The choice of the distribution function was taken to fit the histogram peak for a quantitative comparison of the measurements. The distribution is composed of some noise[2] and the electronic features of the sample. The latter are not necessarily equally distributed, hence it is difficult to find a physically motivated distribution function. The LL films (see below) could be fitted by simple Gaussian peak functions.

[2] The noise level from the 3D sample is a little bit larger due to a more pronounced z-piezo movement.

7.1.2. Temperature dependence

The 3D samples will be described first. They are expected to show a different behavior than the LL samples. Due to their less ordered microstructure locally less homogeneous sample properties should be the result.

At first, the temperature behavior of the overall tunneling conductivity is of interest. From T. Becker [1] it is already known that the tunneling conductivity follows the bulk conductivity in the sense that both decrease with increasing temperature up to the MIT and then increases again.

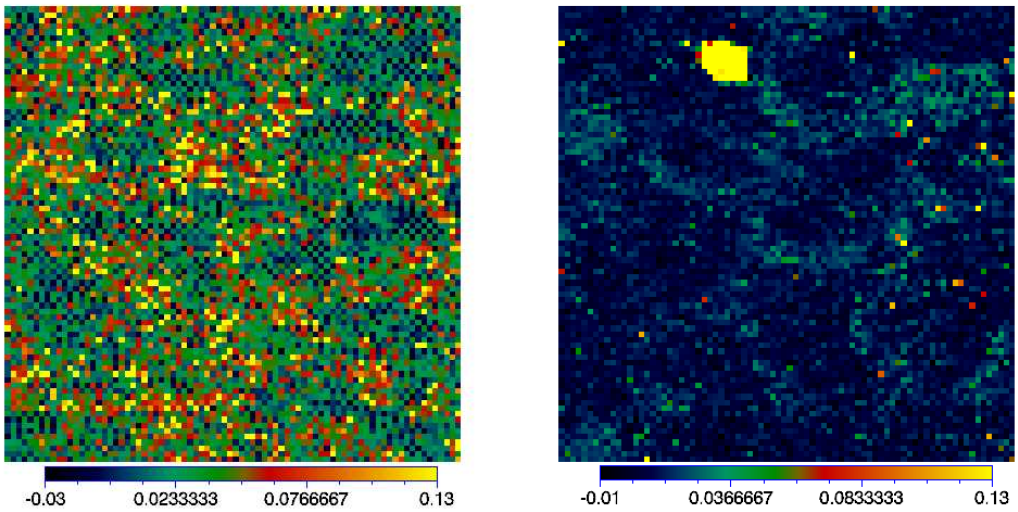

(a) dI/dU [nA/V]: $T = 60\,\mathrm{K}$ **(b)** dI/dU [nA/V]: $T = 221\,\mathrm{K}$

Figure 7.2.: STS images for the 3D sample at 60 K (a) and 221 K (b).[a] The size of both pictures is $300 \times 300\,\mathrm{nm}^2$.

[a] The yellow spot with very high conductivity is some metallic dirt on the sample and can also be seen as a topographic feature.

In Fig. 7.2 two examples for maps of tunneling conductivities at 60 K (a) and 221 K, (b) which are taken for the same parameters (bias voltage and feedback current)[3] of 0.5 V/0.2 nA, are shown within an area of $300 \times 300\,\mathrm{nm}^2$. Each pixel stands for the zero bias differential tunneling conductivity $dI/dU|_{U=0V}$ from a single point on which an $I(U)$ curve was taken. In this case a grid of 80×80 points was chosen for the STS measurements.

For the linear regression only the twenty points around 0 V were taken for the analysis. This ensures that only the linear slope takes part in the analysis, otherwise the conductivities would increase in general, due to the nonlinear rise of the $I(U)$

[3] The bias voltage was always chosen to be under the workfunction of these manganites, which was determined to be about $\Phi = 1.2\,\mathrm{V}$, see e.g. [1].

curves. From previous work the size of a possible gap is known, which is larger than the twenty points of analysis and therefore its zero slope is unaffected. Some negative values arise from noise in the $I(U)$ curves: If there are outliers within the region of analysis, the resulting slope of the straight line might become negative.

The measurements in Fig. 7.2 were not taken at exactly the same position, since this is impossible due to thermal drift during the temperature change. Both pictures show an inhomogeneous distribution of the tunneling conductivities. The mean conductivities (taken as the peak of the histograms of the tunneling conductivity, explained below) are 18.4(8) pA/V for Fig. 7.2 (a) and 6.18(6) pA/V for Fig. 7.2 (b). Both tunneling conductivity maps are shown with the same color code and it easily can be seen, that the overall conductivity is decreased at the higher temperature. For the measurement at 60 K the tunneling conductivity is about one order of magnitude larger than for the value determined at 221 K. The latter means that this temperature is much closer to the MIT than the much more "metallic" like measurement at 60 K.[4] [5]

The temperature dependent measurements reflect the resistivity behavior of the sample, that is, the mean tunneling conductivity at lower temperatures ($T \ll T_{MI}$) is higher than for higher temperatures ($T < T_{MI}$) below the MIT and confirm the observations of T. Becker [1].

Of course the tunneling conductivity could not directly be compared to the bulk conductivity, but a behavior reproducing the bulk behavior in some sense is expected. In this case no gap map is plotted, because no distinct gap was observed.

7.1.3. Magnetic field dependencies

The magnetic field dependencies were measured at three different temperatures, namely at 60 K, 221 K and 258 K and are going to be discussed in this order. At the end the measurements are summarized for a comparison of the magnetic fields effect at different temperatures.

The measurement at 60 K (measurement A) was done without and also in an applied magnetic field of 50 kOe, the measurements are shown in Fig. 7.3 (a,b). Both tunneling conductivity distributions are inhomogeneous, which can be seen with the help of the color distribution and the darker and lighter areas, but both show similar structures and tunneling conductivities in the same order of magnitude. At this lower temperature the bulk MR is negligible (about one percent) and therefore no significant changes are expected for the tunneling conductivity.

An error analysis, that is the determination of the χ^2 values for each linear fit was performed as well. The calculation of χ^2 is implemented within the fitting routine of the IDL language. In Fig. 7.3 (c,d) the maps for the χ^2 distributions for the respective tunneling conductivity maps, shown above, can be seen. A good agreement with the experimental data is expressed by a low χ^2 value, which corresponds

[4] The word "metallic" is written in quotation marks since it is still much smaller than those of real metals like for example gold.

[5] Here and in the following the values which are lower or higher than those given with the shown scale bar are condensed onto the lowest or highest value in the scale bar respectively.

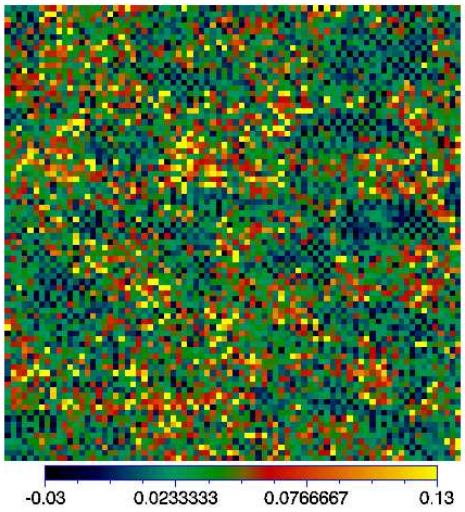

(a) dI/dU [nA/V]: zero field

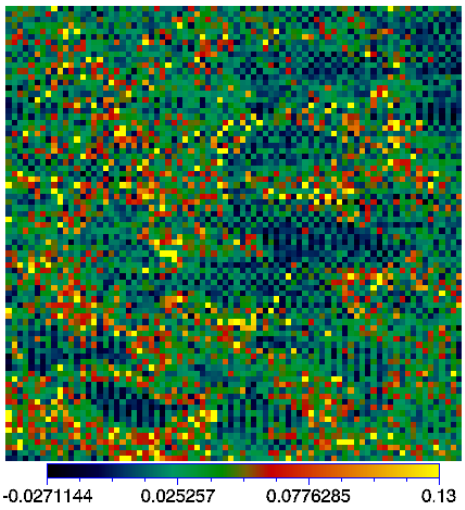

(b) dI/dU [nA/V]: 50 kOe

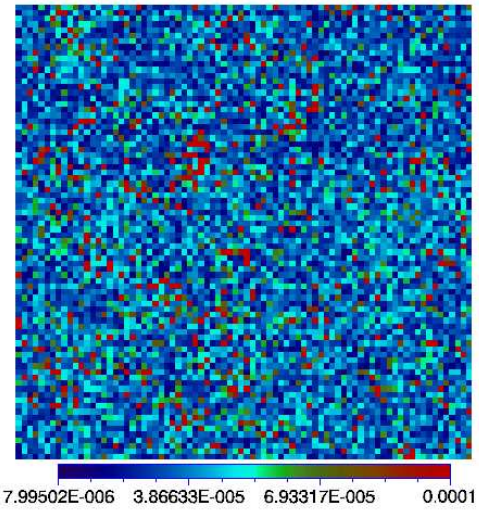

(c) χ^2 zero field

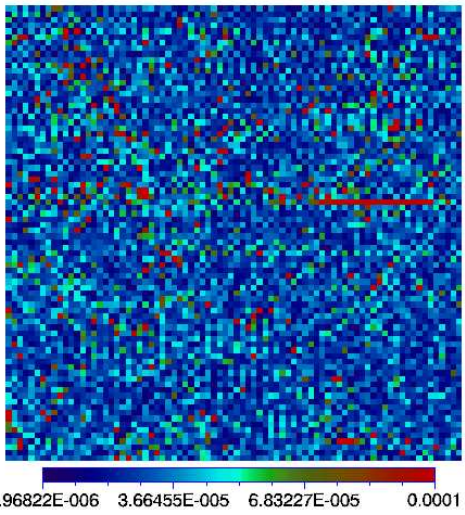

(d) χ^2 50 kOe

Figure 7.3.: STS images for the 3D sample at 60 K (measurement A) without field (a) and with 50kOe applied (b); except for a small drift to the left, the sample areas were the same for the two images. The respective maps of the χ^2-values are shown in (c) and (d).

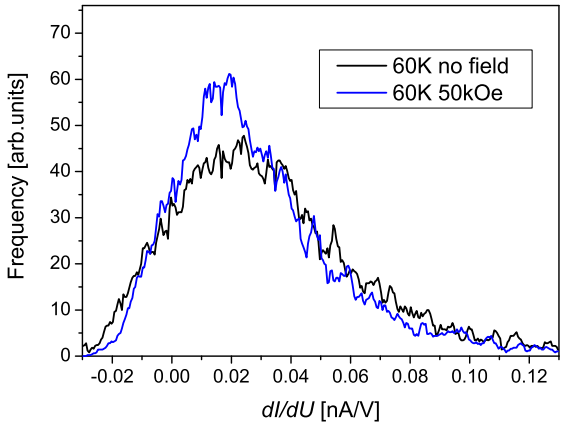

Figure 7.4.: Histogram for Fig. 7.3 at 60 K without and with a magnetic field applied.

to the dark blue spots in the figure, while the red points should be considered with care. It should be noted that systematic errors are not contained, because the linear fit is only done with the middle points of the spectroscopy curves.

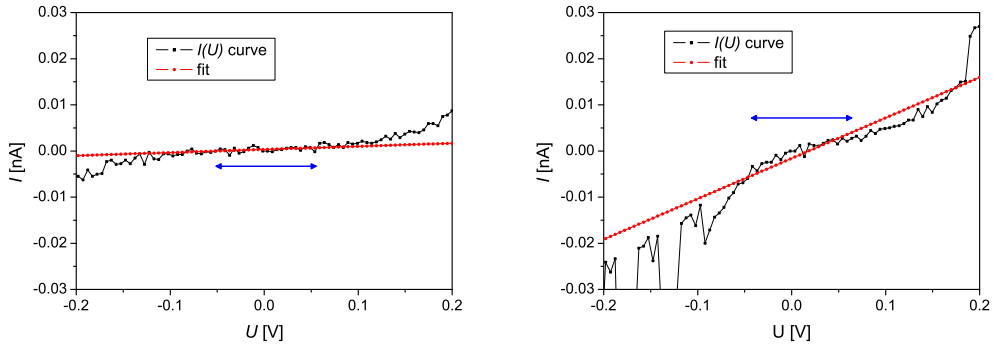

(a) $\chi^2 = 4.3\,10^{-6}$ **(b)** $\chi^2 = 7.5\,10^{-5}$

Figure 7.5.: Demonstration of the fitting and the resulting deviations: A very good linear fit (a) and a worst case fit (b). The $I(U)$ curves are taken from a zero-field measurement and the blue arrows mark the fitting region.

For a better impression about the fits two examples are shown in Fig. 7.5 (a,b) while the value for χ^2 is given below the plots. Only for a few fits the value of $\chi^2 = 2 \cdot 10^{-5}$ is exceeded (which is also true for the following measurements) and therefore Fig. 7.5 (d) shows an extraordinary bad fit with $\chi^2 = 7 \cdot 10^{-5}$. Generally the linear fits appear to be similar to the good fit demonstrated here and for the eye it would be difficult to see large differences[6].

[6] Some possibly deviations of the tip sample distance, because the feedback set could not be maintained for example, are not taken into account in the case of the linear fits and lead to

It is evident, that there is no net change as can be seen in Fig. 7.4 and the irregularities could be ascribed to the bad topography and probable tip changes. In general an artifact from the system due to the magnetic fields can be excluded, since this was tested on gold and there were no magnetic field effects found. In this case it can be ensured, that nothing happens with the sample properties at this temperature.

The latter observations were made far below the MIT, the next describe a different situation. For a temperature of 221 K (measurement B) the results differ as demonstrated in Fig. 7.6. The topography[7] states that the measurements with and without field were taken at exactly the same film area, except for a slight drift which cannot be totally prevented.[8] The topographies show a typical picture of a 3D growth mode (see also Chap. 6), with grains of more or less same size.

The STS results are plotted for zero field in Fig. 7.6 (c) and 40 kOe in 7.6 d. The bright yellow spot on these tunneling conductivity maps is some undefined metallic contamination, which can be located also in the upper part of the topographies. Both pictures do not show a homogeneous distribution of the tunneling conductivity. Instead, there are regions with qualitatively different $I(U)$ curves. These regions are expressed in the image by the different colors, whereat the regions do not have sharp edges, but a continuous transition.[9] This measurement is also suitable for a demonstration of the quality of the fits. In Fig. 7.6 (e,f) the values of χ^2 are plotted locally. Blue values mean a very good fit and with the red values the fit starts becoming bad. The tunneling conductivity rises with a magnetic field applied. This is the case not only for the regions with higher tunneling conductivity, but also for those with lower tunneling conductivity. Only a very few points remain with the same color. The rise in tunneling conductivity takes place systematically in that sense that the structure of the regions is preserved.

The topographies printed above the conductivity maps serve as a comparison of the local STS analysis with topographical features. The yellow spot in the tunneling conductivity, which show a metallic like STS curve can be identified as a small obstacle between the upper left grains. For an even better comparison a gray-scale topography and its respective conductivity map were superimposed in Fig. 7.7 (a). On some areas there is a small correlation between the regions of higher tunneling conductivity with the valleys between the grains, that is, some of the grains seem to be surrounded by the green/orange parts, but it does not apply for the whole region and happens supposedly by chance. On some grains better

some noise. At a first glance the influence of small deviations of the feedback set (due to a test with a normalization) is not so significant for the analysis at $I(U = 0)$, see the discussion later.

[7] The topography images were created by "Gwyddion 2.4", a free (GNU license) data analysis software for scanning probe techniques.

[8] The topographies were plane fitted, that is, a plane was subtracted from the picture to enhance the visibility of the grain structure (mostly the area scanned is tilted a little bit which dominates then the height distribution). This will also be the case in all of the next topographies and is not mentioned in every case, since this method does not change the information contained in the picture.

[9] At some spots the sharp changes from the colors (for example from green to red) might lead to an impression of sharp edges between different regions, although this is not the case here.

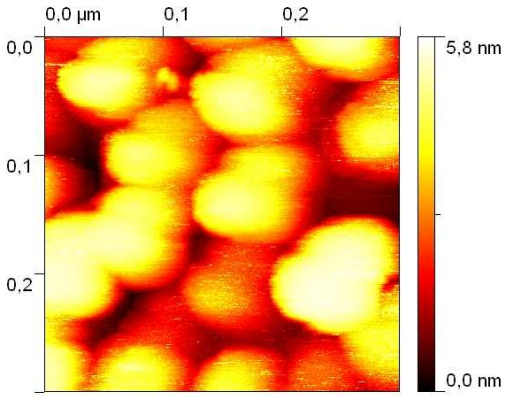

(a) Topography [nm]: zero field

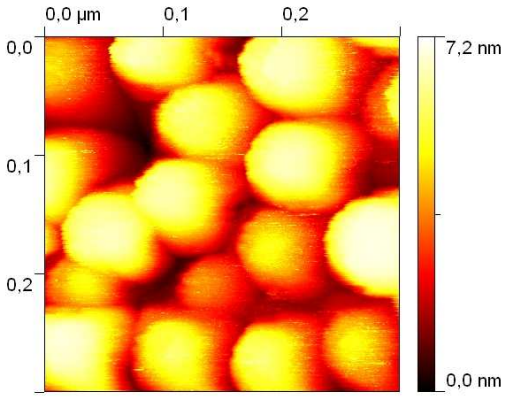

(b) Topography [nm]: 40 kOe

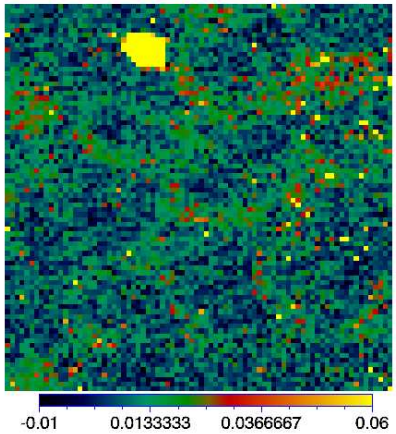

(c) dI/dU [nA/V]: zero field

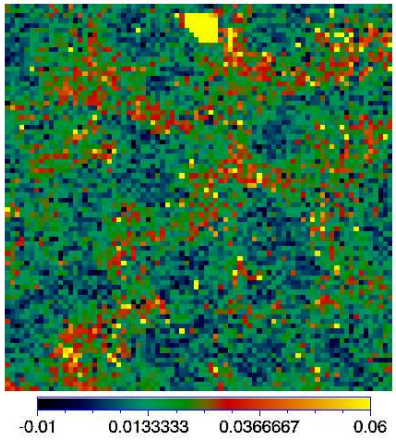

(d) dI/dU [nA/V]: 40 kOe

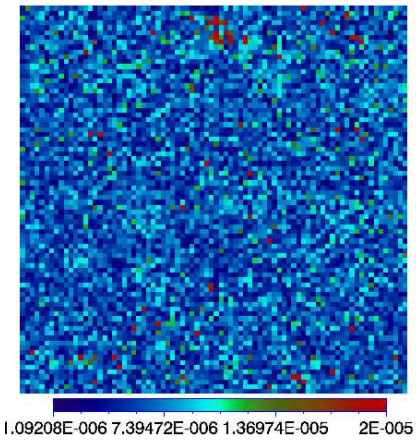

(e) no field

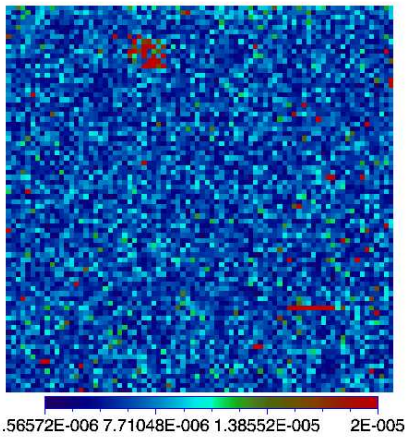

(f) field

Figure 7.6.: STM (a,b) and STS (c,d) images for the 3D sample at 221 K without field and with 40 kOe applied. The picture size is $300 \times 300\,\mathrm{nm}^2$. χ^2 maps (e,f) for (c,d) respectively.

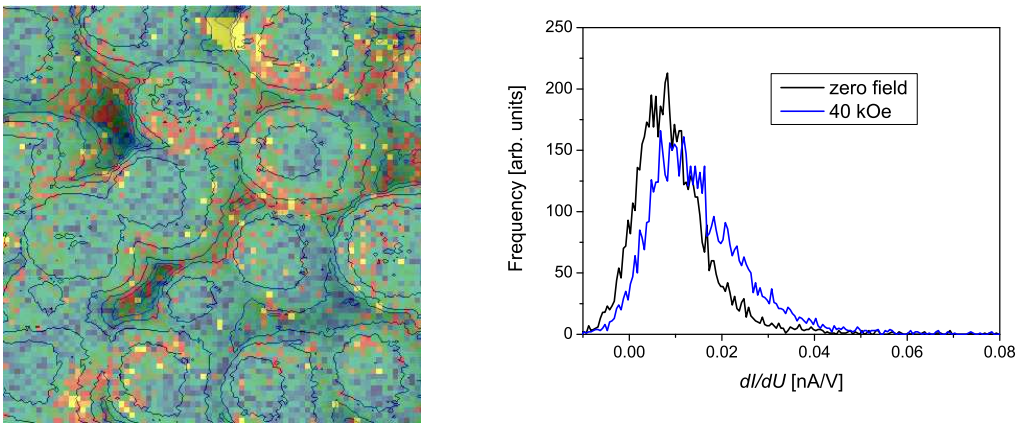

(a) comparison **(b)** histogram

Figure 7.7.: Direct comparison of tunneling conductivity and topography (a) for Fig. 7.6 (b,d) and histograms (b) for Fig. 7.6 (measurement B).

tunneling conductivity parts can be found (for example on the grain on the lower left). In summary the spectroscopy is not totally coupled to the topography.

The tunneling conductivities for the respective pictures are summarized in the histograms of Fig. 7.7 (b). They show an overall increase of the tunneling conductivity, the histogram is shifted towards higher values for the measurement with magnetic field. The mean – or better peak – conductivity σ_p (fitted as the peak discussed before) rises from 15.7(1) pA/V to 19.0(1) pA/V, that is, a net change of 38 % is observed. This change is calculated according to the magnetoresistance as

$$\Delta\sigma_p = 1 - \frac{\sigma(H=0)}{\sigma(H = x\,kOe)} \tag{7.2}$$

with x as the applied magnetic field, which was 40 kOe in this case.

The next measurements were done at a higher temperature of $T = 258$ K. In this case it was possible to keep the measurement stable enough for a comparison of the field effects with different feedback sets, that is for 0.4 V/0.2 nA (measurement C) and 0.7 V/0.4 nA (measurement D) respectively. The topography which is shown only for 0.4/0.2 nA is the same for all four measurements and a drift is negligible. In addition the grains show a more cubic like structure (Fig, 7.8 a,b), more pronounced probably due to a sharper tip. The size of the pictures is $200 \times 200\,\mathrm{nm}^2$.

Again similar features in the tunneling conductivities (Fig. 7.8 c-d) can be observed as in the measurement demonstrated last. The tunneling conductivity maps also include high and low conducting regions and the impression about their shapes remains the same independent of the magnetic field (compare left to right map) or the feedback set (compare upper to lower tunneling conductivity maps). For the feedback of 0.7 V/0.4 nA the values of the tunneling conductivities are shifted towards lower values, they depend not only on the bias but also on the tip-sample distance, which is different for different feedback sets.

In Fig. 7.9 (a) the overlapping of the topography with some added contour lines

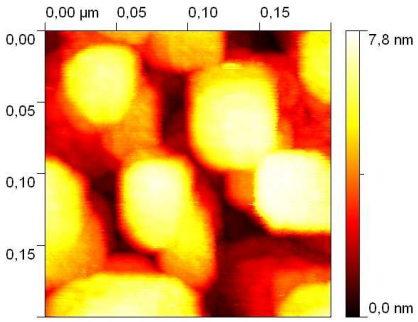

(a) Topography [nm]: zero field

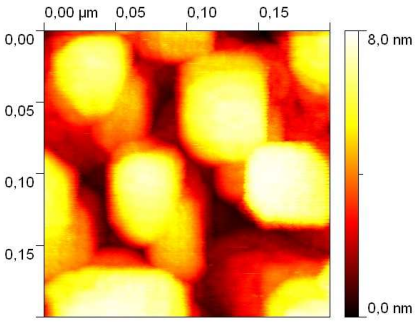

(b) Topography [nm]: 40 KOe

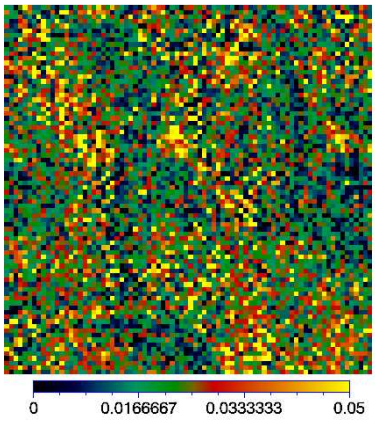

(c) dI/dU [nA/V]: zero field

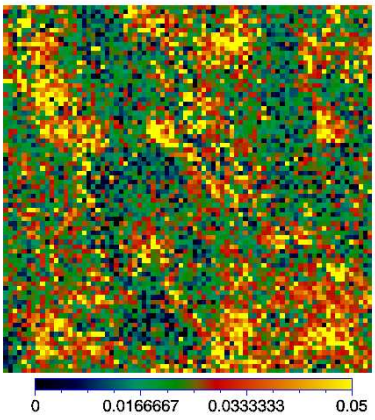

(d) dI/dU [nA/V]: 40 KOe

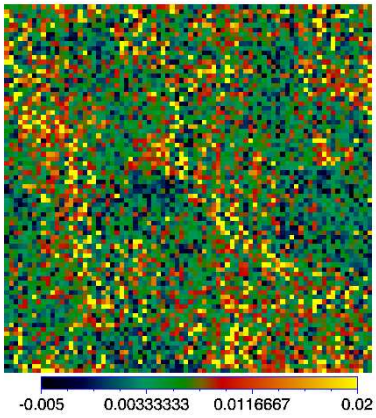

(e) dI/dU [nA/V]: zero field

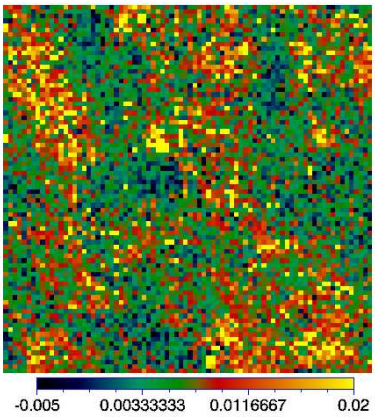

(f) dI/dU [nA/V]: 40 KOe

Figure 7.8.: STM (a,b) and STS (c-f) images for the 3D sample at 258 K without field and with 40 kOe applied. The picture size is $200 \times 200\,\mathrm{nm}^2$. The conductivity maps were taken for a feedback of 0.4 V/0.2 nA (c,d) (measurement C) and 0.7 V/0.4 nA (e,f) (measurement D). (The respective units for the color bars are given in brackets.)

in Fig. 7.8 (b) and the tunneling conductivity map of Fig. 7.8 (d) is shown. Here the correlation of the grain structure and the different regions of the conductivity map is less pronounced than in the last measurement discussed. Some parts with higher tunneling conductivity are located along the grain edges (see for example the upper left part of the map). Only small deviations of the feedback current exist at the grain edges, but do not affect the main part of the STS map. Again the tunneling conductivity increases with an applied magnetic field of 40 kOe.

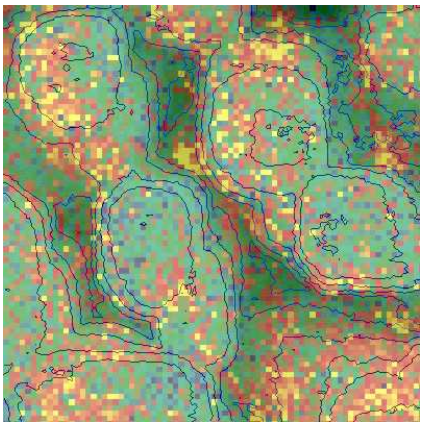

Figure 7.9.: A comparison of the tunneling conductivity map in Fig. 7.8 (d) with its respective topography.

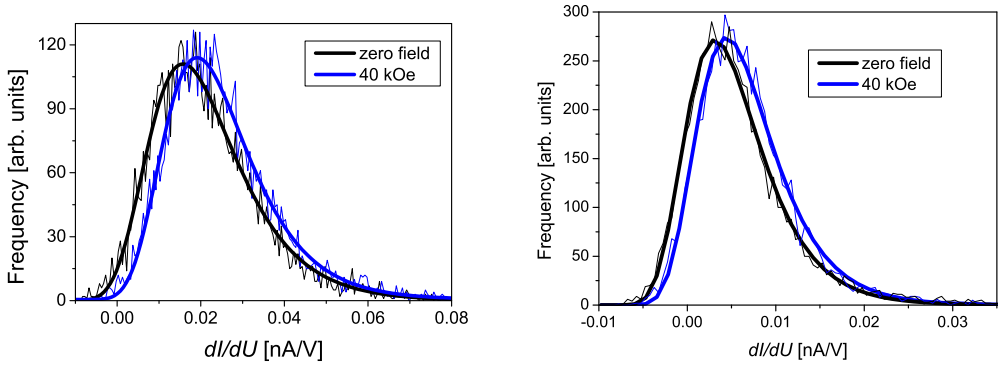

(a) Histogram (0.4 V/0.2 nA) **(b)** Histogram (0.7 V/0.4 nA)

Figure 7.10.: Histograms of Fig. 7.8 for two different tunneling feedback parameters 0.4 V/0.2 nA (a) (measurement C) and 0.7 V/0.2 nA (b) (measurement D) in comparison without and with a magnetic field. (The bold lines correspond to the fitting functions.)

The histograms in Fig. 7.10 reflect the observations from the tunneling conductivity maps. The magnetic field shifts the tunneling conductivity peak towards higher values for both feedback sets. The peaks are mainly shifted and do not change their shape. For the higher feedback parameters (0.7 V/0.2 nA) this takes

place at lower tunneling conductivity values, while the peak width is reduced.

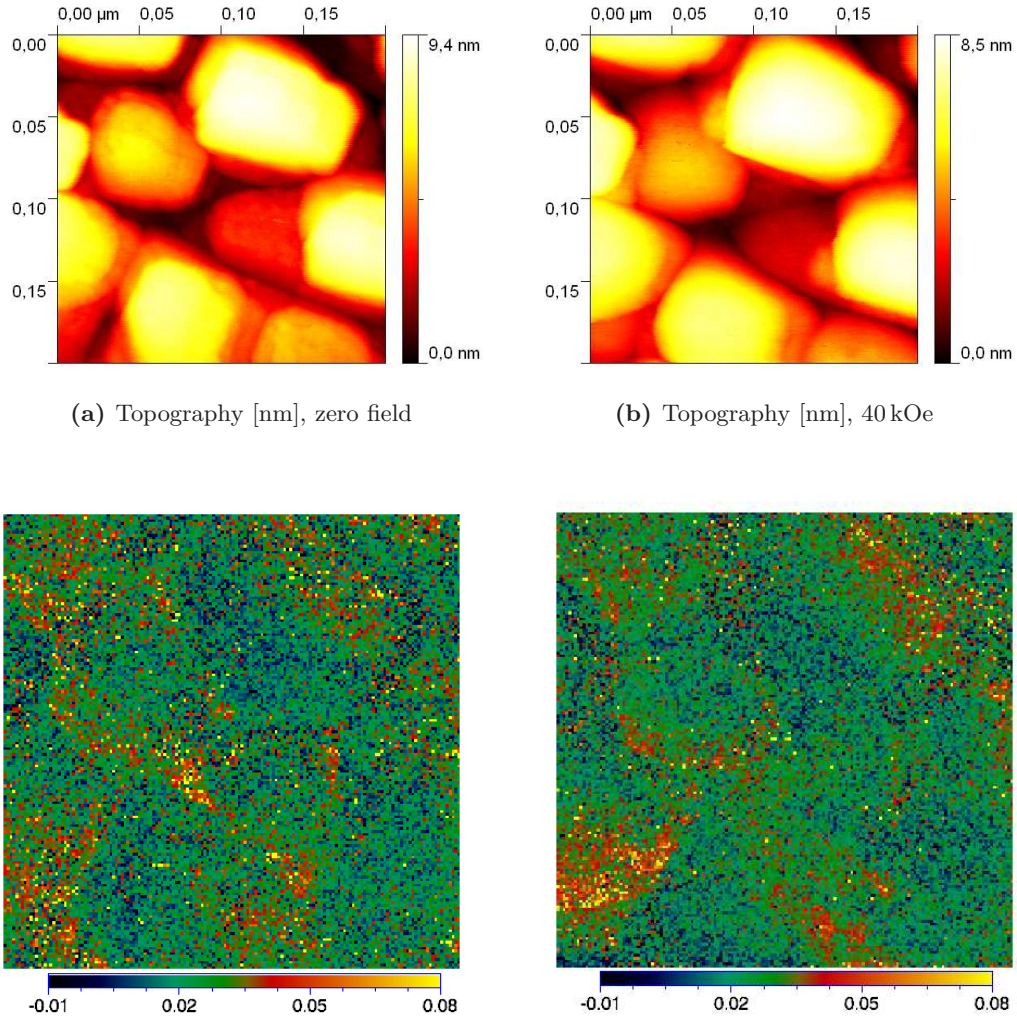

(a) Topography [nm], zero field

(b) Topography [nm], 40 kOe

(c) dI/dU [nA/V], zero field

(d) dI/dU [nA/V], 40 kOe

Figure 7.11.: Topography (a,b) and STS images (c,d) for the 3D sample at 258 K (measurement E). The picture size is $200 \times 200\,\mathrm{nm}^2$. The conductivity maps were taken for a feedback of 0.4 V/0.2 nA for a grid of 160×160 points. (The respective units for the color bars are given in brackets.)

The next measurement was done at the same temperature and feedback set as for Fig. 7.8 (c,d). In this case another spot on the sample and 160×160 spectroscopy points were taken. (The image was rotated by 20°.) The drift of the topography is negligible, but the grains are smoothed a little bit in the second measurement (Fig. 7.11 b) and the tip seemed to be slightly less sharp. Like in the pictures before the grains show a cube like shape with the grain edges oriented roughly parallel with respect to the substrate edges and therefore the cubic orientation of the MgO.

The tunneling conductivity maps in Fig. 7.11 (c,d) appear to be a little bit dif-

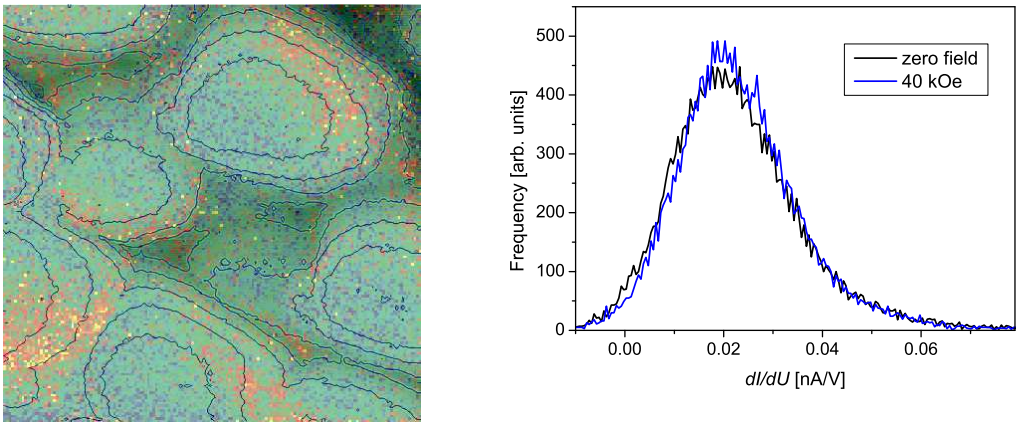

(a) Comparison **(b)** Histogram

Figure 7.12.: Comparison of the topography with the tunneling conductivity map (a) and the histograms of Fig. 7.11 c,d.

ferent than for the case demonstrated before. The different regions are comparable with the previous results, there are sample spots with higher and lower tunneling conductivity (blue, green and red areas). Also sometimes the grain edges show a lower conductivity as can be seen in Fig. 7.12 (a) on the upper grain, for example, where a gray scale topography with contour lines again was overlaid by its respective tunneling conductivity map. In this case Fig. 7.11 (b) and d were taken as demonstration. In contrast to the expectations the changes with the applied magnetic field appear less pronounced and except for the lower left region of Fig. 7.11 (c) the field differences seem to be negligible.

This picture is supported by the histogram, seen in Fig. 7.12 (b). The peak in blue for the histogram of the tunneling conductivities taken within a magnetic field of again 40 kOe is not shifted in comparison with that for the zero-field measurement. Both curves lie more or less on top of each other. The net change resulting from the fit is only 5%, which might be due to a tip change from on to the next measurement, indicated by the somewhat smoothened grain edges.

7.1.4. Summary

The results presented so far are summarized in Fig. 7.13 and in Tab. 7.1. In the bar plot the changes $\Delta\sigma_p$ are shown together with the temperatures and feedback sets. The error bars resulting from the peak fits are not shown. The capital letters refer to the respective measurements. The largest changes with respect to the magnetic field is observed for the measurement at 211 K with $\Delta\sigma_p = 38\%$. The other measurements show a less pronounced change, depending on the feedback set and the sample spot, which was measured. In Tab. 7.1 the mean tunneling conductivities, their changes in a magnetic field and the feedback sets are summarized in numbers.

The magnetic field effects are largest for the measurement at 220 K, while the effect at the higher temperature ($T = 258$ K) is smaller, shown by a comparison of

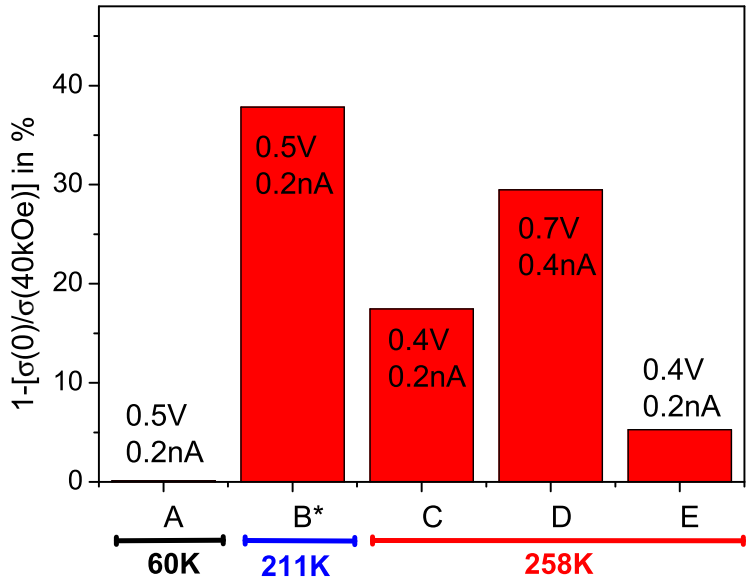

Figure 7.13.: Overview of the different field changes for the 3D sample at two different temperatures. Within the bars the feedback parameters are given.

Measurement	$\sigma_p(0)$[pA/V]	$\sigma_p(40\,\mathrm{kOe})$[pA/V]	$\Delta\sigma_p$ [%]	feedback set
B*	6.18(7)	9.94(9)	≈ 38	0.5 V/0.2 nA
C	15.75(12)	19.08(11)	≈ 17	0.4 V/0.2 nA
D	3.11(4)	4.41(4)	≈ 29	0.7 V/0.4 nA
E	17.77(1)	18.76(11)	≈ 5	0.4 V/0.4 nA

Table 7.1.: Comparison of the field effects on the tunneling conductivity for the different measurements. The peak conductivities σ_p for the measurements without and with field are given with their net change $\Delta\sigma_p$ due to the magnetic field. For the measurement marked with * the temperature had not reached its final stability.

the measurements with 0.5 V and 0.4 V (measurements B and C). In this case for the measurement at the higher voltage and higher tunneling current the change in $\Delta\sigma_p$ is increased.

7.2. Film with layered growth

7.2.1. Topographic details

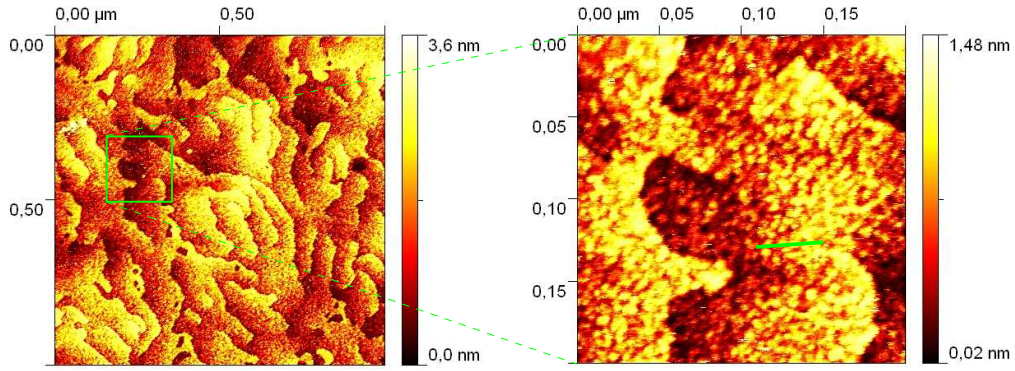

Figure 7.14.: STM images at two different scales to demonstrate the ripple structure on the surface: The green box on the left image indicates the section, which corresponds to the right image. The line on the right image shows the line profile in Fig. 7.15.

The topographies of the samples were already discussed shortly in Chap. 6. The LL samples show a flat terrace structure with a terrace height of a unit cell (see Fig. 6.1 and Fig. 6.2). There is another remarkable observation which should be addressed here. All of the LL samples show a ripple structure on the terraces. The latter appear on every picture and are shown in the two images in Fig. 7.14 for two different scales. The right image of the figure shows a part of the larger image on the left, which is marked by the green box. It was taken separately at a higher resolution. No distinct ordering pattern of these small ripples appears. They rather seem to be quite randomly distributed. To determine the size, that is the lateral corrugation length of these ripples, some line profiles like the example in Fig. 7.15 were analyzed. The diameter of the structures is about 8(1) nm. While the terrace height is one unit cell, the height of the ripples is much more difficult to measure and seems to be about half a unit cell parameter (for the structure of $La_{0.75}Ca_{0.25}MnO_3$ compare Chap. 2).

This structural feature reflects truly the topography. AFM pictures always show the same structure as in Fig. 7.16, which was taken on a similar sample in a small room temperature AFM under ambient conditions. Here the tip was somewhat blunt, but still at some places the ripples can be seen quite well, marked by the green boxes.

7.2.2. Temperature dependence

Similar to the 3D sample also for the LL sample STS-measurements at different temperatures were taken to see if there are any differences in the spectroscopy

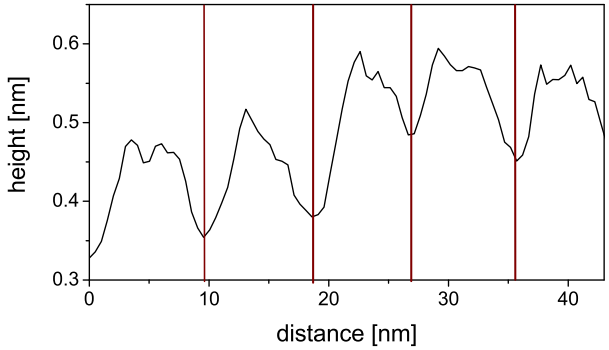

Figure 7.15.: Example for a line profile with some ripples from the left image of Fig. 7.14.

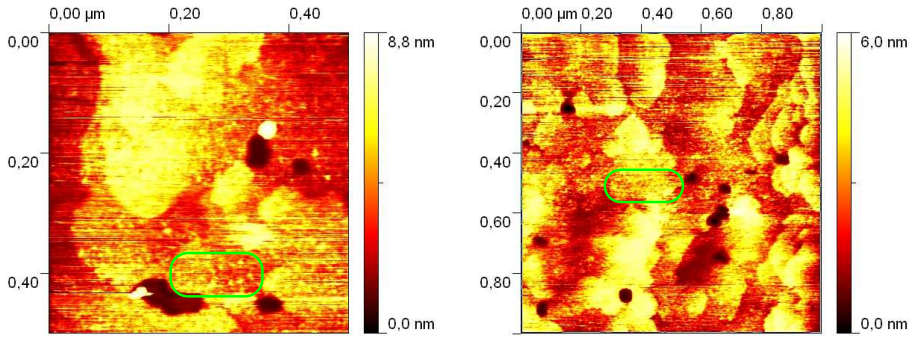

Figure 7.16.: Two AFM pictures on a similar LL sample. Here, also the ripples can be seen, marked by the boxes.

data compared to the 3D films.[10] The STS data were taken at two temperatures, while the first of 150 K is below the MIT and the second one of 216 K is directly on the onset of the transition, compare also with the gray curves Fig. 6.9. The two tunneling conductivity maps are shown in Fig. 7.17 for 150 K (a) and 216 K (b). Related to the temperature change between the measurements the pictures do not show the same area. The lateral distribution of the tunneling conductivities is not homogeneous, but there are spots with lower conductivities and regions with higher conductivities. One can see spots with lower conductivity with a size of 5 nm-15 nm diameter. The regions with higher conductivities seem to be inhomogeneous in shape and size.

The χ^2 values, which are less than 5×10^{-5} are plotted in Fig. 7.17 (c),(d) and do not reflect any features seen in the tunneling conductivities implicating a good reliability of the measurement.

In Fig. 7.18 the histograms for both measurements can be seen with their respective fitting functions. In this case the asymmetry (discussed in Chap. 7.1.1) was not

[10] T. Becker[1] measured the temperature dependence for manganite thin films, but the films used during his study did not show a layer-by-layer growth.

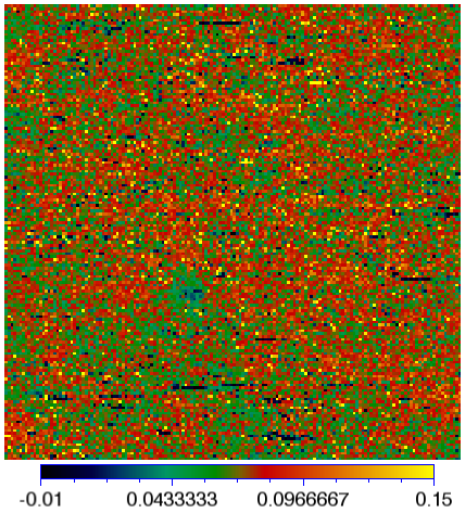

(a) dI/dU [nA/V]: $T = 150\,\mathrm{K}$

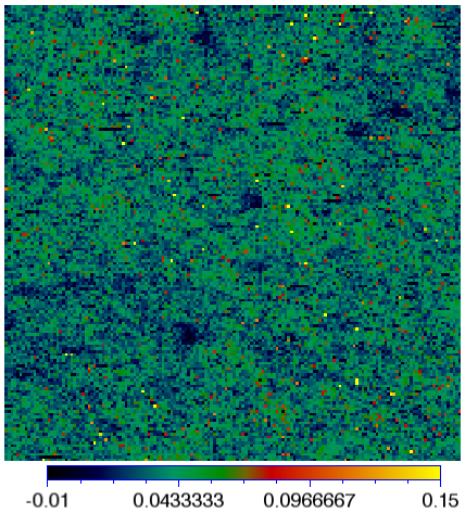

(b) dI/dU [nA/V]: $T = 216\,\mathrm{K}$

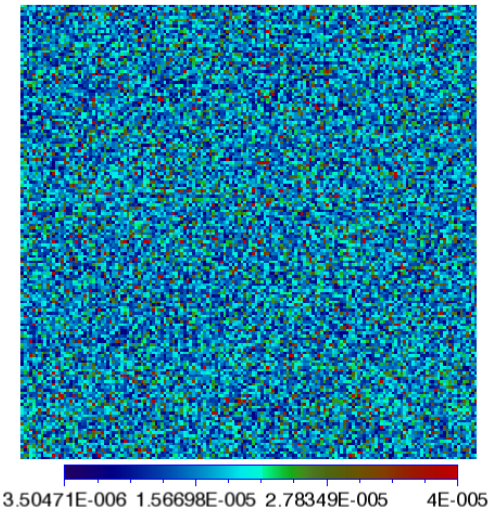

(c) χ^2: $T = 150\,\mathrm{K}$

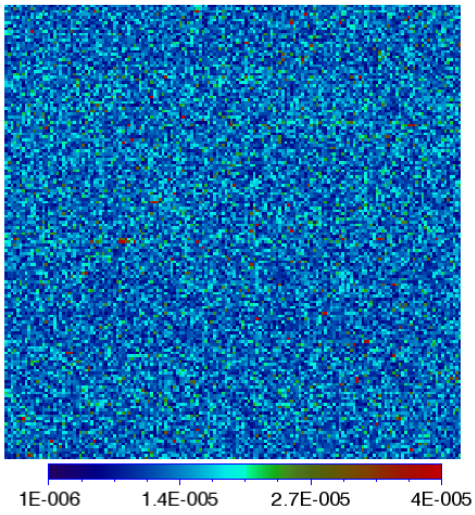

(d) χ^2: $T = 216\,\mathrm{K}$

Figure 7.17.: STS images for the LL sample at 150 K (a) and 216 K (b). The size of the pictures are $150 \times 150\,\mathrm{nm}^2$ (a) and $250 \times 250\,\mathrm{nm}^2$ (b). Both images were taken at 0.5 V and 0.2 nA. Below, the respective χ^2 values are given.

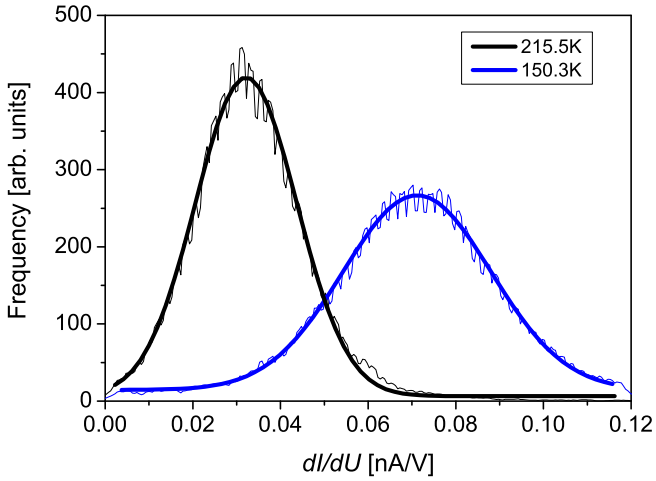

Figure 7.18.: Histograms for STS-maps of Fig. 7.17 to demonstrate the rise in tunneling conductivity for lower temperatures. The thick lines correspond to the fitted Gaussian curves.

observed and a Gaussian fit was taken, which applies for all LL measurements.[11]

The overall tunneling conductivity was determined from the peak values from the Gaussian fits. For the measurement at 150 K the mean tunneling conductivity is hence $\sigma_p = 71.1(6)\,\mathrm{pA/V}$ more than twice as much higher than the tunneling conductivity $\sigma_p = 32.12(4)\,\mathrm{pA/V}$ at 216 K. For the higher tunneling conductivity the histogram peak is also broader (width: $w = 34(17)\,\mathrm{pA/V}$) than for the lower one ($w = 23.1(9)\,\mathrm{pA/V}$). If the width of the Gaussian peaks is normalized to the peak centers, the value for the lower temperature, namely $\frac{w}{\sigma_p}(150\,\mathrm{K}) = 0.48$, is smaller than for the higher temperature with $\frac{w}{\sigma_p}(216\,\mathrm{K}) = 0.71$.

Compared to the 3D sample, the inhomogeneities are less pronounced for the LL sample. At a first glance, in contrast to the 3D samples here the different regions are smaller in size. While for the 3D samples regions about 20 nm-50 nm were observed, in this case the length scales (10 nm-20 nm) are much smaller. These are direct observations from the conductivity maps by the eye. A much more detailed study of length scales via a correlation analysis will be presented in the discussion (Chap. 8).

The difference in the tunneling conductivities in this case is not as large as for the temperature dependent measurements of the 3D sample, since both temperatures are less far apart from each other. Compared to the bulk resistance changes between 150 K and 216 K (Fig. 6.7) the relative change of the tunneling conductivity is a little bit smaller, which also applies for the changes by a magnetic field as described in the following.

[11] Gaussian fit used here: $y = y_0 + \frac{A}{w \cdot \sqrt{\frac{\pi}{2}}} \cdot \exp -\frac{2(x-x_c)^2}{w^2}$, with y_0: baseline offset, w: originally 2σ with $w/2$ as standard deviation, here: ≈ 0.849 of FWHM, x_c: peak center, which corresponds here to the mean tunneling conductivity, called σ_p.

7.2.3. Field dependence

A change of the tunneling conductivities with the temperature was verified in the last part. Now, the field dependent measurements are presented. For the data collection the temperature was kept constant while in between two measurements the magnetic field was changed. Since the largest effects caused by a magnetic field are expected to occur at the MIT (see also Chap. 6, Fig. 6.9), the measurements concentrate on temperatures nearby T_{MI} , that is 258 K and 267 K were chosen for the experiments.

In Fig. 7.19 measurements taken at 258 K are shown. The panels (a) and (b) show the topographies for zero-field and the measurement in a magnetic field. The imaged area did not change while applying the magnetic field of 40 kOe. Therefore, both tunneling spectroscopy maps can be directly compared with each other. In the next row (c,d) the respective tunneling conductivities are shown, taken at a grid of 80×80 points. The data was collected at a bias voltage of 0.5 V and a feedback current of 0.2 nA. Some inhomogeneities can be seen also in these conductivity maps, similar to those shown in Sec. 7.2.2 about the temperature dependency.

Most intriguing is the large color change between the zero-field and the in-field measurement. The overall tunneling conductivity is shifted towards higher values. The worse conducting parts, that is dark blue areas are shifted and do not remain with the same tunneling conductivity. On the tunneling conductivity map for the in-field measurement not very many spots with this color can be found, but the regions with lowest tunneling conductivity show a dark green color. The same accounts for the higher conducting parts, which are shifted with their tunneling conductivity as well. For the measurement in a field much more points with red and yellow color appear. In addition a general lateral growth of the areas with higher tunneling conductivity cannot be found.

In the last row (Fig. 7.19 e,f) the χ^2 values are shown and neither do exceed $3 \cdot 10^{-5}$ nor would give any hints to correlations with the topography. None of the structures in the tunneling conductivity maps corresponds to any topographical features like a terrace step or anything else.

The histograms of the tunneling conductivities are plotted in Fig. 7.20 for the analysis of the mean tunneling conductivities and the distribution of the conductivities. The zero-field and in-field measurements are indicated by the line colors black and red, respectively, while the thick line is the Gaussian fit for the histograms. The mean tunneling conductivities, determined as the peak centers σ_p, change about $\Delta\sigma_p$ =45% from $\sigma_p(0) = 19.26(14)$pA/V to $\sigma_p(40\,\text{kOe}) = 34.88(15)$pA/V while the error was determined from the Gaussian fitting. The specific values are going to be given in summary in Tab. 7.2 at the end of this chapter. To set them into relation with each other again the ratio $\Delta\sigma_p$ from Eq. 7.2 in Sec. 7.1.3 was used.
The width of the peaks increases slightly with the application of the magnetic field from $w = 21.8(4)$ pA/V to $w = 22.3(4)$ pA/V. The latter will be analyzed in more detail and compared with the other measurements at the end of this chapter in the summary.

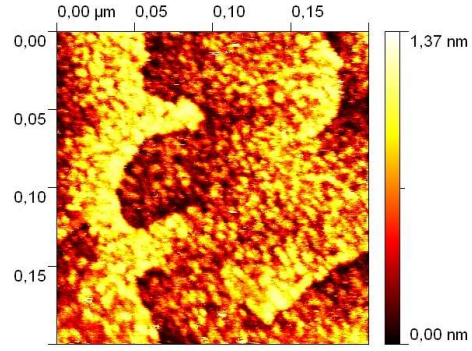

(a) Topography [nm]: $H = 0$

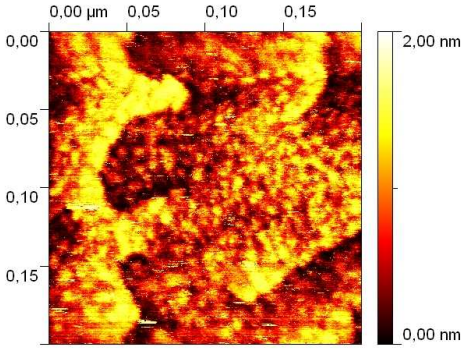

(b) Topography [nm]: $H = 40\,\mathrm{kOe}$

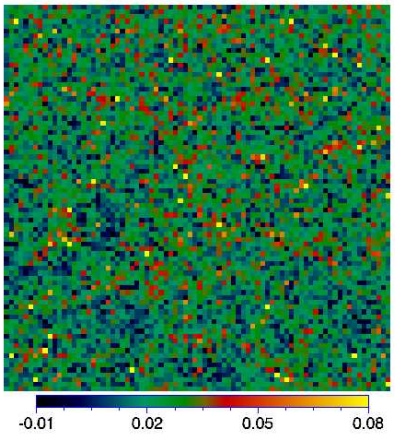

(c) dI/dU [nA/V]: $H = 0$

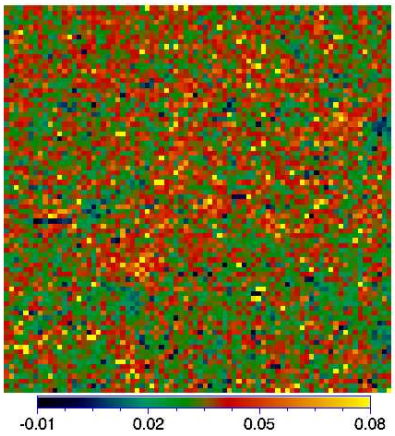

(d) dI/dU [nA/V]: $H = 40\,\mathrm{kOe}$

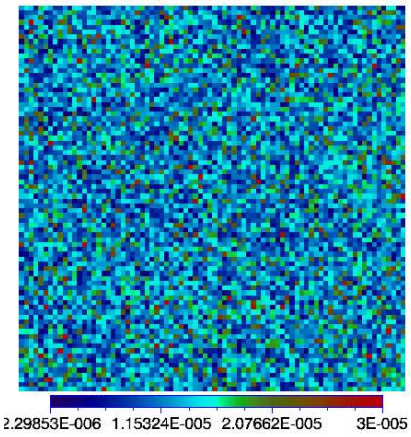

(e) χ^2: $H = 0$

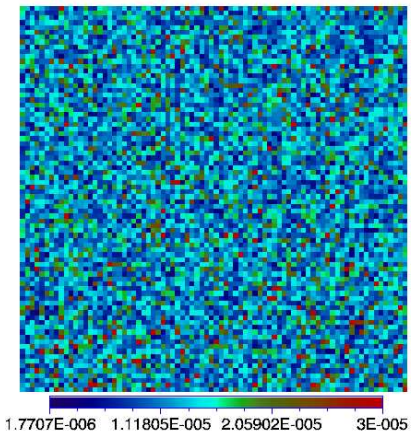

(f) χ^2: $H = 40\,\mathrm{kOe}$

Figure 7.19.: Topographies (a,b), tunneling conductivities (c,d) and χ^2 values (e,f) measured for the LL sample at 258 K without a magnetic field applied (left) and with 40 kOe applied (right). All images show the same area of $200 \times 200\,\mathrm{nm}^2$ and were taken at 0.5 V and 0.2 nA. (Measurement A)

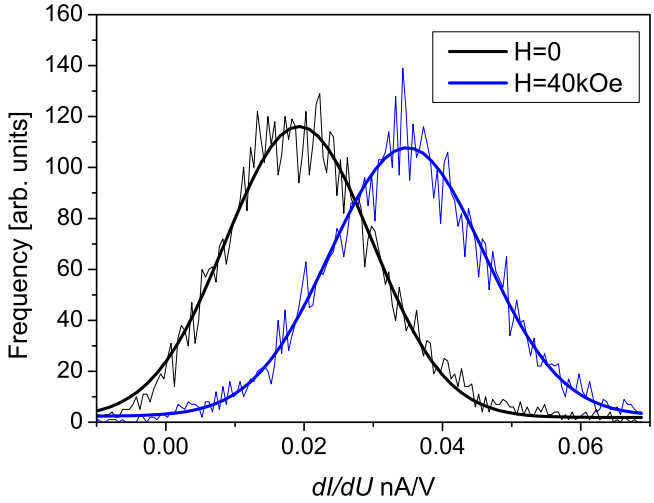

Figure 7.20.: Histograms for STS-maps of Fig. 7.19 (c,d) for the in-field and zero-field measurement. The thick lines correspond to the respective Gaussian curves.

In Fig. 7.22 another example for a measurement at 258 K is presented with a much smaller topographical scale ($150 \times 150\,\mathrm{nm}^2$). The images were taken at 0.7 V and 0.2 nA. Here, the field was first applied and the zero-field measurement was taken afterwords, since the measurements were done in one run with the last measurements. A very small shift of the image to the upper left can be observed, but in principal both topographies (and tunneling conductivity maps) are from the same surface area. The tunneling conductivity maps are shown in Fig. 7.21 (c,d) and again predict a significant change in the tunneling conductivity. The values in Fig. (e,f) are $\chi^2 < 5 \cdot 10^{-5}$ and reflect no topographical features.

For the last two measurements the zero-field and in-field histograms are shown in Fig. 7.22.[12] Here, only the areas of the pictures with a size of $128 \times 128\,\mathrm{nm}^2$, which are found in both measurements, were taken for the determination of the histograms. In other words only the spectroscopy points of exactly the same surface points were taken. The resulting peak change from 10.82(7) pA/V to 15.26(9) pA/V is $\Delta\sigma_p$ =30%, for the complete pictures the result is only slightly different and yields to a net change of $\Delta\sigma_p$ =29%. The latter shows, that a small drift does not significantly affect the results. Since the magnetic field was applied in reverse order in comparison of the measurement described before and again a large change in tunneling conductivity was observed, a change of the tunneling conductivity due to temperature effects can be excluded.

The next measurements taken at 267 K are presented in Fig. 7.23. Again the

[12] The different heights of the peaks arise from the distribution of the values. There is the same number of spectroscopy points for both measurements, but if there is a long tail of high conducting outliers, the height of the mean peak is reduced.

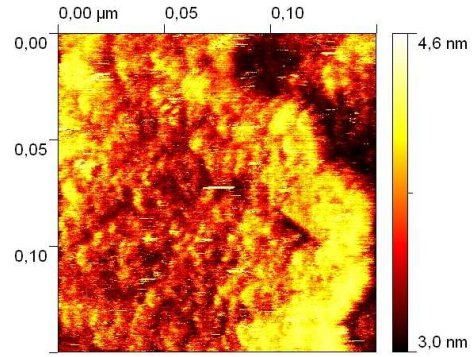

(a) Topography [nm]: $H = 0$

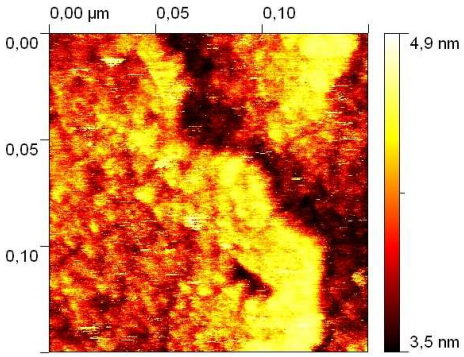

(b) Topography [nm]: $H = 40\,\mathrm{kOe}$

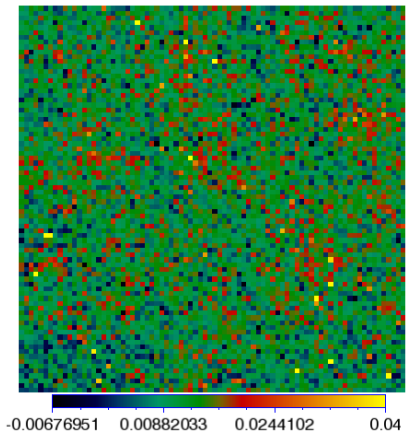

(c) dI/dU [nA/V]: $H = 0$

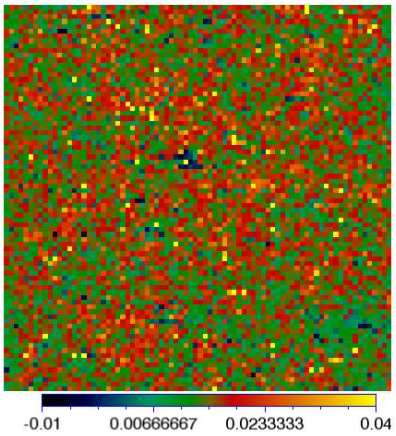

(d) dI/dU [nA/V]: $H = 40\,\mathrm{kOe}$

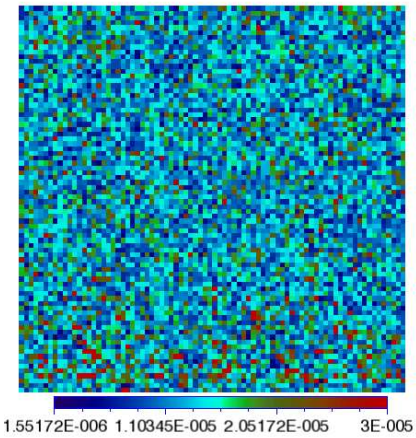

(e) χ^2: $H = 0$

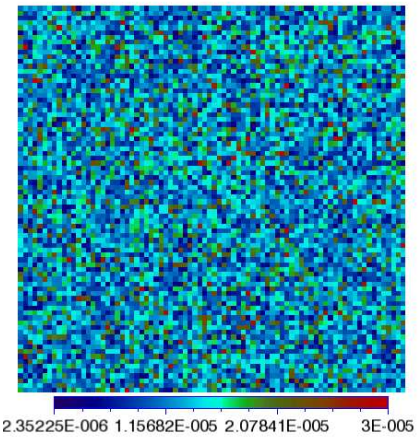

(f) χ^2: $H = 40\,\mathrm{kOe}$

Figure 7.21.: Topographies (a,b), χ^2 values (c,d) and tunneling conductivities (e,f) for the LL sample at 258 K without a magnetic field applied (left) and with 40 kOe applied (right). All images show the same area of $150 \times 150\,\mathrm{nm}^2$ and were taken at 0.5 V and 0.2 nA. (Measurement B).

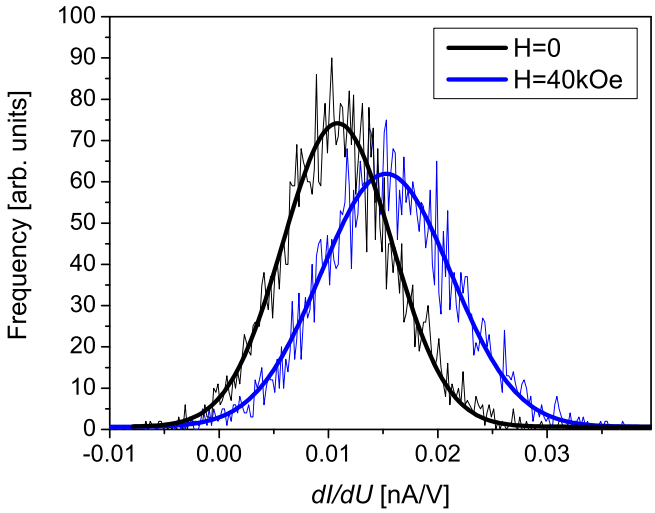

Figure 7.22.: Histograms for STS-maps of Fig. 7.21 for the in-field and zero-field measurement reduced to the matching areas in the topographies.

topographies are shown in the figures (a) and (b). Some terraces and the typical pattern on these terraces can be seen. In this case the spectroscopy was taken at a better resolution than before with a grid of 160×160 points at a feedback set of 0.4 V and 0.25 nA. Hence, the features in the spectroscopy can be seen in more detail compared to the measurements before. In Fig. 7.23 (c) different regions can be seen. The tunneling conductivity map is again inhomogeneous. There are some (partially elongated) areas of higher conductivity and some blue spots with lower conductivity. With a magnetic field applied the shapes of the regions remain the same, but are shifted towards higher conductivity values. Although the fact of an inhomogeneous distribution of tunneling conductivities is evident, it should be noted here, that the division into regions by eye to describe the pictures is done by the color information. The borders of the regions are not as sharp as they might appear due to a color change. In the discussion another way for the description is chosen by a correlation analysis to distinguish the different length scales of the regions. As usual, none of these features is reflected in the χ^2 values, which are $< 3 \cdot 10^{-5}$, shown in Fig. c and d. The histograms of these pictures are shown later in Fig. 7.25 and discussed together with the histograms for the next images.

In Fig. 7.24 a measurement on a scale of $1\,\mu\text{m} \times 1\,\mu\text{m}$ is presented with the topographies shown in a and b. A lot of terraces can be seen with the typical ripple structure. Both pictures are taken at the same spot. The spectroscopy data was taken at 160×160 points at the same feedback as the last measurement, such that the determined values can be directly compared with each other. The tunneling spectroscopy maps look different in the sense that there are less of the distinct small features observable on this scale. On the other hand similarly to the last measure-

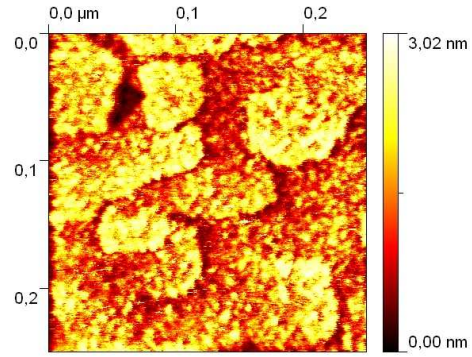

(a) Topography [nm]: $H = 0$

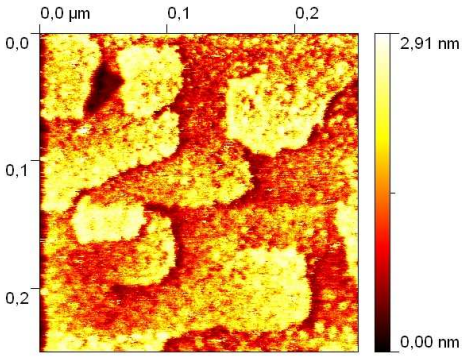

(b) Topography [nm]: $H = 40\,\mathrm{kOe}$

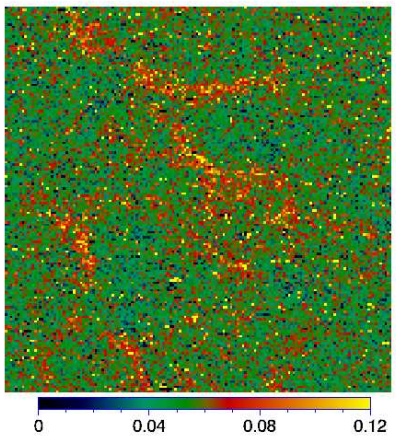

(c) dI/dU [nA/V]: $H = 0$

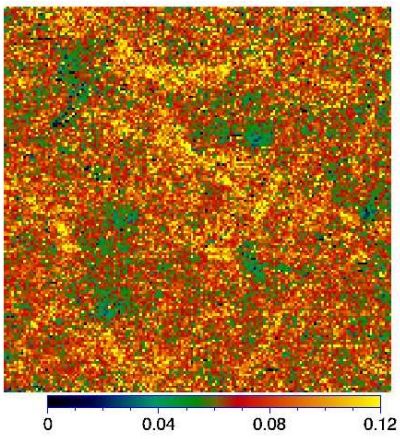

(d) dI/dU [nA/V]: $H = 40\,\mathrm{kOe}$

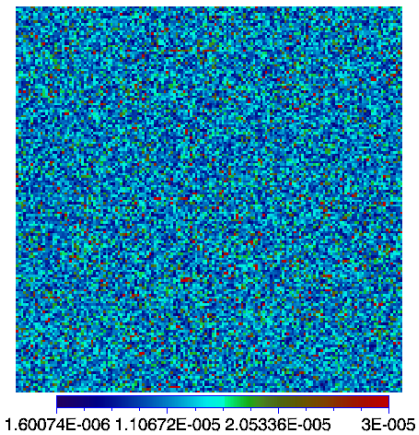

(e) χ^2: $H = 0$

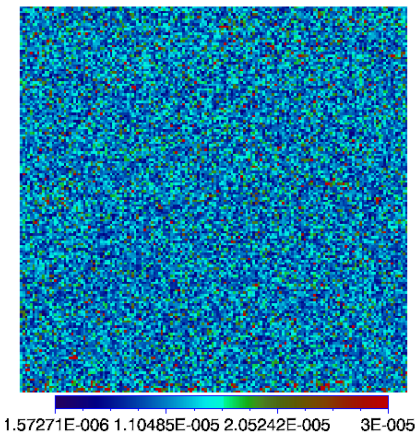

(f) χ^2: $H = 40\,\mathrm{kOe}$

Figure 7.23.: Topographies (a,b), tunneling conductivities (c,d) and χ^2 values (e,f) for the LL sample at 267 K without a magnetic field applied (left) and with 40 kOe applied (right). All images show the same area of $250 \times 250\,\mathrm{nm}^2$ and were taken at 0.4 V and 0.25 nA. (Measurement E.)

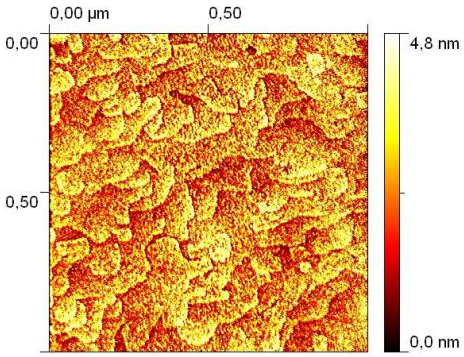

(a) Topography [nm]: $H = 0$

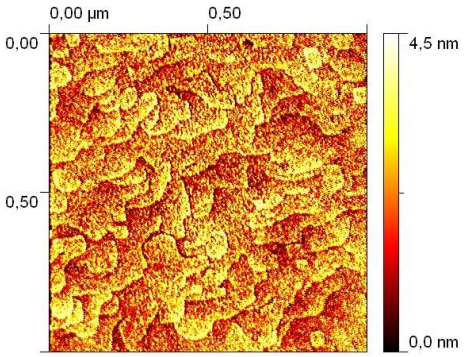

(b) Topography [nm]: $H = 40\,\mathrm{kOe}$

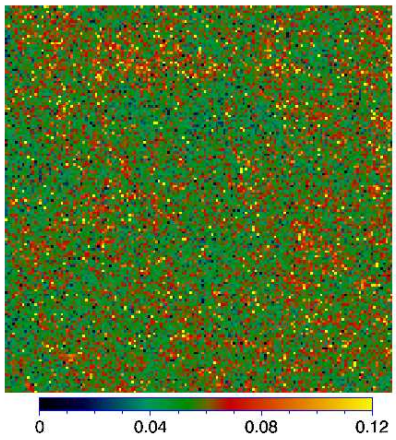

(c) dI/dU [nA/V]: $H = 0$

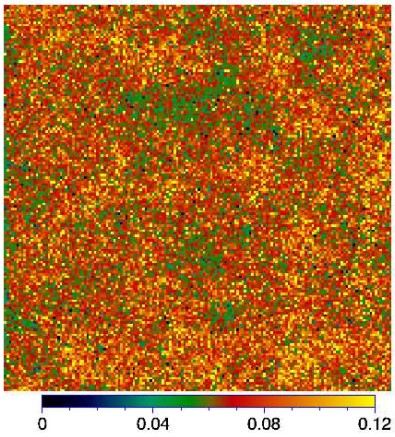

(d) dI/dU [nA/V]: $H = 40\,\mathrm{kOe}$

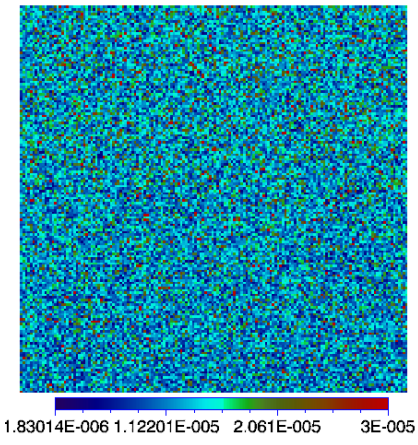

(e) χ^2: $H = 0$

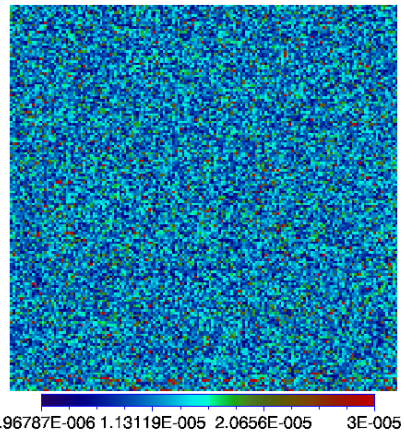

(f) χ^2: $H = 40\,\mathrm{kOe}$

Figure 7.24.: Topographies (a,b), tunneling conductivities (c,d) and χ^2 values (e,f) for the LL sample at 267 K without a magnetic field applied (left) and with 40 kOe applied (right). All images show the same area of $1000 \times 1000\,\mathrm{nm}^2$ and were taken at 0.4 V and 0.25 nA. (Measurement F.)

ment different regions, which are larger, with an extend of 100 nm to 400 nm with lower (blue) and higher (green) conductivity can be seen in Fig. 7.24 (c). These are shifted to higher conductivities, namely towards green and yellow regions in Fig. 7.24 (d) like the shifting seen in all the measurements before. The $\chi^2 < 3 \cdot 10^{-5}$ values again reflect a reliable fit.

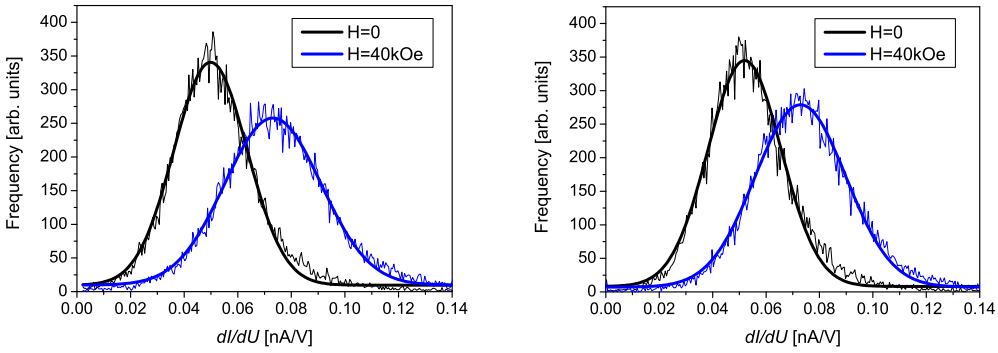

(a) measurement F **(b)** measurement E

Figure 7.25.: Histograms for STS-maps of the last figures (left: from Fig. 7.23 c,d,reduced to the matching parts according to the topographies; right: from Fig. 7.24 c,d).

The respective histograms are given in Fig. 7.25. Again a distinct shift of the histogram peaks takes place upon the application of a magnetic field. The peak is shifted from 49.87(11)pA/V to 73.11(14)pA/V for measurement E and $\Delta\sigma_p$ is 32%. For measurement F they are the same as for the measurement E with nearly the same peak positions of 51.96(12) pA/V and 72.89(13) pA/V. The same is valid for the width of 27.4(3) pA/V for the zero-field measurement and 33.9(3)pA/V for the in-field measurement. The net change is about $\Delta\sigma_p$ =29%.

7.2.4. Voltage dependence

To demonstrate the voltage dependence, for measurement E (shown in Fig. 7.23) a polynomial analysis at different voltages was performed. The voltage dependence is therefore demonstrated for a constant feedback set (bias voltage 0.4 V and feedback current 0.25 nA), since it is not changed in this case. Here the $I(U)$-curves were fitted by polynomials and the respective derivatives $\frac{dI}{dU}|_{U=U_0}$, calculated analytically from these polynomials, are plotted for certain voltages U_0 in Fig. 7.26 again as tunneling conductivity maps. For the highest voltage, namely the feedback voltage $U = 0.4$ V, the tunneling conductivity is highest due to the exponential behavior of the tunneling current. As mentioned in the experimental part the scattering of the tunneling conductivities determined with this method is somewhat higher than for the linear method used so far. It can be observed that there is only a statistical distribution of the tunneling conductivities, but there are no topological features recognizable at the feedback bias $U_0 = 0.4$ V. The same can be observed for 0.3 V and 0.2 V.

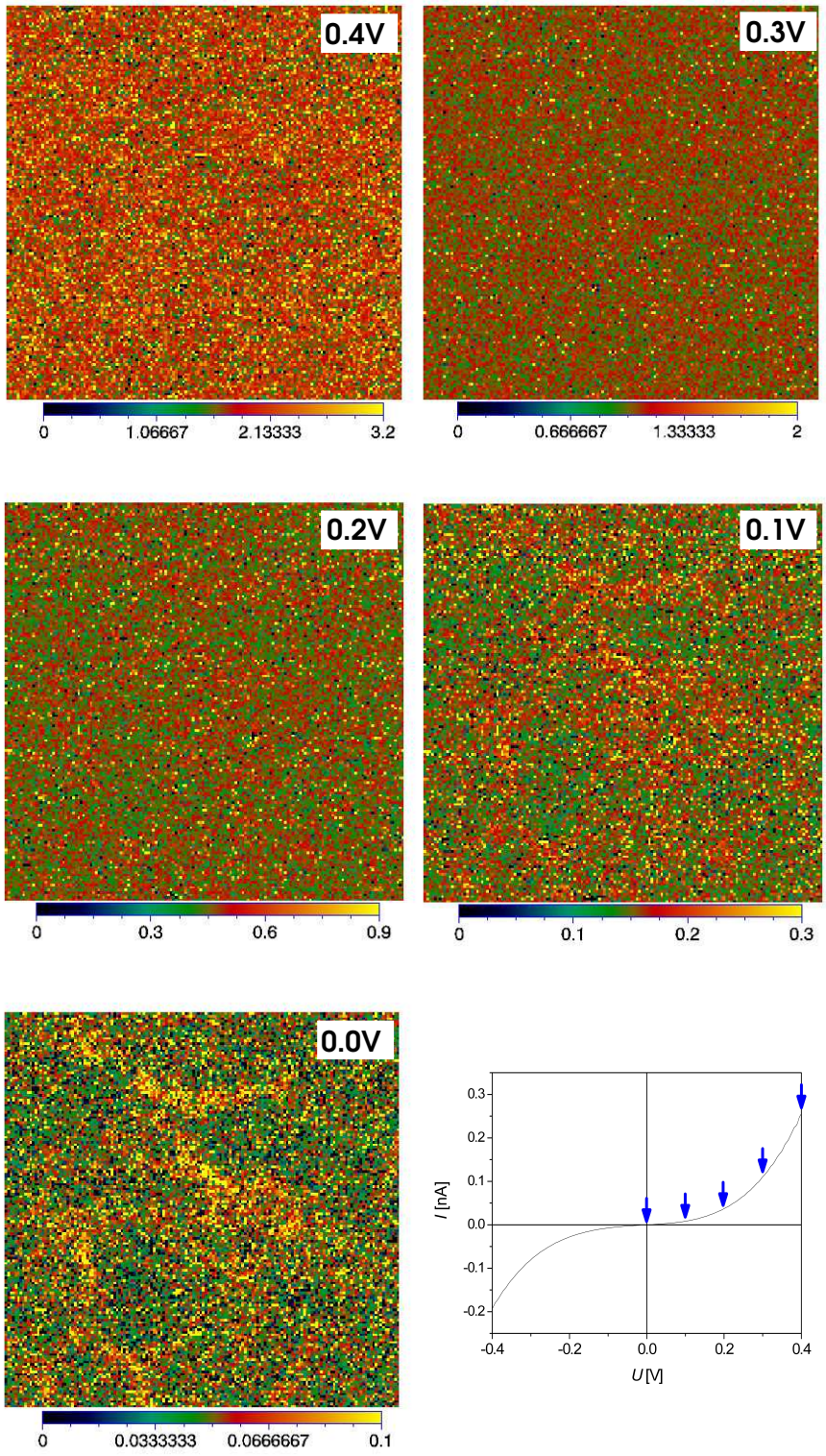

Figure 7.26.: Analysis of tunneling conductivity at different voltages for measurement E (polynomial method was used here). In the lower right part an averaged spectroscopy curve is shown whereat the voltage points U_0 for the calculated derivatives $\frac{dI}{dU}|_{U_0}$ are marked by blue arrows.

In the tunneling conductivity map for 0.1 V some inhomogeneities start to develop. The emerged regions of high and low conducting areas itself do not change their shape with voltage, but they are most pronounced for zero bias. This means that at small energies the effects of the different regions are largest. It should be noted that the picture appears to be qualitatively the same as the one analyzed with the linear method in Fig. 7.23 (f), only a slight offset in the tunneling conductivity could be observed. The latter shows, that the analysis methods show consistent results. In the plotted curve on the lower right the points at which the derivatives were taken are marked by arrows on an averaged spectroscopy curve.

7.2.5. Summary

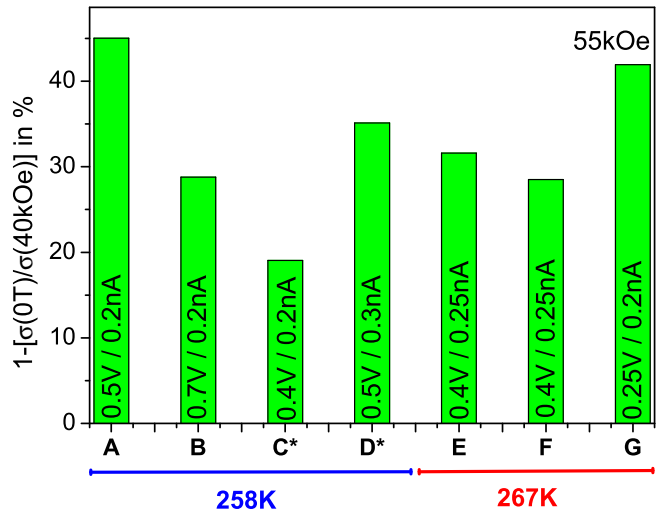

Figure 7.27.: Overview of the different field changes for the LL sample at two different temperatures. Within the bars the feedback parameters are given. The capital letters denote the respective measurements. (Measurements marked with * had a reduced qualitiy of the topography.)

A summary of all field changes is shown in Fig. 7.27 as a bar chart. Each bar represents a single measurement denoted by the capital letters. Those marked with a star showed a topography of reduced quality. For both temperatures the field induced changes are similar in magnitude. Additionally there is no tendency towards larger or smaller changes with respect to the bias applied during the scan. The values for the measurements are again summarized in numbers in Tab. 7.2. The errors given for the mean conductivities σ_p reflects mainly the quality of the Gaussian fitting, since the distribution of the changes $\Delta\sigma_p$ show a larger scattering outside these small errors.

In general also the width of the Gauss peaks increases with increasing tunneling conductivity and therefore increasing field or decreasing temperature. Taking the width as another kind of error bar, it should increase with larger values due to the

No.	Field	σ_p[pA/V]	w[pA/V]	$\frac{w}{\sigma_p}$	$\Delta\sigma_p$ [%]	bias/feedback
A	0	19.26(14)	21.77(36)	1.13	≈ 45	0.5 V/0.2 nA
	40 kOe	34.88(15)	22.31(42)	0.64		
B	0	10.82(7)	9.98(17)	0.92	≈ 30	0.7 V/0.2 nA
	40 kOe	15.26(9)	11.90(23)	0.78		
C*	0	54.1(43)	30.1(14)	0.56	≈ 19	0.4 V/0.2 nA
	40 kOe	66.84(63)	36.0(19)	0.54		
D*	0	32.46(10)	22.50(25)	0.91	≈ 35	0.5 V/0.3 nA
	40 kOe	50.02(14)	21.94(35)	0.44		
E	0	49.87(11)	73.11(14)	0.54	≈ 32	0.4 V/0.25 nA
	40 kOe	73.11(14)	35.93(37)	0.49		
F[a]	0	51.96(12)	27.40(28)	0.52	≈ 30	0.4 V/0.25 nA
	40 kOe	72.89(13)	33.98(33)	0.47		
G[b]	0	65.83(53)	45.3(12)	0.69	≈ 42	0.25 V/0.2 nA
	40 kOe	11.34(8)	67.4(22)	0.59		

Table 7.2.: Comparison of the magnetic field effects on the tunneling conductivity for the different measurements. The mean conductivities σ_p for the zero-field and in-field measurements are given with their net change $\Delta\sigma_p$ due to the magnetic field. Additionally the width w of the Gaussian peaks of the histograms are given for zero-field and in-field measurements together with the respective ratios $\frac{w}{\sigma_p}(H)$. (Measurements marked with * had a reduced qualitiy of the topography.)

[a] Determined for matching parts, see text above.
[b] Determined for matching parts. Applied field was 55 kOe.

increase of noise caused by the electronics and tunnel junction. On the other hand, a comparison of the ratios between the peak centers σ_p and the peak width w_p for each measurement yields the relative widths as a kind of normalization of the widths with respect to the mean tunneling conductivities. The obtained numbers given in Tab. 7.2, do not give quantitative hints, but there is the tendency towards decreasing ratios $\frac{w}{\sigma_p}$ for increased σ_p.

Bibliography

[1] T. Becker. *Untersuchung der elektrischen Phasenseparation in dünnen Manganatschichten mit Rastersondenspektroskopie.* Doktorarbeit, Universität Göttingen, 2004.

8. Discussion

The influence of a magnetic field onto the electronic properties is of fundamental interest to understand the peculiar interplay of spin, charge and lattice degrees of freedom in manganites. The main task of this work was to determine the effect of an external magnetic field on the local electronic properties by scanning tunneling spectroscopy. This was done in the vicinity of the bulk metal-insulator transition, where the effects are expected to be large. Two different samples, a 3D and LL film, with a different microscopic texture due to their growth modes were used for the measurements. The results of the measurements were presented in Chap. 7. They are now compared and analyzed within the context of the general theories and model calculations given therein.

Since the crystallographic structure largely influences the electronic and magnetic properties, it is first investigated and compared with films reported in the literature. The importance of the microscopic structure is related to (A-site) ordering tendencies. The influence on the electronic and magnetic properties is then discussed in a wider context of structural influences. Later on in this context a connection can be drawn between the structure and the differences of the bulk properties of the films. Since the STS was the main part of this work, a detailed analysis is demonstrated using some of the data sets of Chap. 7 and the results are compared with each other. The properties of manganites are commonly ascribed to a phase separation, which will be discussed for the results obtained. Finally, the work will be compared with STM and STS measurements reported by other groups.

8.1. The samples and their structural differences

8.1.1. Thin film growth

The thin film growth and properties depend largely on the substrate chosen. On $SrTiO_3$ (STO), manganite films with $x \approx 0.3$ (Ca,Sr doping) possess usually a large misfit stress [28, 8] and with increasing film thickness the growth mode changes from layer-by-layer to a grain like growth, depending also on the miscut angle of the substrates [30]. On $LaAlO_3$ (LAO) the misfit is much larger such that the films do not adopt the in-plane lattice constant due to misfit dislocations at the interface and the stress is relaxed, but only a grain like growth was reported for such films [24, 25, 4]. Exceptionally for $NdGaO_3$ (NGO) a nearly stress-free growth for LCMO films was reported [28] and also a layer-by-layer growth was observed [17].

MgO is a less common choice as substrate for manganites like LCMO, but it turned out to be a good decision to obtain stress-free films. The 3D growth reported

for a large lattice mismatch, as mentioned above, cannot be generalized here and at least does not account for the MgO substrates, as demonstrated by the layer-by-layer (LL) growth. Here the films have practically the same thickness and they were deposited on substrates of the same series, but they show a different microstructure. The growth rate (see App. A) has obviously a large influence on the growth mode. In contrast to the LL sample, the 3D sample was deposited much faster, resulting in a three dimensional growth mode. It can be concluded that the diffusion times were much smaller and seemingly the growth did not correspond to a fully equilibrium condition.

It was already known from previous results that the films can be grown in a lattice matched manner on MgO substrates. This was confirmed by in-plane texture X-ray measurements on the (220) reflex of LCMO [20]. As was shown in Fig. 6.5 for the LL film, misfit dislocations occur in the $La_{0.75}Ca_{0.25}MnO_3$ -film directly at the interface to the substrate and therefore only 2-3 monolayers are epitaxially strained. Upon those the film growth is stress free, which is confirmed by the lattice parameters given in Tab. 6.1. The advantage of this kind of strain relaxation is the exclusion of remaining stress in the films in contrast to totally strained films, grown on STO [8]. For a 3D film no HRTEM picture exists of the film - substrate interface, but it can be expected that also for this film such dislocations exist, since the lattice parameter is very similar and the film does not appear to be fully strained. On the other hand, some growth spirals within the grains can be seen, as indicated in Chap. 6.2, which means that a possible locally remaining strain due to the larger deposition speed, is released by a somewhat different mechanism via screw dislocations in growth spirals[1].

Although the in-plane lattice parameters are very similar (Tab. 6.1), the films developed a different crystal structure, namely the orthorhombic (P_{nma}) structure, typical of LCMO, is found for the 3D film and a pseudo-cubic or rhombohedral ($R\bar{3}c$) structure is found for the LL film, as shown in Chap. 6.2, Fig. 6.6. This is a quite remarkable result, since normally only the lattice parameters change for different substrates or deposition conditions, but generally the film structure retains the same geometry. The origin for this observation is given in the next section.

8.1.2. Ordering tendencies

In the theory (Chap. 2) it was already mentioned that ordering of the ions or orbitals is expected to influence the properties of the manganites. From the discussion of the growth mode above, it can be concluded that not the macroscopic stress, which is negligible here, but also the local ordering within the sample plays an important role. The reasons for this suspicion will be discussed in the following in terms of the structural ordering with respect to the properties of the samples. At first, the ordering tendency is manifested by a particular LL film (called by LL-O in the

[1] A pure columnar growth, like it was observed in LSMO/MgO composite films on Al_3O_3 [10], was not observed in such a pronounced way in previous studies of LCMO on MgO [20]. (The behavior of the resistivity as a function of temperature would be different at low temperatures, if there were badly connected grains.)

following), which shows an A-site ordering (Fig. 8.1), that is, the La and Ca ions are found on well defined lattice sites forming two sublattices [21]. Although such a strict ordering was not seen for the LL film used for the STS measurements of this work, the tendency to a more ordered structure is evident by the morphology and the crystal structure.

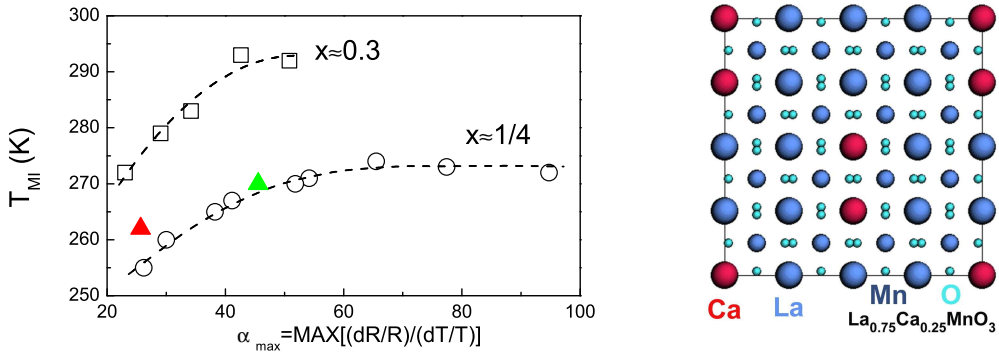

(a) Comparison transition **(b)** A-site order

Figure 8.1.: (a): Transition temperature T_{MI} versus sharpness of transition in comparison with different samples. The 3D and LL samples used here are marked by the red and green triangle, respectively. The LL-O film is represented by the point nearby $\alpha_{max} = 100$. (b): Schematic representation of A-site ordering in LL-O film in the $a-b$-plane as a projection along the $[001]_c$ direction.

Another indication for these ordering tendencies are the bulk electronic and magnetic properties. In Chap. 2 the importance of the structure and lattice distortions for the electronic and magnetic properties were discussed in terms of the influence of the Mn-O-Mn bonds and their bond angles on the exchange mechanisms. From this point of view a change of the properties can be expected for these films with their different structural characteristics. It is indeed the case that the magnetic and electronic transitions differ with respect to their parameters for both samples (shown in Chap. 6): The transition temperature, that is T_{MI} and T_C, are smaller for the 3D film, while for the LL film the values are the highest reported for $La_{0.75}Ca_{0.25}MnO_3$ thin films. Additionally the sharpness of the transition α_{max} (see p. 71) has been mentioned in Chap. 6.3. It rises with the ordering tendency, which is demonstrated in Fig. 8.1, in which different films of the series were compared. The graph shows T_{MI} as a function of α_{max}, whereat a second series of $La_{1-x}Ca_xMnO_3$ films with $x = 0.3$ is added. The latter shows the same tendency as the $La_{0.75}Ca_{0.25}MnO_3$ films. The 3D film used within this work is marked by a red and the LL by a green triangle, respectively. The A-site ordered LL-O film corresponds to the outermost point on the right nearby $\alpha_{max} \cong 100$. Remarkably the sharpness of the transition increases with increasing T_{MI} up to a certain value, where the transition temperatures seem to saturate. In other words here the T_{MI} is given by the composition and its most ordered structure and can be shifted towards

lower temperatures by disorder, which also broadens the transition.

The resistivity for the 3D sample is also higher than for the LL film, but only below the MIT. Above the MIT the resistivities are nearly equal, which does not necessarily contradict the results about ordering, since above T_{MI} a thermally activated transport is expected and therefore the role of the structural ordering is less important, as the transport mechanism is different. The LL-O film fits into this considerations, since its resistivity lies slightly below the one of the LL film here [21].

Evenly the ferro/paramagnetic transition fits into this picture. From the theories (Chap. 2) a direct coupling of the magnetic ordering to the electronic properties is indisputable. There are a lot of hints from experiments, which underline these models (although it never could be proved by a direct measurement). The temperature of the magnetic transition was shown in Fig. 6.8 and the critical temperature T_C is about the same for the LL film and the 3D film, but the sharpness of the transition is broader for the 3D film, like the sharpness of the MIT.

All these differences in the sample properties due to the structural characteristics are an indication for a different degree of A-site ordering. The first peculiarity is the saturation of T_{MI} at a value of about 270 K. This seems to be the maximum, which can be reached for the given doping, $x = 0.25$, and can be associated with the "ideal" case for $La_{0.75}Ca_{0.25}MnO_3$. Ideal means that the structural ordering leads to a perfect arrangement of Mn-O-Mn bonds, such that the electronic properties are optimized. The A-site ordering in the LL-O films additionally supports an ideal regular pattern within the sample with its superstructure and four times larger unit cell.

The orthorhombic structure breaks the cubic symmetry, which changes the Mn-O bond angles slightly compared to the cubic structure. An absolute equivalence of the Mn-O bonds is no more possible. The 3D sample shows a different morphology and it cannot be excluded that locally the sample is strained, although the macroscopic lattice parameter does not support a strained sample. For LCMO/STO films it was for example found that the centers of the islands are unstrained, while the edges are strained regions [4]. Local strain effects (extending over a few lattice sites) would not be expected under a A-site ordering, since the ions with slightly different radii (Chap. 2.3) are distributed in a regular pattern. But for a random distribution of the A-site ions different distortions of the local lattice are expected. In other words, the electronic properties, expressed by the mobility of the charge carriers, are coupled to the structure and therefore are determined by the latter, as demonstrated here.

Another issue, which provides further evidence for a scaling of the sharpness of the transition with the microscopic order within the films, is the structural transition observed by Radaelli [23], compare Chap. 2.3. The group examined the change of the Mn-O bond lengths and angles together with the Jahn-Teller distortions. Consequently there must be a connection with the structures observed and the shifted and broadened MIT of the 3D films. For a quantitative discussion highly resolved temperature dependent neutron scattering experiments would be necessary, but here some qualitative arguments can be highlighted.

The ordering, structure and sharpness of the transition seem to be related to

each other and two attempts of an explanation will be given now. In the rhombohedral structure, which here is associated with a higher chemical ordering, all Mn-O bond lengths are the same, since octahedral distortions are missing. Across the transition, the changes of the bond angles might cost less effort if the structure is more symmetric, which in this sense is the case for the rhombohedral structure, all Mn-O-Mn bond angles and lengths are equal, compared to the orthorhombic structure (see structural description on p. 9 and Fig. 2.4). Therefore the transition can take place within a smaller temperature region and appears to be much sharper. Due to the remaining Jahn-Teller distortions in the orthorhombic 3D films the structural rearrangement is more complicated and restricted. The mean bond lengths and angles could then be expected to remain larger (smaller) than for the other phase. Therefore the bandwidth, which is dependent on these bond lengths (angles), would remain smaller in accordance to a higher resistivity. The LL-O film with its commensurate superstructure would also fit into this picture. Due to the ordering the undisturbed system is expected to change in a cooperative manner (probably slightly comparable to a martensitic transition).

Another possibility is a distribution of different local strain fields and/or local compositions coming along with the disorder. It is known that strain, caused here by disorder on a microscopic scale, can lead to a decrease in the transition temperature, and therefore locally different transition temperatures can occur. Then the different regions within the film undergo the MIT at slightly different temperatures and the transition appears to be broadened compared to an ideally ordered sample. Concurrently the mean transition temperature also can be reduced. Again the bandwidth would be reduced for the disordered cases, since the bond lengths and octahedral distortions, which are caused by the disorder and a random distribution of ionic radii, remain in the sample.

8.2. Spectroscopy

8.2.1. Magnetic effects on the local tunneling conductance

In Chap. 7 the main results were shown for the 3D and LL samples. The $I(U)$ curves were analyzed using the fitting procedures in Sec. 5.3 and Fig. 5.12. Now, the spectroscopy curves will be analyzed and discussed in detail with respect to the regions of different tunneling conductivity and the influence of a magnetic field. The 3D and LL sample will be compared with each other, but the emphasis lies more on the LL measurements.

It should be mentioned that for magnetic fields of 40 kOe the sample magnetization is expected to be saturated as confirmed by the hysteresis curves taken near the metal-insulator transition displayed in Fig. 6.8. Although there is no saturation reached for the MR in the lower panel of Fig. 6.9, most of the changes due to a magnetic field are already reached at 40 kOe as can be seen by the much smaller slope for that region compared to the steep decrease for fields ≤ 20 kOe. Maybe due to the small energies of magnetic fields a real saturation in resistivity might never be reached. This is a general observation for manganites. In addition for 40 kOe also the magnetization at the surface is expected to be at least close to saturation

and effects caused by the shape anisotropy of thin films (e.g. about 10 kOe for Fe films) do not play a role here.

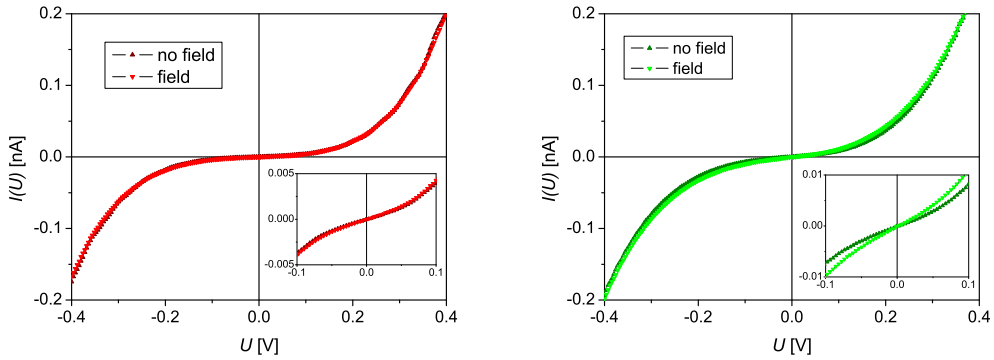

(a) 3D **(b)** LL

Figure 8.2.: Spectroscopy curves for a measurement without field and the respective measurement with a magnetic field applied; averaged over a whole STS image for a 3D (a) sample at 258 K [measurement C, Fig. 7.8] and LL (b) sample at 267 K [measurement E, Fig. 7.23]. The insets show the $I(U)$ curves around zero bias.

In Fig. 8.2 two examples for spectroscopy $I(U)$ curves averaged over an entire STS image are shown for a 3D and LL sample. Both are compared with the respective measurements with an applied magnetic field. At a first glance it can be seen, that the curves[2] for the 3D sample (Fig. 8.2 (a)) are flattened around zero bias compared to those for the LL sample. Secondly the field difference for low voltages $-0.1 < U < 0.1$ V is more pronounced for the LL sample, as can be seen in the insets of the pictures.

The 3D sample shows a smaller tunneling conductivity than the LL sample; this is reflected in the slope of the spectroscopy curves, which have the typical shape attributed to semi-metals. A smaller conductivity can be interpreted in the sense of a less itinerant electron gas in the sample. The flatter the curve and the greater the deviations from a 3rd order polynomial, the larger is the tendency to an insulating behavior, which can go as far as leading to a gap, like in typical semiconductors. Due to the small bias, the tunneling matrix elements are assumed to be constant. A "real" insulating gap with $dI/dU = 0$ at and around 0 V was never seen for these samples, like it was for example the case on $Pr_{0.7}Ca_{0.3}MnO_3$ with the microscope used in this thesis or $Bi_{0.24}Ca_{0.76}MnO_3$ in [26]. The same observations were made in [33, 18]; the literature is discussed in Chap. 8.4.

The curves in Fig. 8.2 also have been analyzed by a linear fit for the zero bias regions, similar to the automatic fitting routine used in the analysis of the individual spectroscopy curves. For the LL sample the tunneling conductivity determined from these averaged curves changes from $< \sigma >= 55.5(5)$ pA/V for the zero-field $I(U)$

[2] The $I(U)$ curves were shifted along the ordinate to run through exactly zero. A small constant offset is caused by the preamplifier and the filter.

curve to $< \sigma(40\,\mathrm{kOe}) >= 79.1(5)\,\mathrm{pA/V}$ for the field curve, while for the 3D sample a much smaller change from $< \sigma >= 24.2(2)\,\mathrm{pA/V}$ to $< \sigma(40\,\mathrm{kOe}) >= 26.9(2)\,\mathrm{pA/V}$ can be determined. The values for the LL sample are similar to those obtained from the histogram peak positions (see Tab.7.2, p. 105) within the statistical error of the linear regression. This underlines the quality and consistency of the computer based analysis of the measurements. Those from the 3D sample are also similar to the histogram peak positions in Tab.7.1, p. 90, but a little bit larger. A clear rise of the slope for the in-field measurement of the LL sample can be seen ($\Delta_\sigma \approx 30\,\%$), but the effect is considerably smaller for the 3D sample ($\Delta_\sigma \approx 10\,\%$). It should be repeated that the rise of the tunneling conductivity of the 3D sample due to an external magnetic field is quite small (compare Tab. 7.1) compared to the width of the histogram peaks shown in the last chapter (e.g. Fig. 7.10). The absolute shift $\sigma_p(H) - \sigma_p(0) = 3.33\,\mathrm{pA/V}$ for the 3D sample (measurement C, p. 87) compared to the width of the histogram for zero field $w(0) = 10.45\,\mathrm{pA/V}$ is very small $[\sigma_p(H) - \sigma_p(0)]/w(0) \simeq 0.32$. Therefore differences for the spectroscopy curves caused by the magnetic field are hardly visible, although the bulk MR is as large as for the LL sample as shown in Fig. 6.9. In the case of the LL sample a change of the slope around zero bias can be already seen in the inset of Fig. 8.2 (b). Here the absolute shift $\sigma_p(H) - \sigma_p(0) = 23.24\,\mathrm{pA/V}$ (measurement E, p. 102) compared to the width of the histogram for zero field $w(0) = 27.35\,\mathrm{pA/V}$ is much more pronounced $[\sigma_p(H) - \sigma_p(0)]/w(0) \simeq 0.85$. The same observations apply for the other measurements of the 3D and the LL sample, not shown.

Compared to the width of the distribution of the tunneling conductivities the changes in tunneling conductivity caused by the magnetic field are much more pronounced for the LL film than for the 3D film. In other words, the shift of the tunneling conductivity with an applied magnetic field are much better resolved for an LL film than for a 3D film.

In the following the local spectroscopy is analyzed in more detail with respect to the different regions of tunneling conductivity for the LL film. In Fig. 8.3 four different spectroscopy curves are compared with each other. The spectroscopy data of parts with lower (black and blue curves) and higher (red and orange curves) tunneling conductivity were averaged over the regions marked by the black and white boxes in Fig. 8.3 (a,b), respectively. The same regions were selected from Measurement E without a field applied (black and red) and with a field applied (blue and orange). From the $I(U)$-curves the differences in tunneling conductivity can be seen for higher and lower conducting regions. The black and blue curves have both smaller tunneling conductivities than the red and orange curves. With the application of a magnetic field, both conductivities are shifted by nearly the same value.[3] (This is consistent with the fact, that the histograms (Fig. 7.25 (a), p. 102) for the measurements with and without field overlap.) This can be seen even

[3] The small effects might be caused by some contaminations on the surface due to the ex-situ preparation, but this is not very likely. Some hints of carbon were found in an XPS measurement and in [32], but the authors talk about less than a monolayer. If a surface preparation would help is not clear, one try by sputtering and heating in air with an LL film of a newer series did not result in reliable measurements. There are recent temperature dependent STS measurements from another group, which confirm these measurements [18].

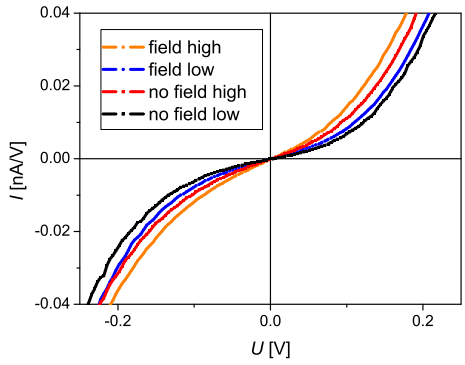

(a) $I(U)$

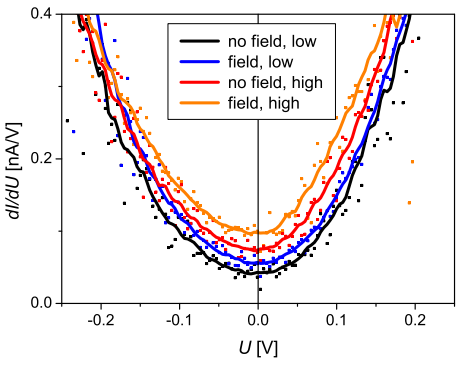

(b) dI/dU

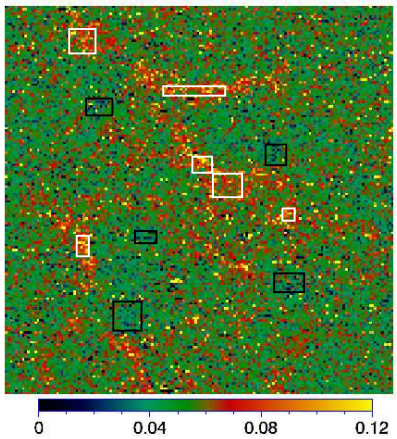

(c) non-field

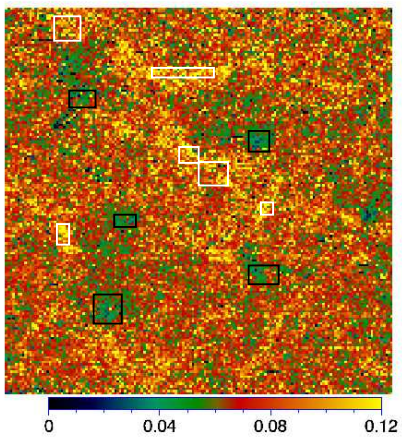

(d) field

Figure 8.3.: Spectroscopy curves (a) and their derivatives (b) averaged over different regions of the zero-field (c) and measurement with field (d) of Measurement E in Fig. 7.23 at $T = 267$ K. White boxes denote average regions for parts with highest conductivity (red and orange lines) and black boxes for parts with lowest conductivity (black and blue lines).

better for the derivatives dI/dU of the curves given in Fig. 8.3 (b).[4] Remarkably none of the curves shows a gap and the changes appear to be gradual. The latter means that the changes within the conductivities of the different regions and with respect to the magnetic field are all in the same magnitude and no severe jumps can be found. The latter is very important, since a growth of one region on the cost of the other cannot be confirmed. Rather all parts show an increase in conductivity, which is also reflected by the optical impression of the changing colors.

[4] It is visible that the tunneling conductivity of the high conducting parts undergoes a larger increase than the low conducting parts, which is comparable to the broadening of the histogram for the measurement with an applied magnetic field.

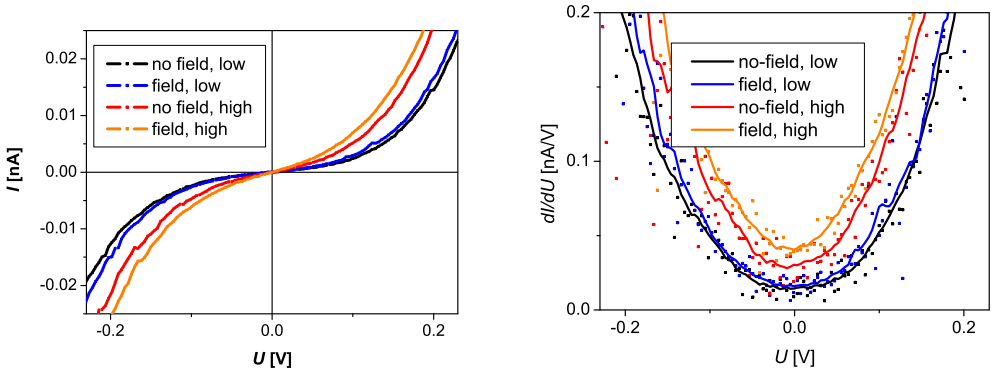

(a) $I(U)$ **(b)** dI/dU

Figure 8.4.: Derivatives of spectroscopy curves averaged over different regions of the measurements without and with a magnetic field applied for Measurement C (Fig. 7.8) at $T = 258\,\mathrm{K}$, analyzed similar as in Fig. 8.3.

The picture for the 3D film is similar, as can be seen in Fig. 8.4. The derivatives, dI/dU, also do not become zero and all parts (high and low conducting regions) change their conductivity. Remarkably, here the difference between the high and low conducting parts are somewhat more pronounced than for the LL-film and the low conducting parts seem to show smaller field induced changes.

As it was shown in the Chap. 3, near the Fermi level the DOS is approximately proportional to the derivative $(dI/dU)_{U\to 0}$. Considering the points at zero bias $(dI/dU)_{U=0}$, in all cases the DOS at the Fermi level interestingly seems to be changed by the magnetic field. The DOS is never vanishing and is increased by the application of a magnetic field.[5] The increase depends a little bit on the regions, but these differences become less pronounced for the LL film. Again the ordering tendency plays a role in this case, which is not very astonishing, since the bandwidth depends on the bond angles and distortions, as discussed in the last section.

8.2.2. Additional remarks about the spectroscopic data

In general there exists a slight asymmetry between the positively and negatively biased sides in the spectroscopic curves. Additionally a very small shift of the minimum of the dI/dU curves towards negative voltages can be identified. Therefore the asymmetry might originate partially in the different workfunctions of tip and sample [34]. At negative bias the tip structure dominates and since the DOS of the PtIr is not exactly constant or symmetric, it also influences the shape of the curve [5] and can cause an additional gradual slope. Unfortunately it is difficult to tell if the s-, p- or d-states of the tip dominate in the measurements, since although the

[5] On the other hand it should be noted, that instead using the term DOS one could state that the itinerancy of the conduction electrons is enhanced due to the magnetic field, which influences the double exchange mechanism.

states from the d-orbitals should contribute most (and are most asymmetric), their decay is very sharp [11]. Also it is difficult to distinguish between the tip states and sample states in this case, as no distinct structures can be found in the dI/dU curves. An asymmetry in otherwise unstructured curves has also been observed by for instance Mitra et al. [17] on similar samples, who ascribe the asymmetry to somewhat different distributions of DOS for filled and unfilled states, which is another possibility. Charging effects or large space charge regions are not very likely in this case and would rather be expected on the highly insulating manganites.

Pickett et al. have performed a calculation of the DOS for $La_{0.75}Ca_{0.25}MnO_3$ [22], which does not show any distinct structures at $\pm 0.5\,\mathrm{eV}$ with respect to the Fermi edge. The same result is confirmed by a photoemission spectroscopy measurement [15].[6] But interestingly Pickett et al. used also a superstructure for their calculation and proposed a dependence of the DOS, particularly for the minority states, on the disorder. Unfortunately no predictions concerning the temperature evolution or magnetic field induced changes of the DOS have been made.

8.3. Phase separation

The term *phase separation* means the existence and interplay of two competing phases in the vicinity of a first order phase transition. Several computing models of the metal-insulator transition in manganites are based on phase separation to explain the CMR effect and are confirmed by some experiments. The two competing phases are mostly ascribed to a ferromagnetic metallic and antiferromagnetic/charge ordered insulating phase. The universality of phase separation for all manganite compounds is still under debate, since most of the models consider only small band width manganites, like $(La_{1-y}Pr_y)_{5/8}Ca_{3/8}MnO_3$ (LPCMO), which show a charge-ordered state at low temperatures.

In the last section the effects of magnetic fields on the tunneling spectroscopy curves were discussed in detail by means of some examples. At first it was shown that there are gradual changes in the tunneling conductivity over the surface areas examined. Secondly, for an applied magnetic field the tunneling conductivity for all of the regions is shifted to a higher value. Third, there is no growth of one kind of regions on the cost of others, that is no nucleation behavior was observed. That there is no sharp boundary between the different regions, in contrast to atomically sharp phase boundaries reported by Renner et al. [26], is another important observation.

Both 3D and LL films show a similar behavior in their electronic and magnetic properties and seem to follow the same mechanism, although some differences, especially in the range of the length scales according to lattice effects, were outlined. Another film, the LL-O film with A-site ordering, showed no phase separation [21, 33] and has the sharpest metal-insulator transition with the highest T_{MI} . Another work[7] provides some hints about the same mechanisms with respect to

[6] For a direct comparison, a deconvolution of the sample and tip DOS and the transmission coefficients is necessary, which is not trivial.

[7] Diploma work in progress, Thomas Mildner.

magnetic fields for the A-site ordered LL-O film. Namely the tunneling conductivity also seems to change all over the scanned area.

In this section the sample properties will be considered in the context of phase separation and different related theories (see Chap. 2.2). The (locally pinned) regions with different conductivities might be called phases.[8] These phases cannot be identified here on the atomic scale, like it was done by Renner et al. [26]. This thesis concentrates on a scale of about 2 – 1000 nm.[9] Below these length scale no direct measurements could be done with the existing setup and no predictions can be made about phase arrangements on a scale close to atomic resolution.

8.3.1. Is there a distinct two phase behavior?

The histograms of the LL samples show a symmetric (Gaussian) distribution, which does not imply any multiphase coexistence. In contrast, the histograms for the 3D sample are somewhat asymmetric. One therefore could assume two Gaussian components as demonstrated in Fig. 8.5. In the figures (a) and (b) the same histograms for a measurement at zero field are shown. There are two different possibilities of fitting the data. At a first glance, the sum of the Gaussian peaks shown in red in graph (a) is a good fit of the data. The peaks of both components are located at centers of $\sigma_{p1} = 13.6(7)\,\mathrm{pA/V}$ and $\sigma_{p2} = 25(6)\,\mathrm{pA/V}$. In graph (b) the data is less well fitted with $\sigma_{p1} = 16.8(8)\,\mathrm{pA/V}$ and $\sigma_{p2} = 37(7)\,\mathrm{pA/V}$. Additionally the data of the measurement within a magnetic field, given by the subfigure (c) was also analyzed this way. Here the peak centers are $\sigma_{p1} = 18.5(6)\,\mathrm{pA/V}$ and $\sigma_{p2} = 31(9)\,\mathrm{pA/V}$.

If now the figures (a) and (c) are compared with each other, both peak centers are shifted to higher conductivities, which is consistent with the results discussed so far. The component of high tunneling conductivity becomes smaller in height – and also the area under the peak is decreased. This observation contradicts a model in which the proportion of high conducting parts increases with the application of a magnetic field. The situation shown in (b) would be even less physically probable, since the peak center for the high conductivity is decreased for the histogram of the measurement in a magnetic field. This analysis together with the analysis of the other measurements did not lead to a well-defined result.

The change over from one phase (region) to the other is demonstrated in Fig. 8.6. Here the data of Measurement E of the 3D film were taken, due to the higher resolution of the spectroscopy grid. Individual spectroscopy curves along a line are shown between a low and high conducting part. The transition is continuous or otherwise two bundles of curves would be expected. If there was an atomically sharp boundary extended over several nanometers between two phases, as seen by Renner et al. [26] on a very small part of the sample, it also would show up as

[8] The term "phase" here does not necessarily mean a phase in a classical thermodynamic description. The lack of a clear definition of the phases in manganites implies the risk of disaccords in the discussion about phases.

[9] The resolution given here does not mean, that with one spectroscopy point a region with diameter of 2 nm is covered, the latter is much smaller, but a definition of a region which is covered by the tunneling current is quite difficult and should not be discussed here. The resolution here is already limited by the number of spectroscopy points per area.

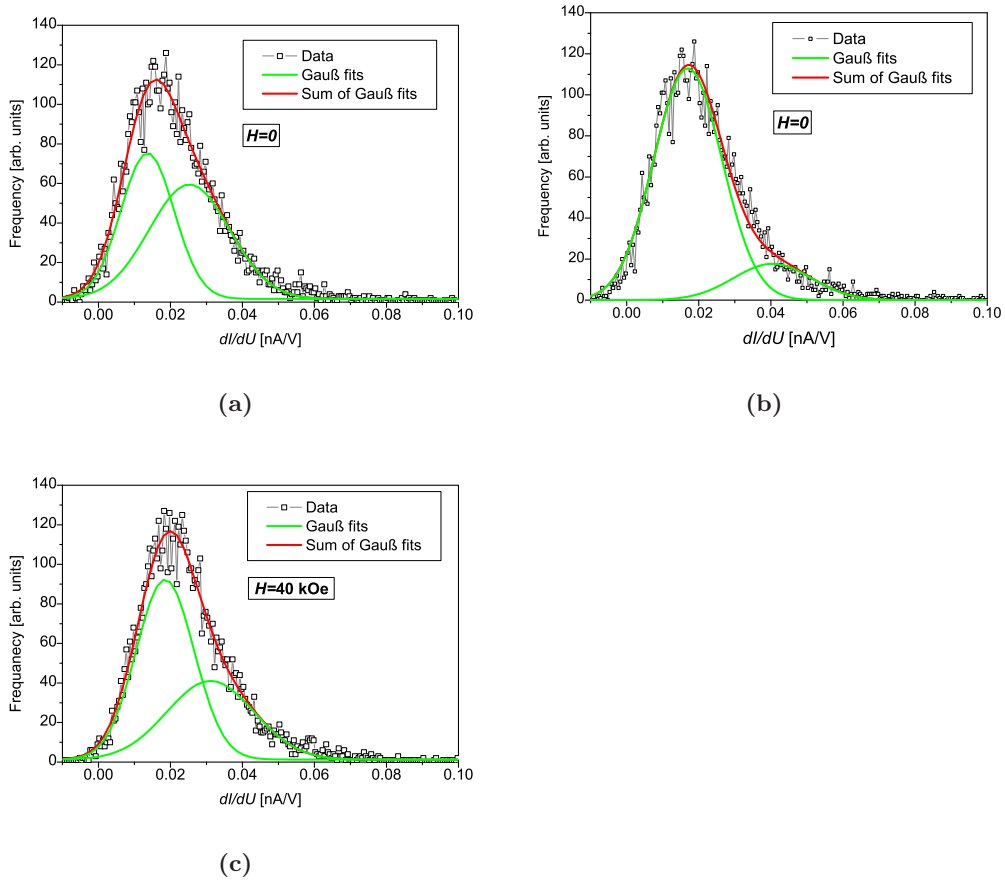

Figure 8.5.: Histograms with double peak Gauss-fits (Measurement C) for zero field (a,b) and an applied field of 40 kOe (c) for the 3D film.

a sharp boundary in our case. The gap of 0.7 eV observed by Renner at room temperature [27] would be also observed here in individual $I(U)$ curves.[10]

Together with the fact that there are no sharp boundaries in between the high and low conducting regions, an interpretation with only two distinct phases has to be taken with care. The observed asymmetry might as well originate from mechanical noise coupling into the measurement or a non-even distribution of different conductivities, which does not mean that there are only two distinct conductivities or phases. In addition, it can be claimed that there is a distribution of different tunneling conductivities (different phases), but a clear distinction between two phases (like an insulating and metallic one) is not possible in this context. The existence of locally strained and/or disordered regions would support this notion, since those also would not change in a discontinuous manner on the above mentioned scale, 2–1000 nm.

[10] The temperature broadening at RT is about $\Delta E \approx 100$ meV, see Chap. 3.

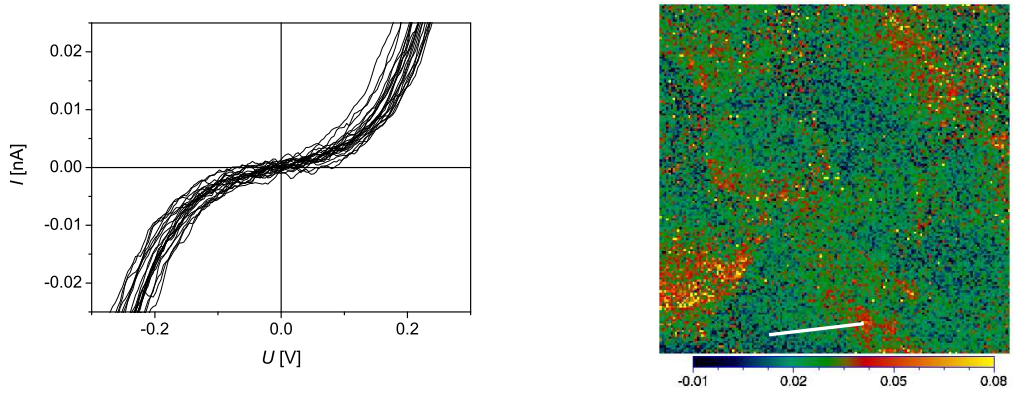

(a) (b)

Figure 8.6.: $I(U)$ spectra (a) shown along one line (b) between a low and high conducting part.

Points of high and low tunneling conductivity can be found to be located closely together on the STS maps. If one would take a very small region on the STS maps as origin and determine the histogram for it, then the width would increase with increasing regions up to a saturation value. This idea leads to the next considerations of correlations.

8.3.2. Size effects and correlations

Regions with different tunneling conductivity have been discussed so far with respect to their electronic properties. The measurements with the different regions were shown in the STS maps in Chap. 7. The 3D samples as well as the LL samples show high and low conducting parts, which have a larger extension for the 3D samples. A detailed analysis of the characteristic length scales involved is based on the correlation analysis introduced in Chap. 5.3.

The normalized radial auto correlation functions $C_{\mathrm{norm}}(r)$ from the topography and spectroscopy for the 3D sample (Measurement C) are shown in Fig. 8.7 (a). The two radial correlation functions for the topographies, taken with and without a field applied, are given by open circles. In all cases the first points were disregarded, since they are influenced by random noise, demonstrated in Fig. 5.14. Both curves have virtually the same shape, which underlines that the topography did not change during the measurements. From the initial decay to $1/e$ the correlation length r_l was determined (see p. 62). The first maximum denotes the mean separation of similar structures, for instance the grains. This maximum occurs at about 75-80 nm, which matches the mean distance between the centers of individual grains in Fig. 7.8 (a,b). The first maximum of the auto correlation function of the spectroscopy maps (given by filled circles) is different from that of the topography, confirming that the regions with different conductivities do not coincide with the topography as was already mentioned in Chap. 7, for example in Fig. 7.9.

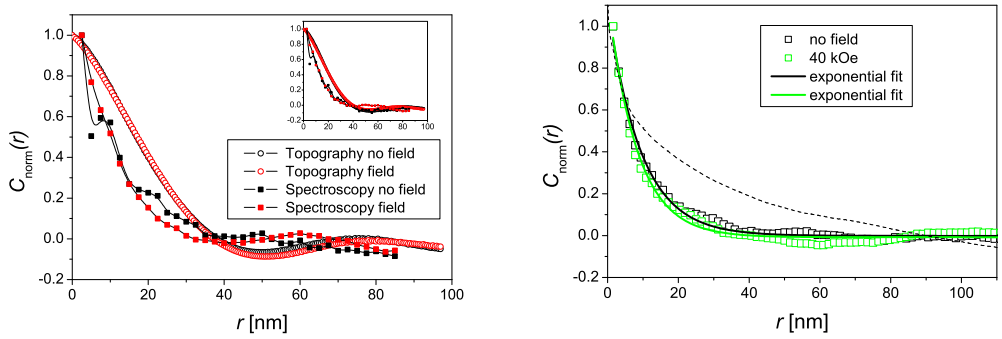

(a) (b)

Figure 8.7.: Examples for normalized radial auto correlation functions $C_{\text{norm}}(r)$ for the topography and spectroscopy maps of Measurement C (inset: Measurement D) of the 3D film (a) and $C_{\text{norm}}(r)$ for the spectroscopy map (measurement E) and the respective exponential fits for the LL film, dashed line indicates $C_{\text{norm}}(r)$ for the topography (b).

In Fig. 8.7 (b) $C_{\text{norm}}(r)$ for the spectroscopy maps of Measurement E of the LL sample are given. Here only one radial correlation function of the topography is indicated by the dashed line, since it is not very meaningful to analyze these curves, because it is impossible to reasonably correlate the terraces at different height z with each other. Additionally the exponential fits to the curves are shown in the same graph. The exponential fits reproduce the experimental curves $C_{\text{norm}}(r)$ quite well. There are some tiny hills seen for the auto correlation data, but they are not very pronounced so that the curves can be considered to be constant behind the steep decay ($r > 40\,\text{nm}$). The latter indicates that there is no regular pattern of similar distances of the regions, otherwise a distinct maximum would be seen.

The correlation lengths r_l for the spectroscopy maps are summarized in Fig. 8.8. They represent the smallest diameter of structures with similar tunneling conductivity, which are repeated several times. Different measurements for the 3D (red) and LL (green) films were regarded. Firstly it can be seen, that the magnetic field does not severely change the correlation lengths (compare the squares and circles), and sometimes they are not changed at all. Secondly, there is a difference between the length scales of the 3D and LL sample. Disregarding the points in the box, the LL film shows smaller characteristic dimensions ($r_l \approx 5 - 10\,\text{nm}$) than the 3D film ($r_l \approx 10 - 17\,\text{nm}$). Although these differences are not very large, they seem to be systematic. Larger structures with orientations into different directions cannot be seen in the self-correlation, since the folding only shifts the pictures with respect to each other, but rotational variances are disregarded. The correlation lengths can be seen as a measure for the length scale[11] of local effects, like disorder or strain.

One of the measurements (F) on the LL film was done on a larger scale ($1000\,\text{nm}^2$)

[11] The correlation analysis given here cannot predict anything below 2 nm, the given correlation lengths of 5 nm are already at the edge of resolution caused by the statistics.

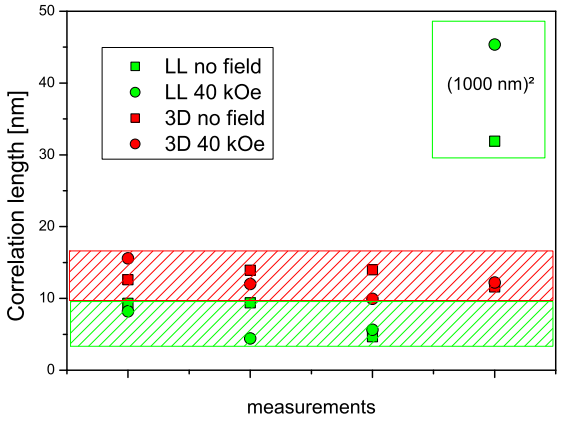

Figure 8.8.: Correlation lengths determined from several STS maps for the 3D and LL samples, which were about $(150\,\mathrm{nm})^2$ to $(250\,\mathrm{nm})^2$ in size. The points in the box were determined on the LL film from a $(1000\,\mathrm{nm})^2$ conductivity map (measurement F).

and shows visually much larger regions, as stated in Chap. 7. This is also reflected in the correlation length shown in the green box of Fig. 8.8. The tunneling conductivities and the histograms were comparable to the measurement on a smaller scale (Fig. 7.25), therefore the regions have similar electronic properties. It seems that at least the LL film develops some kind of self similar structures, which probably might be scaled down again to much smaller dimensions (on the atomic scale).

8.3.3. Comparison with the models

The discussion so far pointed out that the STS maps provide useful information about regions of different tunneling conductivities. It is therefore tempting to compare the results obtained from this work with phase separation models. An overview over some models was already given in Chap. 2. By now the measurements should be compared with these models.

Ahn et al. [1] presented a theory with local strain fields in manganites, in which the metallic phase is undistorted and the insulating phases show short- or long-wavelength lattice distortions. The model does not include the origins of these distortions or the resulting magnetic properties. A local variation of the strain seems to be a good picture for the thin films studied in this work. A non-uniform distribution of (A-site) ion radii, especially within the 3D film, should cause different local strain fields within certain regions, like for instance screw dislocations and Jahn-Teller distortions within the structure. These regions then could be attributed to the differences in local tunneling conductivity.

The model does not exclude the existence of several phases, whereas only the undistorted one is considered to be metallic. An intermixture is not discussed. One disadvantage of the model is that it considers only a 2 dimensional lattice, which might show different effects than a 3 dimensional one. Another disagreement with

the results of this work is the prediction about the effects of magnetic fields. The latter should increase the metallic volume fraction according to the model, which is not the case here. Unfortunately small local rearrangements of the distortions of all regions to veer toward a less distorted case within a structural transition coupled to the metal-insulator transition were not considered in the model.

The most frequently mentioned model is probably the resistor network model from Mayr et al. [14]. As was already discussed, no distinct two phase behavior, like it was observed for charged ordered manganites (see below, Renner et al.), can be found for the ferromagnetic LCMO films used in this thesis. Therefore the two-resistor model is not directly applicable in this case for the length scales covered. The changes observed within different regions are more gradual and a field induced increase can be found in all regions similarly. The extended model (including the change in volume fractions of the two phases) implies a percolative transition, which was neither observed for the temperature dependence nor for the magnetic field dependence of the tunneling conductivity within the measurements of this thesis or comparable STS results from other groups. There is no distinct second electronic phase and therefore such a phenomenological description would have to be changed in some details. For example, more than two different resistors would be needed. The $I(U)$ curves do not show a gap and a thermally activated transport cannot be deduced from these observations. Regarding percolation paths, a growth of one phase on the cost of the others would be expected, which was not observed here. It is not excluded, that such a behavior might be observed for manganite with the strong tendency to charge ordering, since the models were initiated by considering theses kinds of compounds. There seems to be a difference between the behavior of manganites depending on the ground state at low temperatures, which can be either FM or AF/CO.

A similarity with the resistor model is the change of the metallic phase. In the model not a simple linear summation of the partial fractions of the resistors was performed, but the metallic part was allowed to change with temperature. Assuming that a reduction in temperature is comparable to the application of a magnetic field – both reduce the resistivity and tunneling conductivities of the films – it might be partially describing the system if one would leave out the insulating resistor and instead use metallic like resistors with slightly different resistivities.

Another model, mentioned in Chap. 2.2, was a Random Field Ising Model [19]. In this the formation of clusters was discussed. The random fields represent a distribution of different coupling strengths and hopping matrix elements due to disorder. A two dimensional model would not fit into the correlation analysis here, but the three dimensional case leading to larger clusters for a high degree of disorder within the simulations could probably be compared to the size effects observed in the correlation study and by the visual examination of the STS maps. The picture for the reaction of the system on a magnetic field with the growth of some clusters does not reflect the behavior in the films here. On the other hand the introduction of disorder is definitely a meaningful idea, as could be seen by the discussion above. This is probably not necessary for an ideal ordered structure, but

a large fraction of samples produced would not account for this ideal case. How the disorder could be best introduced into a theory is beyond the scope of this work.

In conclusion, the existing models cannot entirely describe the experiments of this work. A true percolation was not observed and no distinct electronic phases were found on the given length scales, although the resistor model could be modified for a more appropriate description. The model, which is most appropriate in comparison, are the considerations of Ahn et al. about local strain fields in the sample. It can be seen that it is still very important to obtain more data about manganites, since the calculations with all important parameters involved are quite complicated. (In a newer publication from Şen et al. [31] reports about the computer clusters needed for the one- and two-orbital models.) Another problem of model calculations is to cover realistic situations rather than considering idealized cases only. Additionally the problem of such models will always be the intermediate case between itinerancy and non-itinerancy of the electrons. The models mainly consider either an AF insulating or FM metallic phase, but it is not considered how a metallic region might be driven into the direction of an insulating region due to strain and disorder.

8.4. Comparison with other STM and STS studies

The results obtained here shed some new light onto the CMR effect in manganites. In the following, the results are compared with other STS experiments reported on in literature. While the first studies were done only with a few spectroscopy curves per sample, the STS measurements as well as the sample preparation were improved over the past years and lead to more reliable results. Most of the experiments concentrated on the temperature dependence of the spectroscopy. STS studies with magnetic field are very rare.

The first STS measurements on manganites within magnetic fields were reported from Fäth et al. [7], which were carried out on $La_{1-x}Ca_xMnO_3$, $x = 0.25, 0.3$ single crystals and $La_{1-x}Ca_xMnO_3$, $x = 0.27$ thin films deposited by sputtering on STO substrates. The spectroscopy was done in magnetic fields between 0 T and 9 T at a bias voltage of 3 V. This group also reports about an electronic phase separation from nearly insulating to nearly metallic behavior with a percolative like transition, for which a few regions supposedly do not change. Unfortunately in the work no histograms are given, and it therefore cannot be directly compared to the observations in this work, although the conductivity maps given in the paper also seem to change continuously in most of the regions. The magnetic field effects are observed as well and the ratio of the tunneling conductivities with nearly 80% nearby the transition are practically the same as obtained within this work, when a normalization with respect to zero field is used as it was the case in the reference. The main shift in tunneling conductivity was observed between applied fields of 1 T and 3 T with some marginal shifting for 9 T, which matches the saturation like behavior of the resistivity in manganites with a non-zero slope over the entire field range. On the other hand, the measurements done by Fäth et al. were performed at a different energy and it is the question what kind of electronic states of the

sample they observed. For a bias of 3 V band bending effects are not negligible any more, especially for semi-metals or semi-conductors. The samples used by Fäth showed a height variation of $\lesssim 20\,\mathrm{nm}$, which occurs to be very rough compared to both 3D and LL films, and additionally films grown on STO usually possess a large misfit stress. Therefore the influence of structural inhomogeneities was supposedly much larger for their samples, confirmed also by the smaller T_C and T_{MI} .

To the author's best knowledge, only one more group tried tunneling spectroscopy measurements in magnetic fields [6] on $La_{1-x}Ca_xMnO_3$, $x = 0.33$ epitaxially grown on STO substrates. This group obtained a phase separation, which is correlated to the thin film morphology and changes irreversibly with an applied magnetic field. The growth of the samples is not further discussed, but seems to be a very rough grain like growth, which does not seem to be comparable to the topographies for other LCMO films on STO [30] (see Sec. 8.1). Regions of markedly different conductivities were seen, which appear and disappear irreversibly with the application of magnetic fields. Seemingly, the samples do not match the growth structures of the films in this work and cannot be compared. It was not explained why the different regions change irreversible by the application of an applied field. The experience during this work showed, that normally a structure in the STS maps concomitant with the topography could be attributed to scanning artifacts.

Temperature dependent STS measurements were done by T. Becker et al. [3]. The films ($La_{0.7}Sr_{0.3}MnO_3$) were deposited by reactive sputtering on MgO or $La_{0.7}Ca_{0.3}MnO_3$ deposited by the MAD technique. The latter was at that time still in its childhood days with respect to deposition of manganite thin films. The films showed a pronounced 3D growth with a somewhat lower T_{MI} for the LCMO films compared to the corresponding studies of this thesis. On the films used by T. Becker the tunneling conductivities showed a broader range with a much more pronounced insulating behavior for some regions. An increase in the overall tunneling conductivity with increasing temperature was seen for these films and they were discussed in terms of a percolative model. This continuous change in tunneling conductivity with temperature was projected onto the two resistance model by the help of a threshold value, which was taken as the border between low and high conducting parts. Therefore the temperature evolution compares with that observed in this work.

It was reported before [2] that oxygen degradation in vacuum can be a problem during the measurements, which was not observed in this work. The LL sample was kept in vacuum for weeks, while a second piece of the same sample was stored under ambient conditions. Due to an oxygen degradation a more insulating behavior or a removal of surface layers [2] would be expected, but this was not observed here. For the 3D samples there was also no observation of changes, which could be ascribed to a oxygen deficient surface were observed. No removals of surface layers or other changes on the scanned areas were observed, which can be confirmed by the pictures given in Fig. 7.14. The large frame was measured after three pictures including spectroscopy curves were taken on the small frame before. No topographical changes were seen in the scanned area. The latter also rules out any oxygen removal from the surface due to reversed bias between tip and sample. The MAD

deposited films seem to be very stable under ultra high vacuum conditions at room temperature.

Some high resolution STM measurements were performed on the LL-O film ($La_{0.75}Ca_{0.25}MnO_3$ /MgO) [33]. For two temperatures below and above the MIT atomic resolution pictures were taken. Both show some stripe-like features; these stripes appear to be parallel to the crystallographic axis with commensurate periodicities of 6.5-8.6 Å at $T = 115\,\mathrm{K} < T_C$ and diagonal to the crystallographic axis with a periodicity of 5.8 Å at room temperature. The latter show two different corrugations of 6 Å and 4 Å. The development of these stripe-like structures is attributed to a structural quasi-organization of distortions on a very small scale, that is within the superlattice unit cell, due to a long-range cation ordering. STS curves measured on the commensurate stripes are reported to be more conducting than the incommensurate stripes at room temperature which are insulating like show a depletion of states near the Fermi level for $(dI/dV)_{V\to 0}$. These stripes are associated with greater distortions. The existence of stripes concomitant with metallicity below the MIT is explained with orbital ordering associated to the stripes. The charge fluctuations within the stripes are compared to the bulk and a phase separation with two different conductivities was ruled out by the authors.

Of course the intention is to find a global theory describing local electronic properties in manganites, but a proof of a final theory is still lacking. It is not clear how these microscopic features appear on larger areas and if they are always present. It is not very easy to compare these results with the results of this thesis, since no atomic resolution could be achieved with the experimental setup and the following considerations are rather speculative. Measurements on an atomic scale would be necessary to possibly detect stripe phases and their possible development within magnetic fields. It should be noted here that the LL sample used for this thesis does not necessarily exhibit a long-range A-site ordering as the LL-O sample and the STS maps obtained reveal only features on a larger length scale. In comparison with the STS curves for the stripe phase at room temperature, all of the STS curves of the measured films in this thesis show a more conducting like behavior (compare for instance Fig. 8.2) than the dI/dV-curve for the room temperature stripe phase given in [33]. This might be an indication that the high temperature stripe phase is also not present below the MIT for the films used in this thesis and a phase mixture of both might not be very likely. On the other hand there are different regions with different tunneling conductivities present, but how they are composed on an atomic scale cannot be seen. Since the stripe phases are associated with distortions, a differentiation between very local (on the unit cell scale) distortions, which appear to be in order to the cation ordering and global distortions, which extend over a larger number of unit cells and can be associated with a certain degree of disorder. Another point is the question of what can be exactly defined as the different phases. At least it might be possible that the LL film here also would show microscopical stripes on ordered parts and the latter is not a contradiction to the results of this work as well as a possibly orbital ordering.

Extensive temperature dependent STS studies on $La_{1-x}Ca_xMnO_3$ films with

$x = 0.3$, which were deposited on NGO by pulsed laser deposition, were performed by another group [18]. The surface structure, sharpness of the transition and T_{MI} are comparable with the LL films of our group. On these LCMO/NGO films no phase separation was observed, although the tunneling conductivity map given in [18] shows some artifacts of a slow feedback loop at the terrace edges of the film. The group studied the temperature dependence of the overall tunneling conductivity. It has a tendency towards smaller tunneling conductivities nearby the T_{MI} (a depletion of DOS), which matches the results presented here. Accordingly also no gap was seen. However in their simulations a small gap appears and reaches a maximum nearby the transition with $\Delta = 0.2\,\mathrm{eV}$ [18, 9]. Since it is very difficult to differ between finite temperature effects and this simulated gap, it was called a "soft" gap. The smooth temperature evolution of the tunneling conductivity shows an evolution, which is consistent with that measured at different temperatures here. (The values are not directly comparable, since the initial sample bias for the STM measurements was not the same and therefore the tip-sample distance was not the same.)

Further STM studies on other manganites were done on single crystals in the group of Renner et al. [26, 29]. The first was done on $Bi_{0.24}Ca_{0.76}MnO_3$, a compound which shows charge ordering below the charge ordering temperature $T_{CO} = 240\,\mathrm{K}$. A phase separation on an atomic scale was observed, where both phases show a different atomic periodicity and quite different tunneling conductivity at 299 K in the paramagnetic phase. The latter is not a contradiction to the measurements within this thesis. The $I(U)$ characteristics is quite similar to those seen here. There are some theories, which predict phase separation only for an interplay between a metallic and a charge ordered insulating phase [16], while the latter is not known to occur in the ferromagnetic region for $La_{0.75}Ca_{0.25}MnO_3$. Renner et al. observed also an insulating phase with a checkerboard pattern with an insulating gap of 0.7 eV at 299 K [27]. If this kind of phase had been present in the $La_{0.75}Ca_{0.25}MnO_3$ films of this thesis, at least some of the spectroscopy curves would have been expected to show also such a large gap, which is not the case. Therefore a presence of this phase is quite improbable here. A stripe pattern [27] (probably similar to that one in [33]) was also observed and showed a much smaller gap. If this phase might be present on a very small scale in the $La_{0.75}Ca_{0.25}MnO_3$ - films cannot be clarified within this thesis. For the LL-O film such a phase was only found for temperatures $T > T_{MI}$ [33] and it showed a more pronounced decrease of the DOS than observed for the spectroscopy data in this thesis.

The second study of this group carried out by Rønnow et al. [29] was done on a layered manganite single crystal, that is $La_{1.4}Sr_{1.6}Mn_2O_7$. The crystal was cleaved in-situ for the STM measurements. At first also half unit cell steps were found, which is a hint that the ripples on the films of this thesis are only caused by the specific crystal structure. (It is known that it is impossible to cleave $La_{0.75}Ca_{0.25}MnO_3$ single crystals with a smooth surface, it appears always to be somewhat rough, since there are no layers which could serve as ideal cleaving planes.) The interesting point of the results on $La_{1.4}Sr_{1.6}Mn_2O_7$ is, that also no phase separation was found and that the slopes of the spectroscopy curves are

changing gradually with temperature, while the histograms showed a Gaussian distribution.[12]

The last important STM study which should be mentioned here comes from Ma et al. [12]. Epitaxial films of $(La_{5/8-0.3}Pr_{0.3})Ca_{3/8}MnO_3$ were prepared in-situ on Nb-doped STO single crystals by laser molecular beam epitaxy. This compound belongs to the ferromagnetic - charge ordered manganites. By voltage dependent imaging (a typical technique used on real semiconductors) they were able to distinguish between occupied and unoccupied states (including localized holes at the Mn^{4+} site) at room temperature in the paramagnetic state. Some CE-type (see Chap. 2) charge ordered clusters were found. The distributions were analyzed by a hole-hole correlation and revealed quite small values, namely 2.6 holes for random distribution clusters, 1.9 holes for non-charge ordered clusters and a much higher value (>10) for charge ordered clusters. Interestingly this kind of distribution shows up for a compound exhibiting charge ordering. The cluster sizes of the other "phases", if one could speak of phases at all for such small dimensions, is quite small and could not be revealed by the microscope used for this work. Additionally it is questionable whether the same kind of phase separation could be found for the metallic compounds due to screening effects of delocalized electrons.

In summary, there are other STS studies, which show results consistent with those obtained within this work. Some differences can be attributed to different sample properties, which are strain effects in similar compounds or different doping atoms, which lead to a different behavior like charge ordering in insulating phases. Some of the measurements partially supplement the observations here (LCMO/NGO films), while others confirm the usefulness of the measuring techniques and analyzing methods (Renner et al.). The magnetic field effects cannot be directly compared to those of Fäth et al., which were done at the early stages of STS studies on manganites. Therefore the effects caused by the magnetic field observed here can be regarded as new and helpful in order to understand the nature of the CMR effect and the metal-insulator transition, especially with respect to disorder effects.

8.5. The metal-insulator transition in manganites

The type of phase transition in manganites is a very controversial issue and up to now an unsolved problem. As was summarized in Chap. 2.3 there are very contradictory theoretical and experimental results regarding the order of the phase transition. Certainly the theoretical considerations depend to a large extent on the simplifications made and the experimental results are coupled to the sample quality and resolution of the measurements. Therefore, due to the complicated interplay of charge, lattice and orbital degrees of freedom, it is a demanding task to obtain reliable data. In particular there might be more than one model, since

[12] Also an increase of the histogram width with the tunneling conductivity was ascribed to instrumental noise. This is another confirmation of the reliability of the measurements done within this thesis.

the manganites might be very different as was already shown by the very rich phase diagram (Fig. 2.12). At most it can be expected to find some explanations for special parts of the phase diagram, like the ferromagnetic compounds or those showing charge ordering.

With the help of the results obtained in this work, it is possible to extend the facts known so far to the very important issue of the metal-insulator transition in a magnetic field and contribute some considerations concerning the metal-insulator and ferromagnetic-paramagnetic phase transition.

As was shown in this thesis, there are already differences within thin films on the same substrates, grown under different deposition speeds (App. A). Fortunately the positive result is that – although the electronic transition changes locally – it became apparent for the whole series (from 3D over LL up to LL-O films) that the magnetic field changes the tunneling resistivity more or less uniformly all over the samples and no distinct two phase behavior is present. The latter result might speak against a first-order transition, since a separation into two distinct phases is not existent, and seems to be more appropriate for a continuous second order transition. On the other hand a first-order transition does not necessarily have to show a phase separation.

The author suggests that the electronic transitions in manganites are coupled to their intrinsic nature, which might be very different. It might depend on the itinerancy of the electrons. The charge ordered manganites tend to show a first order like transition coupled with a phase separation. The latter is confirmed by the experiments discussed above and for instance the new results from Wu et al. who found a glass like transition with a first-order nature by MFM measurements on $La_{5/8-y}Pr_yCa_{3/8}MnO_3$, $y \approx 0.4$ [35]. Phase separation can only be predicted for a first-order transition and so far mainly the charge ordered compounds showed a clear phase separation. Since the non-existence of a phase separation on a nanometer scale below 2 nm cannot be clearly proven and the problem of a missing clear definition of the phases, a final determination of the nature of the transition is not possible at this stage. Due to the tunable parameter-space in manganites it is probably also impossible to clearly talk about the one or the other phase transition with exactly first or second order, it might be a mixture. There is no proof how the Ginzburg-Landau formalism could be generalized to these materials.

The latter considerations are matching at least partially the generalized phase diagram from Littlewood et al. [13], shown in Fig. 8.9. The key parameter here is the electron-phonon coupling. The authors claim that for a very weak coupling $\lambda < \lambda_0$ a second-order phase transition without phase separation could be expected, while for a lager coupling $\lambda > \lambda_0$ a discontinuous transition of first-order nature with phase separation in the transition region is more probable. The white shaded region is attributed to a possible (but not necessary) phase coexistence and the yellow shaded region is attributed to a second order phase transition, while the unshaded region corresponds to a first-order transition. The red lines denote first-order transitions between the phases, and therefore the observation for compounds with charge ordering tendencies and ferromagnetic phases can be found in the region of first-order phase transitions.

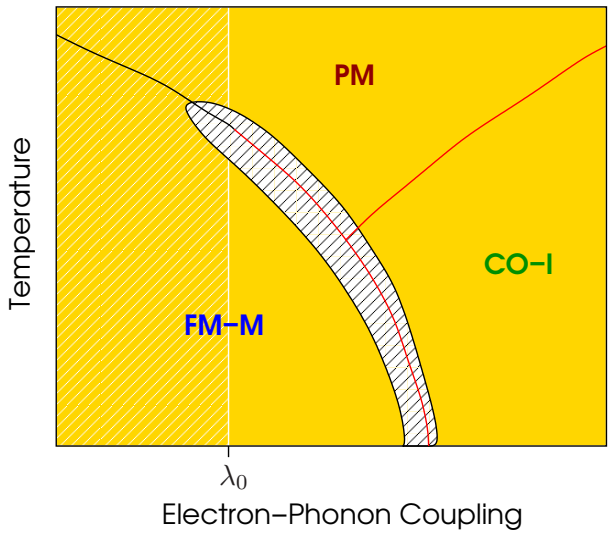

Figure 8.9.: Phase transitions with temperature versus the electron phonon coupling parameter after Littlewood et al. [13]. Red lines mark a first-order like transition. PM: paramagnetic region, FM-M: ferromagnetic metal, CO-I: charge ordered insulator.

On the one hand the films used here might be situated in the yellow shaded region below λ_0. A vivid discussion is still going on about the role of the polarons, but the electron-phonon coupling could not be measured directly. The spectroscopy data showed an itinerant electron behavior and no hints for a localization were found on the length scales considered. The observations within magnetic fields confirm a continuous change of the tunneling conductivity. On the other hand, the different regions of gradually varying conductivity can be interpreted in terms of small variations of strain fields within the films. In conclusion these different regions might have different transition temperatures T_{MI}, which are highly dependent on the microstructure, as was discussed above. These small inhomogeneities change their conductivity continuously with respect to a magnetic field, but since the transition varies spatially over the film, the region pattern remains across the transition of the whole film. This leads to the broadening of the MIT for the 3D and LL films compared to the highly ordered LL-O film. The change in tunneling conductivity for all regions can be explained by this local variation of T_{MI}. From this point of view also a distribution of many first-order phase transitions at slightly different temperatures in the different regions is also a possibility, provided that the sharp MIT for the LL-O film is of first-order nature without intrinsic phase separation. There are some weak hints for a first-order transition in the LL-O film, which need yet to be corroborated.

Of course it has to be taken into account that STS is a very local and surface sensitive technique. Most people would expect nearly the same behavior for the manganites at the surface as in the bulk, but this is not absolutely clear. The STM can detect more than a surface layer, but still mainly detects the surface properties at which the sample changes the geometry from a three-dimensional lattice to a two-

dimensional surface layer. The magneto resistance is the same for both samples, which was shown before, but the difference in the tunneling spectroscopy between the samples, which were both examined nearby T_{MI}, is evident.

As mentioned in Chap. 2.3, different experiments on the phase transition lead to different results concerning the order of the transition. The heat capacity measurements are not unambiguous and furthermore it is the question which parameter would be the correct order parameter for manganites. At this point more work has to be done to clarify this issue.

Bibliography

[1] K. H. Ahn, T. Lookman, and A. R. Bishop. *Nature*, 428:401, 2004.

[2] T. Becker. *Untersuchung der elektrischen Phasenseparation in dünnen Manganatschichten mit Rastersondenspektroskopie.* Doktorarbeit, Universität Göttingen, 2004.

[3] T. Becker, C. Streng, Y. Luo, V. Moshnyaga, B. Damaschke, N. Shannon, and K. Samwer. *Phys. Rev. Lett.*, 89:2372038, 2002.

[4] A. Biswas, M. Rajeswari, R. C. Srivastava, Y. H. Li, T. Venkatesan, R. L. Greene, and A. J. Millis. *Phys. Rev. B*, 61:9665, 2000.

[5] D. A. Bonnell. *Prog. Surf. Sci.*, 57:187, 1998.

[6] S. F. Chen, P. I. Lin, J. Y. Juang, T. M. Uen, K. H. Wu, Y. S. Gou, and J. Y. Lin. *Appl. Phys. Lett.*, 82:1242, 2003.

[7] M. Fäth, S. Freisem, A. A. Menovsky, Y. Tomioka, J. Aarts, and J. A. Mydosh. *Science*, 285:1540, 1999.

[8] M. Izumi, Y. Konishi, T. Nishihara, S. Hayaschi, M. Shinohara, M. Kawasaki, and Y. Tokura. *Appl. Phys. Lett.*, 73:2497, 1998.

[9] S. Kar, J. Mitra, and A. K. Raychaudhuri. *Solid stat. commun.*, 136:410, 2005.

[10] S. A. Köster, V. Moshnyaga, K. Samwer, O. Shapoval, A. Belenchuk, O. I. Lebedev, and G. van Tendeloo. *Appl. Phys. Lett.*, 81:1648, 2002.

[11] N. Lang. *Phys. Rev. Lett.*, 56:1164, 1986.

[12] J. X. Ma, D. T. Gillaspie, E. W. Plummer, and J. Shen. *Phys. Rev. Lett.*, 95:237210, 2005.

[13] N. Mathur and P. Littlewood. *Physics Today*, 56:25, 2003.

[14] M. Mayr, A. Moreo, J. A. Verges, J. Arispe, A. Feiguin, and E. Dagotto. *Phys. Rev. Lett.*, 86:135, 2001.

[15] D. N. McIlroy, J. Zhang, S.-H. Liou, and P. A. Dowben. *Phys. Lett. A*, 207:367, 1995.

[16] G. C. Milward, M. J. Calderón, and P. B. Littlewood. *Nature*, 433:607, 2005.

[17] J. Mitra, M. Paranjape, A. K. Raychaudhuri, N. D. Mathur, and M. G. Blamire. *Phys. Rev. B*, 71:094426, 2005.

[18] J. Mitra, M. Paranjape, A. K. Raychaudhuri, N. D. Mathur, and M. G. Blamire. *Phys. Rev. B*, 71:094426, 2005.

[19] A. Moreo, M. Mayr, A. Feiguin, S. Yunoki, and E. Dagotto. *Phys. Rev. Lett.*, 84, 2000.

[20] V. Moshnyaga, B. Damaschke, O. Shapoval, A. Belenchuk, J. Faubel, O. I. Lebedev adn J. Verbeek, G. van Tendeloo, M. Müksch, V. Tsurkan, R. Tidecks, and K. Samwer. *Nat. Mat.*, 2:247, 2003.

[21] V. Moshnyaga, L. Sudheendra, O. I. Lebedev, S. A. Köster, K. Gehrke, O. Shapoval, A. Belenchuk, B. Damaschke, G. van Tendeloo, and K. Samwer. *Phys. Rev. Lett.*, 97:107205, 2006.

[22] W. E. Pickett and D. J. Singh. *Phys. Rev. B*, 53:1146, 1996.

[23] P. G. Radaelli, G. Iannone, M. Marezio, H. Y. Hwang, S.-W. Cheong, J. D. Jorgensen, and D. N. Argyriou. *Phys. Rev. B*, 56:8265, 1997.

[24] R. A. Rao, D. Lavric, T. K. Nath, and C. B. Eom. *Appl. Phys. Lett.*, 73:3294, 1998.

[25] R. A. Rao, D. Lavric, T. K. Nath, C. B. Eom, L. Wu, and F. Tsui. *J. Appl. Phys.*, 85:4794, 1999.

[26] Ch. Renner, G. Aeppli, B.-G. Kimm, U.-A. Soh, and S.-W. Cheong. *Nature*, 416:518, 2002.

[27] Ch. Renner, G. Aeppli, and H. M. Rønnow. *Mater. Sci. Eng. C*, 25:775, 2005.

[28] P. Reutler, A. Bensaid, F. Herbstritt, C. Höfener, A. Marx, and R. Gross. *Phys. Rev. B*, 62:11619, 2000.

[29] H. M. Rønnow, Ch. Renner, G. Aeppli, T. Kimura, and Y. Tokura. *Nature*, 440:1025, 2006.

[30] F. Sánchez, I. C. Infante, U. Lüders, Ll. Abad, and J. Fontcuberta. *Surf. Sci.*, 600:1231, 2006.

[31] C. Şen, G. Alvarez, and E. Dagotto. *Phys. Rev. Lett.*, 98:127202, 2007.

[32] J. Shin, S. V. Kalinin, H. N. Lee, H. M. Christen, R. G. Moore, E. W. Plummer, and A. P. Baddorf. *Surf. Sci.*, 581:118, 2005.

[33] L. Sudheendra, V. Moshnyaga, E. D. Mishina, B. Damaschke, Th. Rasing, and K. Samwer. *Phys. Rev. B*, 75:172407, 2007.

[34] E. L. Wolff. *Principles of Electron Tunneling Spectroscopy.* Oxford University Press, New York, 1985.

[35] W. Wu, C. Israel, N. Hur, S. Park, S.-W. Cheong, and A. de Lozanne. *Nat. mat.*, 5:881, 2006.

9. Summary and outlook

A lot of open questions still remain in manganite physics. The exact nature of the coupled metal-insulator and ferromagnetic-paramagnetic phase transition is under debate. There are a lot of models, which consider a phase separation to explain the large CMR effects, but it is not known if phase separation is a necessary condition for such effects. A lot of bulk measurements lead to controversial results with respect to the nature of the transition, where they cannot exactly reveal the microscopic mechanisms. Microscopic techniques are necessary to gain a deeper insight into the local properties and how they are influenced by external parameters, like the temperature or a magnetic field.

In manganites structural, electronic and magnetic properties are strongly coupled to each other due to an interplay of charge, lattice and orbital degrees of freedom. The two competing exchange mechanisms, the super exchange (mainly responsible for antiferromagnetic coupling and localization) and the double exchange (providing a ferromagnetic coupling and delocalization of the charge carriers) and a strong electron lattice coupling are responsible for the metal-insulator and ferromagnetic-paramagnetic transition and the large CMR effect. A comprehensive picture has therefore to include structural, electronic as well as magnetic information of the system. In this work scanning tunneling spectroscopy (STS) experiments on ferromagnetic manganites provide detailed information on the local electronic properties, while the macroscopic structure, transport and magnetization have been determined by standard techniques.

Different macroscopically strain-free films of $La_{0.75}Ca_{0.25}MnO_3$, deposited by the MAD technique on MgO substrates, show a varying microscopic texture. A three dimensional (3D) and layer by layer (LL) growth, depending on the deposition conditions, were observed. The 3D films showed the typical orthorhombic structure, normally reported for LCMO films, while the LL films possess (the more pseudo-cubic like) rhombohedral structure coupled to an increased ordering of the A-site atoms [3]. The bulk properties like the resistivity and magnetization follow these observation in the sense that the electronic and magnetic transitions as a function of temperature are broader for the 3D film connected with lower transition temperatures (Chap. 6).

The local tunneling conductivity was measured by STS, and two-dimensional tunneling conductivity maps were generated for different temperatures and magnetic fields below, but nearby the metal-insulator transition temperature. Within these STS maps regions with different tunneling conductivities were found, but all of them showed metallic like current-voltage characteristics and the differences between the conductivities were small. The different regions were suggested to be attributable to uncompensated local strain fields in the films caused by disorder. The films could be quantified with respect to the disorder and the occurrence of

different regions. An ideally ordered film (not examined in this thesis) showed no different phases, while the size of different regions increased with supposedly increasing disorder from the LL to the 3D films.

The $I(U)$ curves taken on differently conducting regions revealed a gradual increase of the tunneling conductivities with temperature and magnetic field nearby the metal-insulator transition (Chap. 7). All regions increased their conductivity by more or less the same value. No two distinct phases were found and a simple two-phase percolative model does not account for the ferromagnetic manganite $La_{0.75}Ca_{0.25}MnO_3$. A magnetic field induced increase of the density of states, which is depleted in the vicinity of the metal-insulator transition, was observed. No insulating gap was observed in the low conducting regions, in contrast to charge ordered manganites, see e.g. [4]. It can therefore be concluded, that a phase separation with two distinct conductivities, an insulating and metallic phase, cannot be confirmed here at least on the observed length scales, although there is a tendency to more pronounced phases for the more disordered film.

A first-order phase transition is believed to be appropriate for manganite compounds, which show charge ordering and a clear phase separation. For the ferromagnetic compound $La_{0.75}Ca_{0.25}MnO_3$ contradictory results regarding the phase transition were presented in the literature. The results obtained here show a continuous change of the tunneling conductivity with respect to magnetic fields. The order of the transition cannot be finally determined due to the quite sharp transition in the resistivity for the LL-O film. The possibility of a distribution of different transition temperatures in the different regions (phases) coming up with the disorder was suggested.

In a nutshell, the observed effects of magnetic fields on the local tunneling spectroscopy together with the structural properties, revealed new aspects related to the metal-insulator transition in the ferromagnetic manganites. A percolative scenario seems not to be a necessary prerequisite for the CMR. It provides a contribution to the understanding of the mechanisms being responsible for the adjacent colossal magneto resistive effect (CMR), which occurs mainly at the metal-insulator transition region (Chap. 8). The nature of the phase transition cannot be finally identified, but by the microscopic technique a continuous change of the local electronic properties by magnetic fields was visualized. A probable connection between the electronic properties and (A-site) disorder was outlined.

9.1. Future work

It is possible to extend the picture given in this work to the local magnetic moments. This could be achieved by means of spin-polarized measurements and one of these is the spin-polarized scanning tunneling spectroscopy (SP-STS) [1], which was established by the group of M. Bode and W. Wulfhekel. With this technique it is possible to observe the spin-polarization of a surface very locally, down to the atomic scale.

For high resolution STM measurements, atomically flat surfaces are required and therefore an appropriate surface preparation is needed, if the samples cannot be

prepared in-situ by, for example, pulsed laser deposition. It is quite difficult to cleave such ferromagnetic perovskite manganites, since they do not have distinctive cleaving planes and normally end up with a quite rough surface. Thin films of extraordinarily high quality are the alternative, and some knowledge about the relationships between structural, electronic and magnetic properties is provided by this work. The chemical composition and surface termination layers with possibly a reconstruction are not irrelevant. On this basis an extended study of the surface layers with, for instance, XPS and LEED would be important to find an adequate surface preparation procedure, which does not destroy the surface and the intrinsic properties of the manganite. Based on the first hints about the surfaces given in the discussion, annealing under vacuum conditions with an oxygen partial pressure might help to solve this problem.

Additional scanning probe measurements are of interest also on other manganite thin films, like $Pr_{1-x}Ca_xMnO_3$. On these films peculiar electric field effects were observed in the group of Ch. Jooss [5]. A first attempt to achieve some STM pictures on the highly insulating compound with $x \approx 0.3$ was done within magnetic fields (see App. B.1). Here the development of different phases under the influence of a magnetic field would be very interesting, since a pronounced splitting into insulating and metallic phases is expected. Considering the observed electric field effects, magnetic force microscopy (MFM) measurement could reveal the development of a current path. It can be expected that a current filament could be resolved by its magnetic stray field. The latter would be an extraordinarily progress for the research within phase separation and percolation studies. A first MFM measurement is given in the appendix. Unfortunately these attempts were done on quite rough films, when the surface preparation was not as mature as it is now.

Another very interesting technique to observe the local spin configuration would be spin-polarized electron energy loss spectroscopy (EELS). Of course, the resolution is much less than for SP-STS, but it can reveal specific features on larger length scales, which could be compared to MFM measurements. This special technique is used within transmission electron microscopy, and can determine the spin-states locally and chemically resolved. It can also reveal other features, like specific magnetic excitations as magnons. A much better understanding of such excitations, which possibly also occur in manganites and related materials, could be achieved.

Of course the field of manganite physics is much broader than the experiments presented here. The optical and dynamic parts have been neglected, and only proposals directly related to this work were given. For instance, the dynamics in manganites has not been explored very much so far. Mishina et al. [2] performed second-harmonic generation experiments and probed crystallographic and magnetic effects. The dynamic effects can reveal even more about the interplay of the spin and orbital degrees of freedom via the time scales of reaction. An idea, which came up during this work, dealt about the performance of STS measurements under the optical excitation of the sample by a laser.

While there are hundreds of publications about the general manganite proper-

ties, a detailed understanding of these materials still needs to be achieved. Further investigations will require more and more complex and local techniques and a very careful sample preparation will be necessary. STS is one of these approaches considering observations on a very local scale. Not very many groups can perform STS measurements together with magnetic fields and the results of this thesis have shown, that there is still a great potential for manganite physics.

Bibliography

[1] M. Bode. *Rep. Prog. Phys.*, 66:523, 2003.

[2] E. D. Mishina, A. I. Morosov, A. V. Mishina, V. Moshnyaga, L. Sudheendra, K. Samwer, and Th. Rasing. *Phys. Rev. B*, 75:0644401, 2007.

[3] V. Moshnyaga, L. Sudheendra, O. I. Lebedev, S. A. Köster, K. Gehrke, O. Shapoval, A. Belenchuk, B. Damaschke, G. van Tendeloo, and K. Samwer. *Phys. Rev. Lett.*, 97:107205, 2006.

[4] Ch. Renner, G. Aeppli, B.-G. Kimm, U.-A. Soh, and S.-W. Cheong. *Nature*, 416:518, 2002.

[5] W. Westhäuser, S. Schramm, J. Hoffmann, and Ch. Jooss. *Eur. Phys. J. B*, 53:323, 2004.

A. Sample data

Sample	Substrate	T_{depos} [° C]	t_{depos} [min]	V_p/t_{depos} [ml/min]
MAD 27 (3D)	polished	$\approx 900 - 1000$	1.1	0.64
MAD 28 (LL)	polished	$\approx 900 - 1000$	5.6	0.125
MAD 400 (LL)	cleaved	$\approx 900 - 1000$	-	-
MAD 177 (LL-O)	polished	$\approx 900 - 1000$	2.0	2.0

Table A.1.: Sample deposition data [4]. T_{depos} deposition temperature [a], t_{depos} deposition time, V_p volume precurser solution

[a] The temperature from the heater is excactly known to be 1000℃, but the temperature on top of the substrate is presumably a little bit lower.

Substrate used:

MgO (Crystal GmbH, Berlin), in (100) out-of-plane direction, cleaned in aceton before deposition

B. Experimental supplements

B.1. STM and MFM on PCMO

Besides the ferromagnetic manganites, also the ferromagnetic insulating and charge ordered manganites are of interest, as already mentioned several times within this thesis. For the latter phase separation is less controversially discussed and there are several interesting experiments. Due to a cooperation with the group of Ch. Jooss [5] it was possible to perform test measurements on a $Pr_{0.68}Ca_{0.32}MnO_3$ thin film. Unfortunately the measurements coincided with a time of technical problems and for several reasons the project had to be terminated already at its beginning. Therefore only first examples can be shown here and they will not be interpreted in detail. The temperature dependent resistance curves for different magnetic fields and various currents (electric fields) are shown in Fig. B.1.

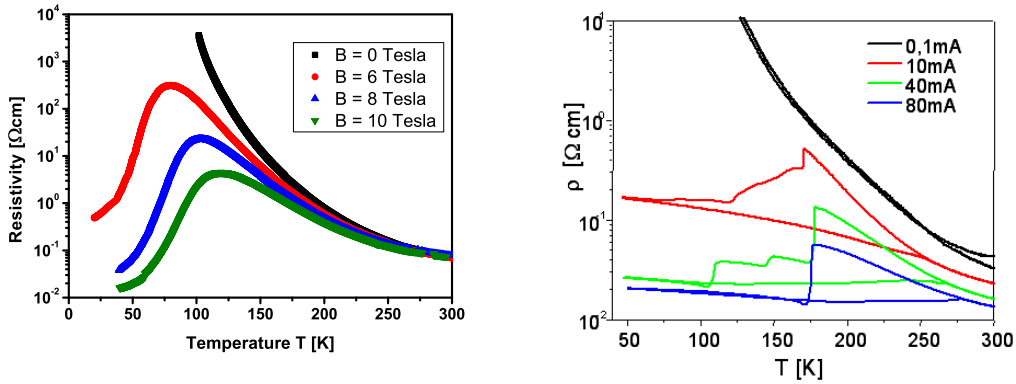

(a) (b)

Figure B.1.: The main features of the resistivity of PCMO with respect to different magnetic fields (a) and applied electric currents (b) [5, 7, 8].

The idea was to perform MFM measurements on the samples within an applied magnetic field and/or with a current flowing through the sample to detect current paths, which are supposed to rise within these samples due to percolation. For this reason, on this first $Pr_{0.68}Ca_{0.32}MnO_3/SrTiO_3$ thin film, grown by W. Westhäuser by pulsed laser deposition [7, 8], two gold contacts were deposited as demonstrated in Fig. B.2. One of the problems, which could not be easily solved, are the quite large currents, which are required to change the state of the sample. Also magnetic fields can be used to reduce the resistivity. On the other hand, it was possible to cool the sample with an applied current, but not within a magnetic field applied, since the He standing times are restricted.

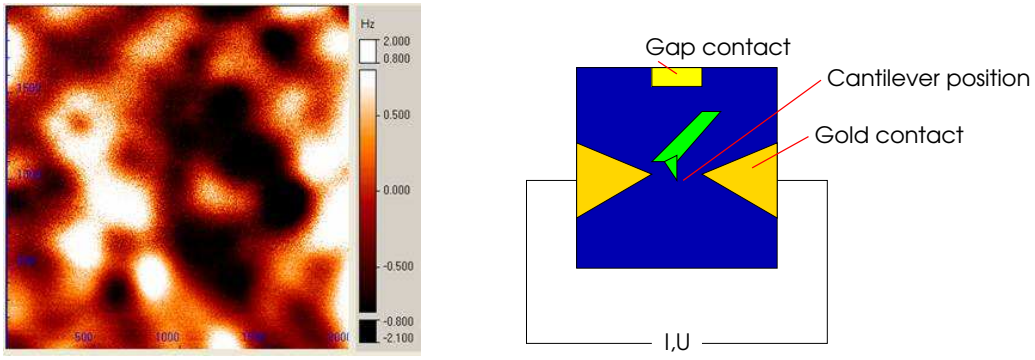

(a) (b)

Figure B.2.: MFM measurement on PCMO at 58 K, 70 kOe and 10 μA (a); the size of the image is 2 μm $\times$ 2 μm. Schematic drawing of the sample contacts (b).

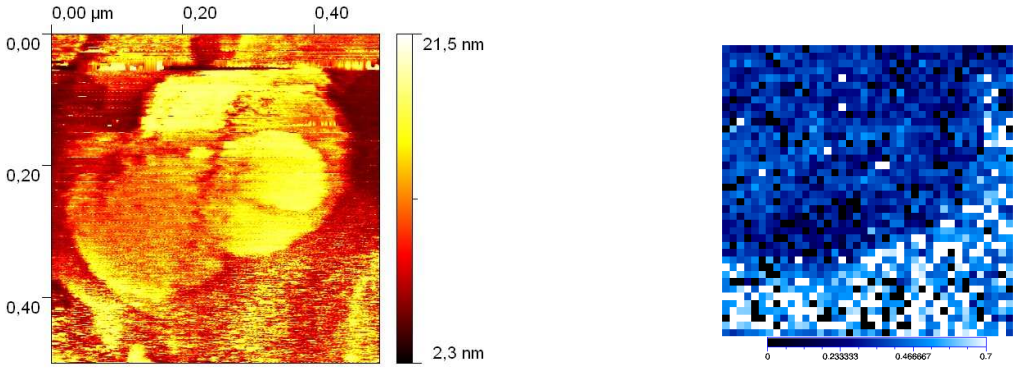

(a) (b)

Figure B.3.: Topography of PCMO sample at 70 K with an applied field of 70 kOe. The image was taken at a bias of 1 V and feedback current of 0.2 nA (a). The respective gap map obtained from the spectroscopy data.

In Fig. B.2 a first MFM picture, taken at 58 K, 70 kOe and 10 μA, is shown. (The cantilever was tested before on a CeH_2/Fe multilayer and showed the typical meander like domain structure.) The cantilever was at first kept far away from the sample to prevent any crashes. It can be seen that the film is not magnetically homogeneous and shows some domains. A current path was not found in the first attempt. Since some droplets on the sample caused problems with the stabilization of the cantilever frequency, it was unfortunately not possible to take a series of measurements with decreasing or increasing fields or currents. The deposited electrodes had a quite large distance of 2-3 mm to position the cantilever in between, therefore it is a matter of luck to find a current path within the gold triangles. For future work the samples would need to be optimized and probably microstructured to have a realistic chance to find a current path.

The second attempt was done by STM. This was probably a little bit adventur-

ous, because the resistivity of these films is quite high, but on the other hand it was also a nice opportunity for a comparison of the spectroscopy data with that measured on the LCMO films. The first attempt was done at lower temperatures, where large magnetic field effects would be expected and with a magnetic field of several Tesla. In order to lower the resistivity, see Fig. B.1 (a). Indeed it was possible to obtain some topographies. Due to the high resistivity the tip is quite near the sample and tip-crashes or a scratching of the tip on the sample are the most frequent problem, especially if the picture is not taken on one terrace only.

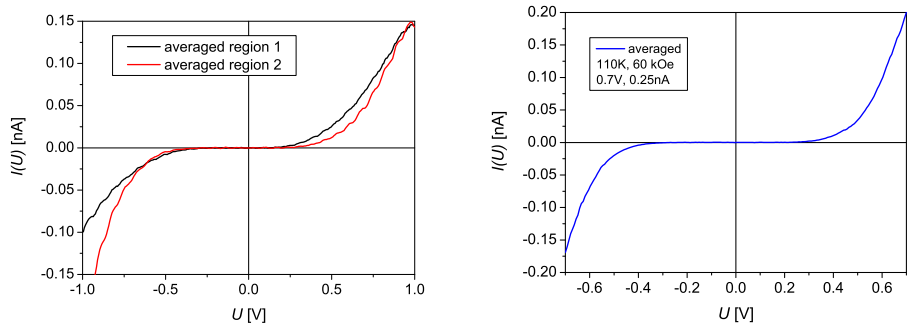

(a) **(b)**

Figure B.4.: Averaged spectroscopy curves for Fig. B.3. Region 1 denotes the dark blue region and region 2 the light blue part. (a) Another example at a different temperature and different parameters.

A topography image is given in Fig. B.3 (a). Some terraces can be seen, while in the lower right edge something else might have been on the surface. In this case it was more useful to calculate the gap map, which is shown in Fig. B.3, since the $I(U)$-characteristic was rather insulating. Two averaged spectroscopy curves are shown in Fig B.4. The two regions of dark blue and light blue color, which might be coupled to the topographical features, were taken for averaging the $I(U)$-curves. Remarkably these curves show a characteristic which is similar of semiconductors and a slight asymmetry can be seen in the curves.

An interpretation would go a little bit too far at this stage, but these experiments have some interesting potential with respect to the discussion of phase separation.

B.2. LCMO tips

Since spin-polarized tunneling is a method of general interest for STS measurements on manganites and an in-situ preparation of special magnetic tips was not possible at this stage, the author tried another experiment initiated by [1]: A piece from a $La_{0.75}Sr_{0.25}MnO_3$ (LSMO) target was taken and one of its corners was used as a tunneling tip. Due to the very rough "preparation" of these tips, only a few attempts succeeded in some images at all. Two of them will be shown here, since it is quite amazing that the test worked out at all, but they will not be commented in detail.

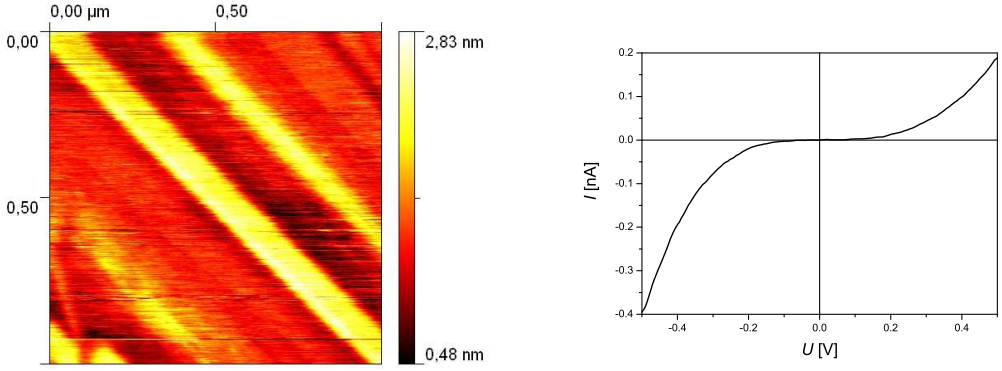

(a) (b)

Figure B.5.: First test of LSMO tip on HOPG at 30 K (0.5 V bias, 0.2 nA feedback current) in (a). Averaged spectroscopy curve (b) for the image in (a).

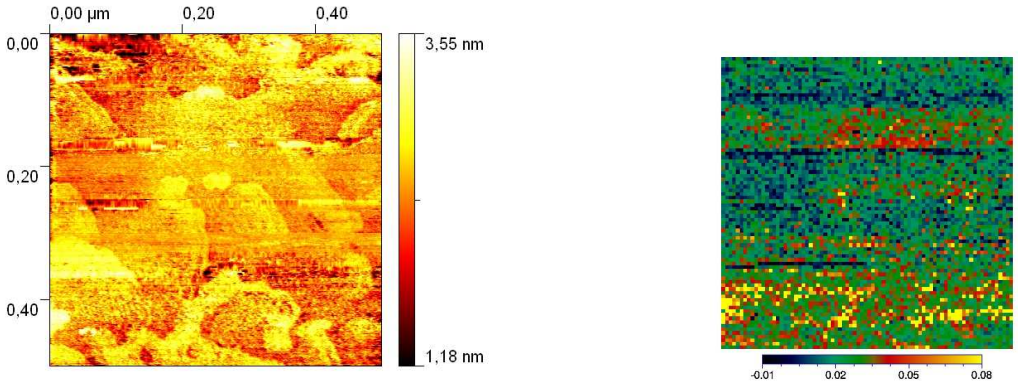

(a) (b)

Figure B.6.: First test of LSMO tip on $La_{0.75}Ca_{0.25}MnO_3$ at 30 K (0.5 V bias, 0.2 nA feedback current) in (a). Spectroscopy map (b) for the image in (a).

The test on HOPG given in Fig. B.5 (a) shows the terrace structure from HOPG. The tip was stable and the spectroscopy curves had all the same shape as can be seen in Fig. B.5 (b). The curves are asymmetric, which can be attributed to the materials of the electrodes.

In Fig. B.6 (a), the test of an LSMO tip on $La_{0.75}Ca_{0.25}MnO_3$ is shown. The typical terrace structure of the $La_{0.75}Ca_{0.25}MnO_3$ films can be identified, although most probably a double tip was present. Fig. B.6 (b) shows the respective spectroscopy map. It can be observed, that sometimes most probably the tip changes from one line to the other and does not seem to be stable throughout the measurement. Different regions can be found, but an interpretation of this map is not reasonable at this stage, especially because the $I(U)$ data was quite noisy in contrast to the measurement shown before.

B.3. Remarks on other effects in STS

There is a widespread discussion about polarons and other kinds of excitations in manganites. Some of those could be seen with inelastic tunneling spectroscopy, in which the onset of electron loss channels can be measured.

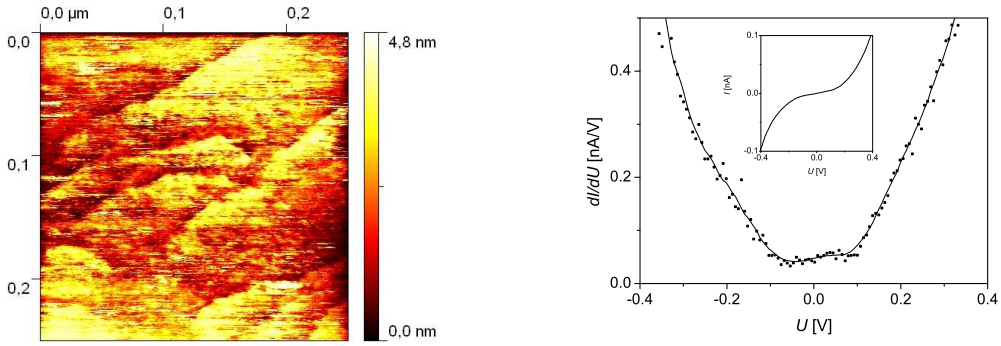

(a) (b)

Figure B.7.: Topography (a) of LL sample at $\approx 134\,\mathrm{K}$. Example for a modified $I(U)$ curve around zero bias (b).

Fig. B.7 shows an example, in which a different shape of the dI/dU curve was observed. The measurement was taken at 134 K. Since the topography seems to be somewhat smeared, the measurement and its conductivity map have to be taken with care. Some stripes in the topography can be accounted for by a modified tip-sample distance. The dI/dU curve was only averaged over parts without these stripes and showed an unusual shape around zero bias. Some hints of such a modification was seen on a few other measurements at about 150 K, but they did not show exactly the same shape. Therefore the question weather there are any inelastic parts cannot be answered at this stage, but within $\pm 100\,\mathrm{mV}$ there were eventually seen some small irregularities, which could probably accounted for by inelastic tunneling. Since in the figure shown, the topography is not so clear, any eventual other artifacts cannot be ruled out.

B.4. Tip etching procedure

Since cut PtIr tips, as used for this thesis, are very often unstable or have double tips, the author suggested to investigate a tip production which does not require a special in-situ preparation. To this end, some tip etching procedures have been tested.[1]

The experiments were started with the procedure described in [4]. The goal was mainly to obtain stable tips for use in spectroscopy, where the tip apex radius plays a minor role. A saturated solution of $CaCl_2$ in H_2O and HCl was used for the

[1] The actual experiments, which are still in progress, have been carried out by Thomas Mildner. See his diploma thesis [3] for details.

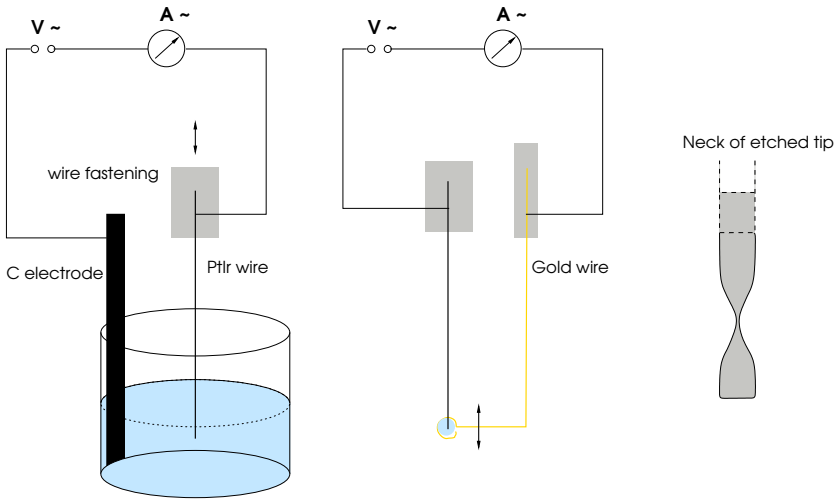

Figure B.8.: Schematic diagram of the two etching steps (left and middle). On the right an enlarged schematic view for an etched neck at the tip wire after the first etching step is shown.

etching. 40 mg of $CaCl_2$ was solved in 50 ml of distilled water. Since the reaction of the compounds is exothermic the $CaCl_2$ has to be added in parts. Afterwords the solution is filtered and the diluted HCl (4 ml HCl 37 % + 40 ml H_2O dist.) is added.

The etching contains two steps (Fig. B.8). First the rough etching is done with the PtIr wire as one electrode and a graphite electrode as counterpart. With a special tip etching apparatus the tip can be moved upwards and downwards into the solution while the beaker is placed on a movable table. We used a voltage of about 30 V and started at a current of 300 mA and waited until about 30 - 90 mA were reached before stopping the process. It seemed to be best to have only a small neck on the wire preventing the etched part of the wire to fall of (which happens also eventually, an example in Fig. B.9 a). The wire then is cleaned with water. During the second step the tip is sharpened by etching it within a small gold ring. The gold ring was dipped into a clean etching solution to obtain a small bubble in it. Then the tip is placed in the middle of this bladder and etched again with a lower voltage of 2 - 3 V. The gold ring can be moved upwards and downwards during etching. If there is still a small remaining piece with a neck, it has to be etched until the latter falls off. Since the bladder is blowing up during etching, this part is not so easy to control since the end part bends sometimes leading to curved tips. In case of no remainder the wire was just etched for a short time in order to sharpen and improve the apex of the tip. During this step the etching is observed through a small telescope to prevent too much etching and therefore flattening of the tip. After the etching process the tip is rinsed again in distilled water to remove any etching solvent. (The rinsing can be done in a small beaker with hot, but not cooking, water which is rotated by a stirrer flowing around the tip from its back part.)

There are some points which need further improvement. For example the etching

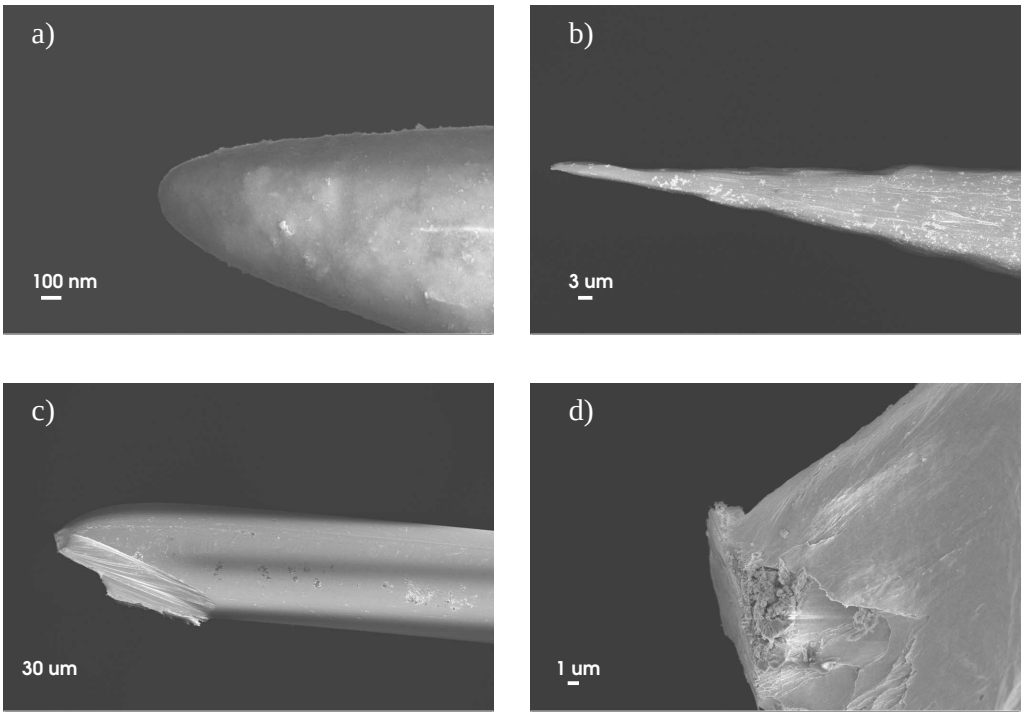

Figure B.9.: Upper part: Two examples for etched tips observed with an electron microscope. a) Tip where the neck already fell off during the first step, with a broad radius of about 350 nm. b) Sharper tip with corrugated surface where a neck was bended and the second step took more than 15 min. Lower part: In c) an example for a cut tip and its micro tip is shown in d). The scanning electron microscope pictures were done by T. Mildner.

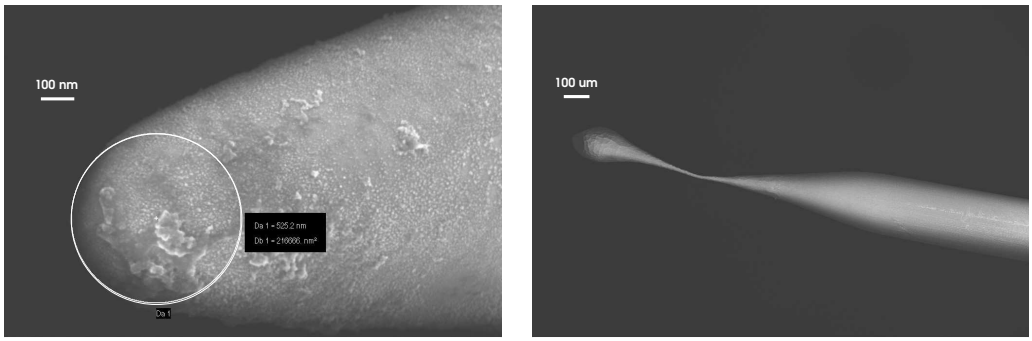

Figure B.10.: On the left a sharp tip with a radius of about 50 nm. On the right an example for an etched neck after the first step is shown. The images were taken by T. Mildner.

solution becomes black from carbon during the first step, while for STM the tips should be as clean as possible. It has been reported that acetone might be used instead of HCl which increases the surface tension [2]. A first attempt with an additional drop of acetone resulted in a limpid solution, but the bubbling was increased at the surface, which was roughened.

Also the usage of the gold ring needs to be changed a little bit to prevent a tip bending. This might be done by lowering of the ring from above the neck, such that the loose part is not covered completely by the bladder. Another way might be to put a small weight at the end of the wire, which can be done like for W tips [6]. Some examples of etched tips are shown in Fig. B.9. After the first step the tips had a somewhat rough surface with a honeycomb-like structure, which is generally removed in the second step. One cannot find a sharp cone as in the case of W tips, but any loose pieces, observed at cut tips, (see lower part of Fig. B.9) are eliminated. Tip radii of less than 50 nm can be achieved, as seen in Fig. B.10.

Bibliography

[1] R. Akiyama, H. Tanaka, T. Matsumoto, and T. Kawai. *Appl. Phys. Lett.*, 79:4387, 2001.

[2] L. Libioulle, Y. Houbion, and J.-M. Gilles. *J. Vac. Sci. Technol. B*, 3:1325, 1995.

[3] T. Mildner. Diplomarbeit, Universität Göttingen.

[4] I. H. Musselman and P. E. Russell. *J. Vac. Sci. Technol. A*, 4:3558, 1990.

[5] Group PD Dr. Ch. Jooss. University of Göttingen, Institut für Materialphysik, http://www.material.physik.uni-goettingen.de.

[6] C. Streng. *Wachstumsanalyse amorpher dicker Schichten und Schichsysteme.* Doktorarbeit, University of Göttingen, 2004.

[7] W. Westhäuser. Transporteigentschaften von Manganat-Filmen in magnetischen und elektrischen Feldern am Beispiel von $Pr_{0.68}Ca_{0.32}MnO_3$. Diplomarbeit, Universität Göttingen, 2004.

[8] W. Westhäuser, S. Schramm, and Ch. Jooss. *Europ. J. Phys. B*, 53:323, 2006.

C. Mathematical considerations

C.1. Autocorrelation function

The autocorrelation function, which can be used, e.g. for comparing structures within an image, constitutes a self-correlation and can be calculated via two dimensional Fourier transforms [2]. The correlation $C(x)$ of two complex functions is defined similar to a convolution as

$$C_{fg}(x) = f(x) * g(x) = \int_{-\infty}^{+\infty} f^*(u)g(u+x)du \tag{C.1}$$

and the autocorrelation is defined as

$$C(x) = C_{ff}(x) = f(x) * f(x) = \int_{-\infty}^{+\infty} f^*(u)f(u+x)du \tag{C.2}$$

which is also called an auto-covariance function. The two dimensional autocorrelation function is defined completely analogously. For a calculation the Wiener-Khinchine-Theorem is applied, that is the autocorrelation can be calculated via the inverse Fourier transform[1] $\mathbf{F}^-$

$$\mathbf{F}^- [f * f] = \hat{f}^* \hat{f} = \left|\hat{f}^2\right|. \tag{C.3}$$

Normally the measurements only exist as a limited amount of data points, so that the discrete form of the Fourier transform has to be used. To discretize the Fourier transform one either uses the sampling theorem or imagines it convolved with a box function (for the reduction of values into a pixel), then multiplied with a comb function (for the discretization) and again convolved with a box function (for the limited data range, which cannot be infinite). The reader is referred to [2] for more details on the formalism. As the result, both data spaces consist of limited and discretized values

$$\hat{f}_l = \frac{1}{N} \sum_{j=0}^{N-1} f_j \exp\left(-2\pi i \frac{jl}{N}\right) \tag{C.4}$$

and the respective inverse form. One thus gets a system of N linear equations with N summands, which could be written in matrix form. The matrix itself can in turn be decomposed into small matrices, which are easier to calculate, and this leads to the fast Fourier transform FFT, which is normally used by the programming languages like IDL [1].

[1] The operator $\mathbf{F}^\pm$ stands for the integration over the argument of the function and the sign corresponds to the sign in the exponential function. $\mathbf{F}^+ \left[\hat{f}(s)\right] = f(x) = \int_{-\infty}^{+\infty} \hat{f}(s) \exp(+2\pi i s x) dx$.

Bibliography

[1] IDL – Interactive data language. Research Systems, Inc. Version 6.0.

[2] W. H. Press, S. A. Teukolsky, W. T. Vetterling, and B. P. Flannery. *Numerical Recipes in C*. Cambridge University Press, 1992.

Acknowledgement

At the end of this thesis I would like to take the pleasant duty to express my gratitude to the people who accompanied me during the last years in the scientific and personal background of this work.

I would like to thank ...

... first of all Professor Konrad Samwer for his mentoring and lots of discussions which he managed to accomplish besides all his duties at university and the opportunity to write a thesis in a challenging field of solid state physics.

... Dr. Bernd Damaschke for his help in particular with the programming (there is a language without punctuation) and the great coffee from his very special coffee machine (being always at our service).

... PD Dr. Christian Jooss for being second referee and for participating in our manganite project with his group, which enriched the seminars and discussions.

... Juniorprofessor Stefan Mayr for providing his correlation analysis program (see you next night at the institute).

... Dr. Steffen Wirth at the MPI in Dresden for the first try at very low temperatures and discussions about STM measurements on manganites.

... Dr. Volker Neu and Dr. Ulrike Wolff at the IFW in Dresden for (also mental) support regarding technical matters concerning the Cryogenic SFM (yes, it has its own personality).

... the manganite group, especially PD Dr. Vasily Moshnyaga and Dr. Lakshama Sudheendra. There have been many fruitful discussions, numerous interesting seminars about manganites and many informative talks about other cultures.

... Thomas Mildner for exploring the tip etching world.

... all the people around. The years at the institute were very instructive and therefore I thank Juniorprofessor Stefan Mayr, Henrike Neubauer, Iris Kock, Tobias Edler, Uta Bete, Guido Mahnke and all the others for the get-together's and chats during the coffee breaks, walking-tours on external institute seminars and holding the fort in the sacred halls of the new physics department during uncommon working hours.

... the group around Dr. Martin Wenderoth for being very kind lab neighbors.

... our secretaries Alexandra Lüttich and Regina Hühne, who keep the institute

and projects going on the organizational side.

... Hartmut Eichenberg and Elmar Gatzemeier for the commitment of the workshop and Katrin Gehrke for the friendly help with the laboratory issues (nothing works without technical realization) and our systems administrator Carsten Mahn.

... the Deutsche Forschungsgemeinschaft for financial support.

... Dr. Christian Hettlage and Christian Tusche for a painstaking proof-reading and keeping me up at work.

... Christian Tusche for the many fruitful discussions about physics.

... the university Aikido group, which gave me a great opportunity to balance the office days (nothing goes beyond momentum and energy conservation) and to get to know very friendly people.

... Dr. Edith Kirsch-Auwärter and Dr. Sylke Ernst for delivering me some insight into the matters and politics outside scientific questions.

... Dr. Christian Hettlage for the many years of friendship in and outside the physics world (always take a towel, just in case).

... my friends Kai Nörthemann, Diana Marcano, Salvatore Manmana, Wolfgang Vukovich, Cathrin Hühne, Jeroen Custers, Kathrin, Sven and little Anna, Christian (B.), Roswitha, Georg, Axel and Heike for their company. Also many thanks to my parents as well as Ernst and Helga Harmening.

I am deeply grateful for the understanding and never-ending patience from Klaus.

Curriculum Vitae

Persönliche Daten

Name:	Sigrun Antje Köster
Geburtsdatum:	25. November 1975
Geburtsort:	Braunschweig

Universität

seit 2003	Promotion
2001–2002	Diplomarbeit, *"Änderung der Magnetowiderstandseffekte in $La_{0.7}Sr_{0.3}MnO_3$-Filmen durch Dotierung der Korngrenzen mit MgO"*, I. Physikalisches Institut, Universität Göttingen
1998–1999	Stipendium: University of California San Diego, USA
1998	Vordiplom
1996–2002	Physikstudium, Universität Göttingen und University of California
1995–1996	Chemiestudium, Universität Göttingen

Schule

1995	Abitur
1988–1995	Gymnasium Gaußschule, Braunschweig
1986–1988	Orientierungsstufe Rühme, Braunschweig
1982–1986	Grundschule Waggum, Braunschweig